UNIVERSITY OF CALIFORNIA
SANTA CRUZ

SEARCH FOR A HEAVY PHOTON IN THE 2015 ENGINEERING RUN DATA OF THE HEAVY PHOTON SEARCH EXPERIMENT

A dissertation submitted in partial satisfaction
of the requirements for the degree of

DOCTOR OF PHILOSOPHY

in

PHYSICS

by

Omar Moreno

June 2016

The Dissertation of Omar Moreno
is approved:

Professor Bruce Schumm, Chair

Professor Jason Nielsen

Professor Abraham Seiden

Tyrus Miller
Vice Provost and Dean of Graduate Studies

Table of Contents

List of Figures

List of Tables

Abstract

Search for a Heavy Photon in the 2015 Engineering Run Data of the Heavy Photon Search Experiment

by

Omar Moreno

The Heavy Photon Search (HPS) is a new experiment at Jefferson Lab that will search for heavy $U(1)$ vector bosons (heavy photons, dark photons or A') in the mass range of 10 MeV/c^2 to 1 GeV/c^2 that couple weakly to ordinary matter. Heavy photons in this mass range are theoretically favorable and may also mediate dark matter interactions. The heavy photon couples to electric charge through kinetic mixing with the photon, in turn, inducing an effective gauge coupling of the A' to electric charge, which is suppressed relative to the electron charge by a factor of $\epsilon \sim 10^{-2} - 10^{-12}$. Since heavy photons couple to electrons, they can be produced through a process analogous to bremsstrahlung radiation, subsequently decaying to narrow e^+e^- resonances which can be observed above the dominant QED trident background. For suitably small couplings, dark photons travel detectable distances before decaying, providing a second signature.

HPS will utilize this production mechanism to probe heavy photons with relative couplings of $\epsilon^2 \sim 10^{-5} - 10^{-10}$ and search for the e^+e^- decay of the heavy

photon via two signatures: invariant mass and displaced vertex. Using Jefferson Lab's high luminosity electron beam incident on a thin tungsten target along with a compact, large acceptance forward spectrometer consisting of a silicon vertex tracker and lead tungstate electromagnetic calorimeter, HPS will access unexplored regions in the mass-coupling phase space.

The HPS engineering run took place in spring of 2015 using a 1.056 GeV, 50 nA beam. This dissertation will present the results of a resonance search for a heavy photon in the mass range between 20 MeV/c^2 to 60 MeV/c^2 using a portion of the unblinded engineering run data which amounts to a luminosity of 74 nb^{-1} (.4671 mC of charge).

To my wife Monica and son Maddox.

Your love and inspiration make me feel like I can accomplish anything.

Acknowledgments

The completion of this dissertation was due in large part to the guidance and support that I received from my colleagues on the Heavy Photon Search experiment. Specifically, I want to thank John Jaros for taking the time to mentor me and instill in me valuable knowledge that I will continue to use in the future. I would also like to thank Tim Nelson, Per Hansson for their guidance through the construction of the Silicon Vertex Tracker and its data acquisition system as well as for helping me keep sane during our time at JLab. I want to thank Mathew Graham for being the greatest of all analysis leaders and guiding me through my analysis. Of course, I can't forget to thank Sho Uemura and Matthew Solt for their important contributions to this analysis and for the fun times we shared in the office.

My colleagues at the Santa Cruz Institute for Particle Physics were also crucial to me completing my dissertation. Specifically, I want to thank Bruce Schumm for giving me the opportunity to first work on ILC hardware, for helping me grow as an experimentalist and for mentoring me during my first few years of graduate school. I would like to thank Alex Grillo for taking the time to mentor me as well as Vitaliy Fadeyev who taught me the majority of the electronics knowledge I currently posses.

Without the support of my parents, sister and nephew, I wouldn't be the person I am today. To my father and mother, you always encouraged me to pursue my goals to the best of my ability and to work through whatever obstacles that life may have presented. The strong work ethic you instilled in me is one of the major reasons I was able to complete my dissertation. To my nephew Joseph, I have enjoyed seeing you grow intellectually these past few years and I'm looking forward to all the questions you will have once you read this dissertation. To my sister, thank you for all the support you gave me during my time in graduate school.

Finally, I want to thank my beautiful wife Monica Moreno. Your support and encouragement were crucial to the completion of this dissertation. It's not possible to put into words what you mean to me. I will love you until the end of time and I'm looking forward to the many memories we will continue to share.

Chapter 1

Introduction

The Standard Model (SM) of particle physics continues to be one of mankind's greatest intellectual achievements. It provides a mathematically elegant description of the building blocks of matter (quarks and leptons) and the forces through which they interact. With the discovery of the Higgs boson at the Large Hadron Collider in 2012 by both the ATLAS and CMS experiments [1, 2], all particles predicted by the SM have now been observed. However, there remain many outstanding issues which the SM fails to explain.

One such issue is the composition and nature of dark matter. The existence of dark matter was first inferred in the early 1930s by Zwicky when calculating the velocity dispersion of the galaxies in the Coma cluster [3]. Using the velocity dispersions, Zwicky calculated the cluster's mass using the virial theorem and found

it to be ∼400 times larger than what was expected from their luminosity. He then concluded that the Coma cluster contained far more of some yet unobserved *dunkel Materie* or 'dark matter' than luminous matter. Additional evidence would come a few decades later when Rubin and Ford observed that the rotational velocity of galaxies was approximately flat instead of decreasing as $1/\sqrt{r}$ as expected [4]. More recent results based on gravitational lensing [5] and the cosmic microwave background [6], further strengthen the argument for the existence of dark matter.

In 2008, the observation by the Payload for Antimatter Matter Exploration and Light-nuclei Astrophysics (PAMELA) of an unanticipated rise in the positron fraction [7] sparked a surge of interest in so called "hidden sector" models. Some of these models suggest that dark matter inhabits a hidden sector with its interactions mediated by a massive photon-like particle [8, 9, 10]. In fact, the possibility that nature contains an additional gauge boson (A', "dark," "hidden," "heavy" photon) was first considered by Holdom [11]. According to Holdom, an additional $U(1)$ gauge symmetry of nature would "kinetically mix" with the SM photon, in turn, inducing an effective gauge coupling of the heavy photon to electric charge, which is suppressed by a factor of $\epsilon \sim 10^{-2} - 10^{-12}$. Kinetic mixing between the A' and the SM photon establishes a portal through which the properties of not only dark matter but other hidden sector particles can be explored.

The effective coupling of the heavy photon to electric charge allows its production through a process analogous to bremsstrahlung radiation. The Heavy Photon Search (HPS) is a fixed target experiment that utilizes this production mechanism to search for heavy photons in the mass range of 10 MeV/c^2 to 1 GeV/c^2. It accomplishes this by using Jefferson Lab's high luminosity electron beam incident on a thin tungsten target to produce heavy photons which subsequently decay to e^+e^- pairs. The kinematics of the decay products are then reconstructed using a compact, large acceptance forward spectrometer consisting of a silicon vertex tracker and a lead tungstate electromagnetic calorimeter. With such a setup, HPS will be capable of not only searching for heavy photons which decay promptly at the target but also for those that are long lived, giving HPS access to unexplored regions in the mass-coupling phase space. The estimated reach of the HPS experiment at 2σ significance along with existing limits (see Section 2.3) are shown in Figure 1.1. The reach calculation assumes running using 1.1 GeV, 50 nA (solid gold line) and 2.2 GeV, 200 nA (blue line) beam for a week each. The full contour (dashed gold line) assumes an additional 2 weeks of running using a 4.4 GeV, 300 nA beam. Sensitivity to the upper region is achieved through a resonance search while the lower region utilizes a resonance search plus a displaced vertex.

The HPS engineering run took place in the spring of 2015 using a 1.056 GeV,

50 nA beam incident on a $0.125X_0$ tungsten target. This dissertation will present the results of a resonance search for a heavy photon in the mass range of 20 MeV/c^2 and 60 MeV/c^2 using the unblinded portion of the 2015 HPS engineering run data set. In total, the search uses 74 nb^{-1} (.4671 mC of charge) which amounts to less than 10% of the data collected during the engineering run. An analysis using the full engineering run dataset will be completed in the summer of 2016. Chapters 2-3 will motivate the need to search for heavy photons and provide an overview of its production mechanism. Chapters 4-5 detail the HPS detector and its performance. Finally, Chapter 6 will contain the details of the resonance search along with results and discussion.

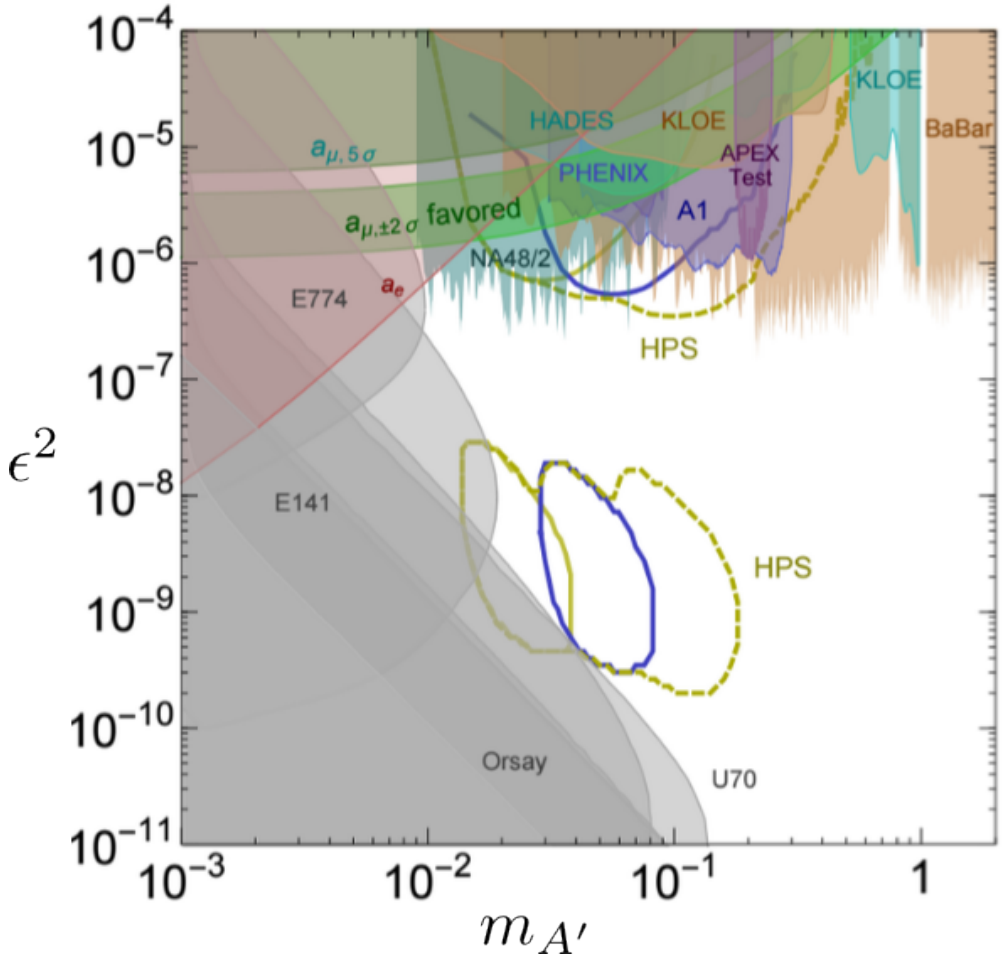

Figure 1.1: The estimated reach of the Heavy Photon Search experiment at 2σ significance along with existing constraints from beam dump [12, 13, 14, 15, 16, 17, 18, 19, 20], collider [21, 22, 23, 24] and fixed target experiments [25, 26, 27, 28]. The regions labeled "a_e" and "a_μ" are exclusions based on the anomalous magnetic moments of the muon and electron. The green band labeled "$a_\mu \pm 2\sigma$ favored" represents the region that an A' can be used to explain the discrepancy between the measured and calculated muon anomalous magnetic moment [29, 30]. A detailed discussion of these constraints can be found in Section 2.3. The reach calculation assumes HPS running using a 1.1 GeV, 50 nA (solid gold line) and 2.2 GeV, 200 nA (blue line) beam for a week each. The full contour (dashed gold line) assumes an additional 2 weeks of running using a 4.4 GeV, 300 nA beam. Sensitivity to the upper region is achieved through a resonance search while the lower region utilizes a resonance search plus a displaced vertex.

Chapter 2

Motivations

The existence of additional $U(1)$ gauge symmetries of nature are common in several Beyond the Standard Model (BSM) theories [31, 32, 33, 34, 35]. Such theories envision the associated gauge boson inhabiting a "hidden sector" consisting of a complex of particles and gauge bosons. Probing the structure of such a hidden sector may be possible through the so called "Vector" portal which describes the weak coupling of the A' to charged particles through "kinetic mixing" with the photon. In fact, it is natural for the A' to kinetically mix with the Standard Model (SM) photon through the interaction of massive fields carrying both SM hypercharge and dark charge [11]. The mixing of the photon with the A' would not only allow searching for new hidden sector particles, but also for dark matter which some theoretical models have envisioned as inhabiting the hidden sector,

with its interactions mediated via an A' [8, 9, 36, 37].

The chapter that follows will motivate the need to search for an A'. This includes an overview of current astrophysical anomalies that may be explained assuming a dark matter candidate that couples to a heavy photon. Finally, a review of current experimental limits on the A' coupling strength will be given.

2.1 Theoretical Formalism and Physics Motivation

As Holdom [11] formulated in the mid eighties, in a theory with $U(1)_Y \times U(1)'$ symmetry, there is a term in the gauge part of the Lagrangian that allows $U(1)_Y$ and $U(1)'$ to mix. The gauge part of such a theory can be written as

$$\mathcal{L}_{\text{gauge}} = -\frac{1}{4}F_Y^{\mu\nu}F_{Y,\mu\nu} - \frac{1}{4}F'^{\mu\nu}F'_{\mu\nu} + \frac{1}{2}\epsilon F'^{\mu\nu}F_{Y,\mu\nu} \tag{2.1}$$

where $F'_{\mu\nu} = \partial_\mu A'_\nu - \partial_\nu A'_\mu$ ($F_Y^{\mu\nu} = \partial^\mu A^\nu - \partial^\nu A^\mu$) is the field strength tensor of the heavy photon (SM hypercharge) and ϵ is a dimensionless coupling constant. Illuminating the low-energy effects that result from kinetic mixing can be achieved by decoupling the gauge fields through the redefinition of the SM hypercharge gauge field as

$$A_\mu \rightarrow A_\mu + \epsilon A'_\mu. \tag{2.2}$$

Ignoring all ϵ^2 terms that arise from such a transformation, this results in the diagonalization of Equation 2.1 as

$$\mathcal{L}_{\text{gauge}} = -\frac{1}{4}F_Y^{\mu\nu}F_{Y,\mu\nu} - \frac{1}{4}F'^{\mu\nu}F'_{\mu\nu}. \tag{2.3}$$

However, the redefinition of the field also affects the interaction term of the Lagrangian, $\mathcal{L}_{int} = A^\mu J_\mu^{EM}$ as

$$A^\mu J_\mu^{EM} \to (A^\mu + \epsilon A'^\mu) J_\mu^{EM}. \tag{2.4}$$

As a result, an effective coupling is induced between the electromagnetic current and the heavy photon field that is suppressed by a factor of ϵ.

Mixing between the SM photon and the heavy photon can naturally be generated at loop-level, assuming there exist heavy multiplets, (Φ, Φ'), that are charged under both the SM hypercharge and dark charge (see Figure 2.1). Integrating out the fields generates values of ϵ on the order of

$$\epsilon \sim \frac{g_Y g_D}{16\pi^2} \ln\left(\frac{m_\Phi}{m_{\Phi'}}\right) \sim 10^{-3} - 10^{-1} \tag{2.5}$$

where g_Y (g_D) are the SM hypercharge (dark) coupling and $(m_\Phi, m_{\Phi'})$ are the

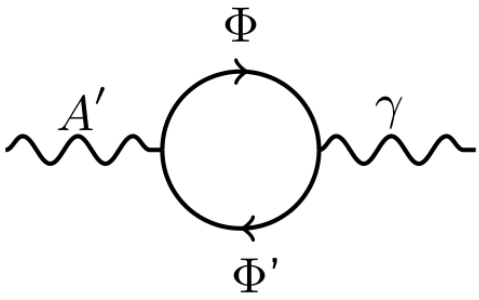

Figure 2.1: Kinetic mixing of a Standard Model photon with a heavy photon at one-loop through the interaction of massive fields charged under the Standard Model hypercharge and dark charge.

masses of the two fields [37, 17]. If the theory doesn't contain split multiplets charged under both $U(1)_Y$ and $U(1)'$, the mass splittings can be generated by additional loops, leading to values of $\epsilon \sim 10^{-6} - 10^{-3}$. In some string theory constructions, values as small as $\epsilon \sim 10^{-12}$ are expected [31, 38, 39].

The possibility that a new gauge boson can couple to charged SM particles is very appealing. It may offer one of the few portals to probe a new sector composed of light weakly coupled particles and possibly dark matter (see Section 2.2). Such a coupling can be exploited by current and future experimental programs in order to measure the properties of the hidden sector and possibly provide insight into many outstanding physics puzzles.

2.2 Motivations for a Heavy Photon from Dark Matter

Although the existence of dark matter (dark matter) has been firmly established through its gravitational interaction [3, 4, 5, 6], its exact nature continues to elude us. An appealing possibility is that dark matter inhabits a "hidden sector" with its interactions mediated by an A'. In turn, the kinetic mixing of the A' with the SM photon may provide a portal that would allow the exploration of not only the properties of dark matter but the hidden sector itself. Furthermore, several recently observed astrophysical anomalies [7, 40, 41, 42, 43, 44, 45, 46] may have a dark matter interpretation if dark matter is charged under $U(1)'$. A summary of those anomalies along with their dark matter interpretation will be presented here.

2.2.1 Cosmic Rays

Interest in hidden sector models surged in 2008 with the announcement by PAMELA of an unforeseen rise in the ratio of the cosmic ray (CR) positron flux to CR electron flux, $e^+/(e^+ + e^-)$, above 10 GeV [7]. The rise was later confirmed by both the Fermi Gamma-Ray Space Telescope [40] and Alpha Magnetic Spectrometer-02 (AMS-02) [41] experiments and observed to continue up to 200 GeV.

The main source of CR positrons was expected to come from the interaction of CR nuclei with the interstellar medium (secondary production). If such a production mechanism was dominant, cosmic ray propagation models predicted the fraction would fall with increasing energy. The observed rise immediately led to the speculation of additional sources of positrons [47, 48].

One attractive scenario that could account for the rise is the annihilation of dark matter to leptons ($e^+e^-, \mu^+\mu^-$). In fact, such models where found to fit the data fairly well but require much larger annihilation rates compared to those expected assuming the typical thermal cross-section [49]

$$\langle \sigma v \rangle \simeq 3 \times 10^{-26} \mathrm{cm}^3 \mathrm{s}^{-1}. \tag{2.6}$$

Alternatively, if dark matter interactions are mediated by a heavy photon, a "Sommerfeld enhancement" of the annihilation cross-section proportional to $\langle \sigma v \rangle \sim 1/v$ can occur [8]. In such scenarios, the "freeze-out" cross-section that leads to the currently observed relic abundance remains unaffected since the velocity of dark matter in the early universe was high and the Sommerfeld enhancement had not effectively turned on. If the heavy photons created in the annihilation of dark matter subsequently decay to leptons (Figure 2.2), the resulting e^+e^- spectrum could account for the rise. Using the latest AMS-02 results, such a model

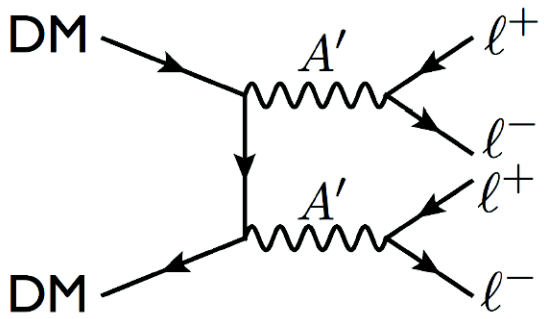

Figure 2.2: Diagram of dark matter annihilation to a heavy photon which subsequently decays into a pair of leptons.

can accommodate the data only if the mass and annihilation cross-section of dark matter ranges between $\sim$ 1.5 - 3 TeV and $\langle \sigma v \rangle \sim (6 - 23) \times 10^{-24}$ cm^{-3}/s [50].

The most recent measurement of the cosmic microwave background (CMB) by the Planck satellite strongly disfavor dark matter annihilation as the cause of the CR excess [51]. The annihilation of dark matter in the early universe injects extra energy into the primordial plasma. This would increase the fraction of hydrogen that was ionized during recombination, resulting in a modification of the CMB spectrum. Thus, a constraint on the annihilation cross-section of dark matter can be obtained through the measurement of the CMB anisotropy.

2.2.2 Light Dark Matter

Recently, an analysis of three years of data collected by the Fermi Large Area Telescope observed an extended emission in the spectrum of gamma-rays originat-

ing from the Galactic Center [42, 43, 44, 45]. Several models have been devised to try to explain the emission including the collision of energetic protons accelerated by a super-massive black hole [52], pulsars [53] and dark matter annihilation to leptons or hadrons [52, 54]. The emission can also be explained in the context of dark matter annihilating to an A' which subsequently decays to SM particles [10]. Such a model assumes a dark matter candidate of mass ~ 10 GeV annihilating to a heavy photon with a mass ~ 100 MeV.

Another anomaly that can be explained in the context of a light dark matter candidate that couples to a heavy photon is the observation of a 3.5 keV X-ray line in the spectrum of 73 galaxy clusters [46]. Specifically, the "eXciting Dark Matter" model [55] proposes the existence of a doublet of dark matter states whose self interactions are mediated by a heavy photon. As shown of Figure 2.3, a pair of dark matter particles upscatter via an A' to produce a pair of excited states, $\chi^*\chi^*$. This is immediately followed by the decay $\chi^* \to \chi\gamma$, producing an X-ray line.

2.3 Current Limits on Heavy Photons

As previously discussed, a heavy photon with a mass between 1 MeV and 1 GeV and ϵ as small as 10^{-12} is well motivated by both theoretical considerations

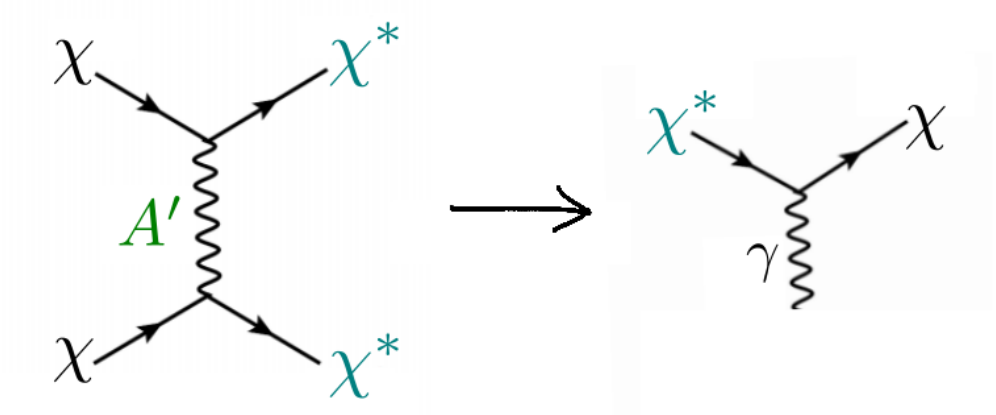

Figure 2.3: A diagram depicting the self-scattering of dark matter via a heavy photon into an excited state. The excited state subsequently decays producing an observable X-ray line.

and recent astrophysical anomalies. A major portion of this region in the mass-coupling phase-space remains hitherto unexplored. However, several experiments will be taking place in the coming years with the intention to probe this favorable portion of phase space. These include HPS, APEX [56], DarkLight [57], VEPP-3 [58], MESA [59], Mu3e [60], SeaQuest [61], SHiP [62], Belle-II and LHCb [63, 64].

Existing 2σ significance constraints from beam dump [12, 13, 14, 15, 16, 17, 18, 19, 20], collider [21, 22, 23, 24] and fixed target experiments [25, 26, 27, 28] on heavy photons with a mass and coupling in the favorable region are shown in Figure 1.1. The regions labeled "a_e" and "a_μ" are exclusions based on the muon and electron $g-2$. The green band labeled "$a_\mu \pm 2\sigma$ favored" represents the region that an A' can be used to explain the discrepancy between the measured

and calculated muon anomalous magnetic moment [29, 30]. The experimental searches for heavy photons will be discussed in more detail in the sections that follow.

2.3.1 Electron Beam Dump Experiments

Electron beam dump experiments make use of a high intensity beam "dumped" onto a thick (∼cm) target to produce highly boosted heavy photons through a process analogous to photon bremsstrahlung. In order to suppress the large SM backgrounds produced at the target, a shield of thickness between 1 and 100 cm is placed immediately downstream of the target, and in front of the detector. Since the heavy photons interact weakly with SM particles, sufficiently long lived heavy photons will traverse the shield before reaching an open space upstream of a detector. The decay products of heavy photons decaying in this region will travel unimpeded until detected. The thickness of the target and shield in combination with a high luminosity beam allow such experiments to be sensitive to heavy photons with small couplings which tend to travel considerable distances before decaying. Such experiments tend to be sensitive to heavy photons which have a mass on the order of 100 MeV and a coupling in the range $10^{-7} \leq \epsilon \leq 10^{-3}$. Sensitivity to larger couplings is limited by the lifetime of the A' since short lived

heavy photons will decay in the shield.

Several electron beam dump experiments were devised over the last several decades with the intention of searching for axions [65] [1]. These included E137 [12] and E141 [13] conducted at SLAC National Accelerator Laboratory, E774 [14] at Fermi National Accelerator Laboratory, and experiments at KEK [15] in Japan and Orsay [16] in France. The results from each of these experiments have been reinterpreted in the context of a search for a heavy photon and used to set limits on the coupling strength ϵ [17, 18].

2.3.2 Proton Beam Dump Experiments

Proton beam dump experiments can also be used to search for heavy photons through either the decay of neutral mesons produced at the target or proton bremsstrahlung. One such experiment, performed at the U70 accelerator at IHEP Serpukhov, used a 68.6 GeV proton beam incident on an iron target to search for axions and a light Higgs boson [19, 20]. The data collected by the experiment were reanalyzed, and used to search for a heavy photon. Specifically, The myriad of π_0 mesons produced at the target were used to search for an A' using the $\pi_0 \to A'\gamma(A' \to e^+e^-)$ decay channel [66]. Furthermore, the production of heavy

[1] Axions are particles postulated by Peccei and Quinn in the late 70's in an attempt to resolve the strong CP problem.

photons through proton bremsstrahlung was also used to search for an $A' \to e^+e^-$ [67].

2.3.3 Colliders

The past few decades saw the operation of several high-luminosity e^+e^- colliders that were able to collect data at different center-of-mass energies. These include KLOE, running at the the DAΦNE ϕ factory, and BaBar at the PEP-II B-Factory. Searches at BaBar were performed using the channel $e^+e^- \to A'\gamma(A' \to \mu^+\mu^-)$ [21, 22]. KLOE searched for heavy photons in the decays of the ϕ meson. Specifically, the channel $\phi \to \eta A'(A' \to e^+e^-)$ was used to set limits on the coupling strength of the A' [23, 24].

The PHENIX experiment at the Relativistic Heavy Ion Collider also searched for heavy photons using neutral meson produced in $p+p$ and d+Au collisions [68]. Specifically, the decay channels $\pi_0 \to \gamma A'(A' \to e^+e^-)$ and $\eta \to \gamma A'(A' \to e^+e^-)$ were used to set limits on the coupling strength of the A'.

2.3.4 Fixed Target Experiments

The A' production mechanism used by electron fixed target experiments is the same as that used by electron beam dump experiments. However, unlike beam dump experiments, the targets used by fixed target experiments are thin allowing

such experiments to be sensitive to promptly decaying heavy photons, i.e. A' with coupling on the order of $\epsilon \sim 10^{-3} - 10^{-1}$. Experiments such as HPS also have the ability to search for heavy photons which decay within a few cm of the target. Thus far, fixed target searches for a heavy photon using an electron beam have been completed by APEX [25] and A1 at the MAINZ microtron [26].

Experiments such as HADES [27] and NA48/2 [28] can also search for heavy photons using neutral mesons. Specifically, HADES used a 3.5 GeV proton beam incident on both a hydrogen and niobium target to produce heavy photons through the channels $\pi_0 \to \gamma A'$, $\eta \to \gamma A'$ and $\Delta \to N A'$ with the A' assumed to decay to an e^+e^- pair. NA48/2 used protons extracted from CERN SPS incident on a berrylium target to produce a Kaon beam. The channel $K^{\pm} \to \pi^{\pm}\pi^0(\pi^0 \to \gamma A')$ was used to search for heavy photons.

Chapter 3

HPS Signal and Backgrounds

The effective coupling between the A' and electric charge can be exploited to produce heavy photons through a process analogous to bremsstrahlung radiation. The heavy photon subsequently decays to narrow e^+e^- resonances, which can be observed above the dominant quantum electrodynamic (QED) trident background. For suitably small couplings, heavy photons travel detectable distances before decaying providing an additional search channel. In the chapter that follows, both the heavy photon production mechanism and backgrounds will be discussed.

3.1 Production of Heavy Photons

Sensitivity to the theoretically favored regions of the heavy photon mass-coupling phase space can be best achieved using high luminosity fixed target experiments [17]. In such experiments, an electron of energy E_0 incident on a high Z target will radiate heavy photons through a process analogous to ordinary photon bremsstrahlung. However, as discussed below, the weak coupling of the A' to electrons along with its relatively large mass will lead to rates and kinematics which are very different from ordinary photon bremsstrahlung.

Consider the process shown in Fig. 3.1 where an A' with momentum $k = (E_{A'}, \vec{k})$ is radiated by an electron of momentum $p = (E_0, \vec{p})$ incident on a target of mass M_i and momentum $P_i = (M_i, 0)$. The energy-angle distribution of heavy photons produced in such a reaction can be estimated using the Weizacker-Williams approximation (WWA) [17, 69, 70, 71]. The WWA models the process as the scattering of photons sourced by the target nuclei by the incident electron in the rest frame of the electron. Therefore, the energy-angle distribution can be

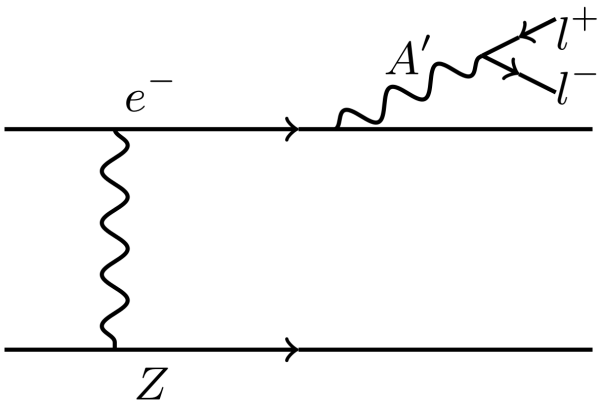

Figure 3.1: A heavy photon can be produced through a process analogous to ordinary photon bremsstrahlung.

obtained from the Compton-like process as

$$\left[\frac{d\sigma(e(p)+Z(P_i)\to e(p')+A'(k)+Z(P_f))}{dx\,d\cos\theta_{A'}}\right]_{\text{W.W.}} =$$
$$\left(\frac{\alpha\chi}{\pi}\right)\left(\frac{E_0 x\sqrt{1-m_{A'}^2/E_0^2}}{(1-x)}\right)\frac{d\sigma(e(p)\gamma(q)\to e(p')A'(k))}{d(p\cdot k)}|_{t=t_{\min}} =$$
$$\frac{8\alpha^3\epsilon^2E_0^2x\sqrt{1-m_{A'}^2/E_0^2}}{U^2}\chi\left[\left(1-x+\frac{x^2}{2}\right)-\frac{(1-x)^2m_{A'}^2}{U^2}\left(m_{A'}^2-\frac{Ux}{1-x}\right)\right] \tag{3.1}$$

where P_f and $p' = (E', \vec{p'})$ are the final momentum of the electron and target respectively, $t = -q^2 = -(P_i - P_f)^2$ is the momentum transfer, $\alpha \sim 1/137$ is the fine structure constant, θ_A is the opening angle of the A' relative to the incident electron in the lab frame, $x = E_{A'}/E_0$ is the fraction of the incident electron

energy carried by the A', m'_A is the mass of the heavy photon. The function

$$U(x, \theta_{A'}) = E_0^2 x \theta_{A'}^2 + m_{A'}^2 \frac{1-x}{x} + m_e^2 x \tag{3.2}$$

is related to the virtuality of the intermediate electron. The WW effective photon flux, χ, is related to the electric form factor as

$$\chi = \int_{t_{\min}}^{t_{\max}} \left(G_{2,\mathrm{el}}(t) + G_{2,\mathrm{in}}(t)\right) \frac{t - t_{\min}}{t^2} dt \tag{3.3}$$

where $G_{2,\mathrm{el}}$ is the elastic form factor, $G_{2,\mathrm{in}}$ is the inelastic form factor, $t_{min} = (m_{A'}^2/2E_0)^2$ and $t_{max} = m_{A'}^2$. Both the elastic and inelastic form factors parameterize effects due to electron screening and the size of the nucleus. Their exact forms are given in the appendix of [17]. For the conditions during the engineering run, a reduced WW effective photon flux in the range $\chi^2/Z^2 \sim 5 - 10$ is expected.

Assuming $m_e << m_{A'}$, and integrating Equation 3.1 over all angles yields

$$\frac{d\sigma}{dx} = \frac{8\alpha^3 \epsilon^2 \sqrt{1 - m_{A'}^2/E_0^2}}{m_{A'}^2 \frac{1-x}{x} + m_e^2 x} \chi \left(1 - x + \frac{x^2}{3}\right). \tag{3.4}$$

Although Equation 3.4 reduces to the cross-section of photon bremsstrahlung in the limit that $m_{A'} \to 0$, their production rate and kinematics differ in several

ways:

- As can been seen from Equation 3.4, the rate of production of heavy photons is $\propto \frac{\alpha^3\epsilon^2}{m_{A'}^2}$. This implies that it is suppressed by a factor of $\frac{\epsilon^2 m_e^2}{m_{A'}^2}$ relative to ordinary photon bremsstrahlung.

- The WW effective photon flux has a sharp turn off as the mass of the A' increases or the energy of the incident beam decreases further suppressing the production cross-section in these cases. For the HPS engineering run, the turn off occurs at around 400 MeV.

- The A' production rate is maximized when $x \approx 1$ since $U(x, 0)$ is minimized. As a result, when an A' is produced, it will carry most of the beam energy.

- The emission angle of the heavy photon has a cutoff given by

$$\theta_{A',\max} \sim \max\left(\frac{\sqrt{m_{A'}m_e}}{E_0}, \frac{m_{A'}^{3/2}}{E_0^{3/2}}\right) \tag{3.5}$$

  which is much smaller than the opening angle of the decay products of the A', $\sim m_{A'}/E_0$.

Equation 3.4 can be used to derive an expression for the number of heavy photons produced when N_{e^-} electrons scatter in a thin-target of radiation length,

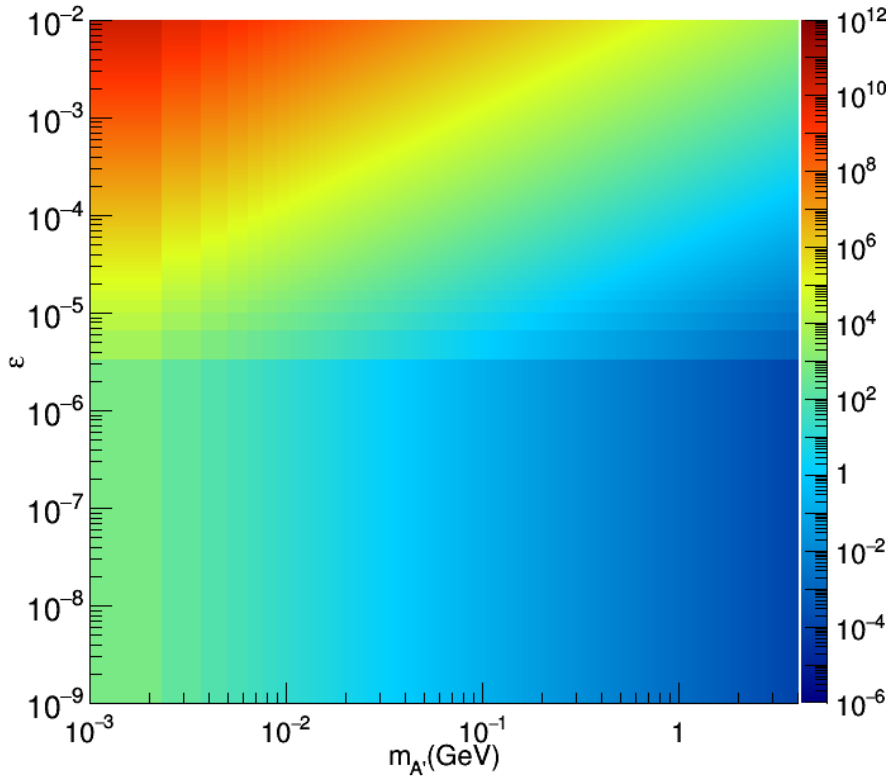

Figure 3.2: The expected number of A' events assuming .4671 mC of charge on target.

$T \ll 1$ as

$$N_{A'} \sim N_{e^-} \frac{N_0 X_0}{A} T \frac{Z^2 \alpha^3 \epsilon^2}{m_{A'}^2} \frac{\chi}{Z^2} \tag{3.6}$$

where N_0 is Avogadro's number, X_0 is the radiation length of the target and A is the atomic mass [17]. Figure 3.2 shows an estimate of the expected number of A' events as a function of A' mass and ϵ assuming .4671 mC of charge on target.

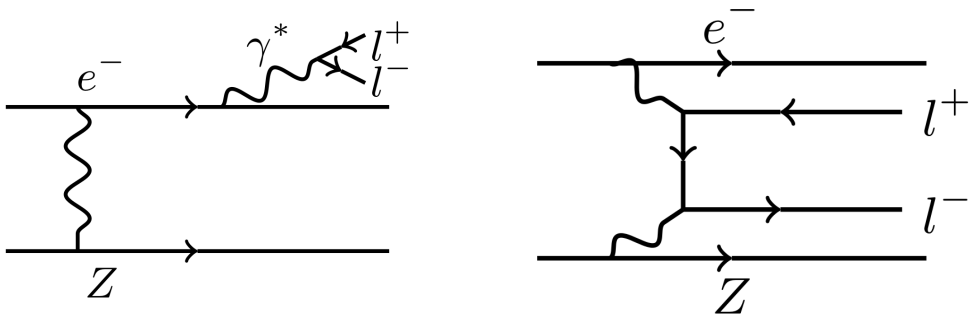

Figure 3.3: Diagrams of the radiative and Bethe-Heitler trident reactions.

3.2 Trident Backgrounds

The primary background expected to dominate the final event sample of the HPS experiment is the QED Bethe-Heitler and radiative trident processes. Diagrams of these processes are shown in Fig. 3.3. The heavy photon signal is expected to appear as a resonance above the trident invariant mass distribution so an understanding of these backgrounds is highly desirable.

The kinematics of the irreducible radiative trident background are indistinguishable from A' signal events within an invariant mass window, δm, centered at $m_{A'}$. Specifically, the A' production cross-section is related to the production cross-section of radiatives as

$$\frac{d\sigma(e^-Z \to e - Z(A' \to l^+l^-))}{d\sigma(e^-Z \to e - Z(\gamma^* \to l^+l^-))} = \frac{3\pi\epsilon^2}{2N_{eff}\alpha}\frac{m_{A'}}{\delta m} \tag{3.7}$$

where N_{eff} is the number of decay channels available. Therefore, radiatives can be used to analyze both the rate of the A' signal production and the sensitivity of an experiment to A' signals.

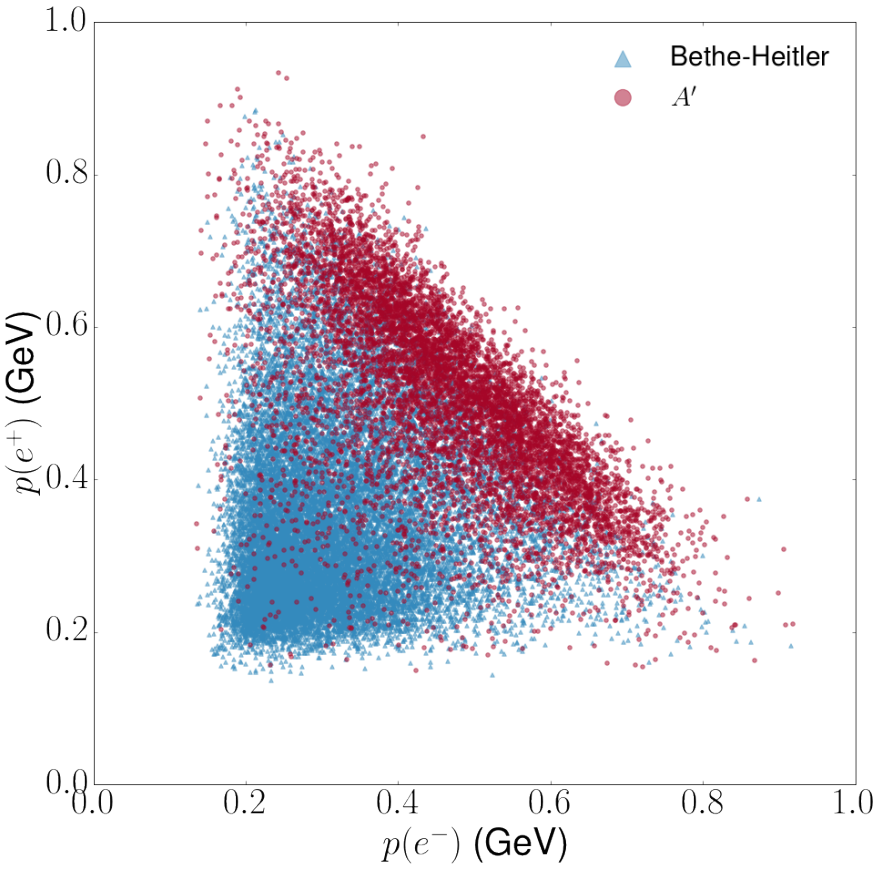

Figure 3.4: Scatter plot of the positron momentum versus the electron momentum of pairs from Bethe-Heitler background (blue) and 50 MeV A' signal events (red). The kinematics of the irreducible radiative background are indistinguishable from A' signal events within an invariant mass window, δm, centered at $m_{A'}$ and can be used to analyze the rate of A' signal production.

Although the rate of the Bethe-Heitler process dominates among the two pro-

cesses, its different kinematics can be used to reduce its contributions in the final event sample. Specifically, the A' decay products are highly boosted while the recoiling electron is soft and scatters at large angles. In contrast, at higher pair energies, the Bethe-Heitler process is not enhanced. Furthermore, only one of the leptons in the pair will be highly boosted, while the other will be much softer. These kinematic differences are illustrated in Figure 3.4 which shows the energy of the positron versus the electron energy for both A' (red) and Bethe-Heitler (black) events. As can be seen from the figure, the signal distribution is concentrated in the region where the sum of the energy of the electron and positron is approximately equal to the beam energy.

Chapter 4

The HPS Apparatus

At the energies at which the HPS experiment is operating, the electroproduced A' will carry most of the incident beam energy. Consequently, the A' decay products will be highly boosted, necessitating a detector with very forward acceptance that can be placed in close proximity to the target. Maximizing the acceptance requires placing the detector close to the beam plane, encroaching on a "dead zone" which is occupied by an intense flux of multiple Coulomb scattered beam particles along with radiative secondaries originating from the target. In order to avoid additional background from beam gas interactions, the detector needs to operate in vacuum. Finally, minimizing the material budget of the active area of the detector is essential to reducing the multiple scattering that dominates both the mass and vertex resolutions that determine the experimental sensitivity.

These design principles led to the conception of the HPS detector. Specifically, HPS utilizes a compact, large acceptance forward spectrometer consisting of a silicon vertex tracker (SVT) along with a lead tungstate electromagnetic calorimeter (Ecal). The SVT is installed inside a vacuum chamber immediately downstream of a thin ($0.125\%X_0$) tungsten target. The vacuum chamber resides within an analyzing magnet providing a .24 Tesla field perpendicular to the beam plane, allowing for the precise measurement of track momenta. The Ecal, placed downstream of the tracker, provides the primary trigger for the experiment and is also used for electron identification. Together, both subsystems provide the complete kinematic information required to reconstruct heavy photons. An overview of the HPS Detector is shown in Figure 4.1.

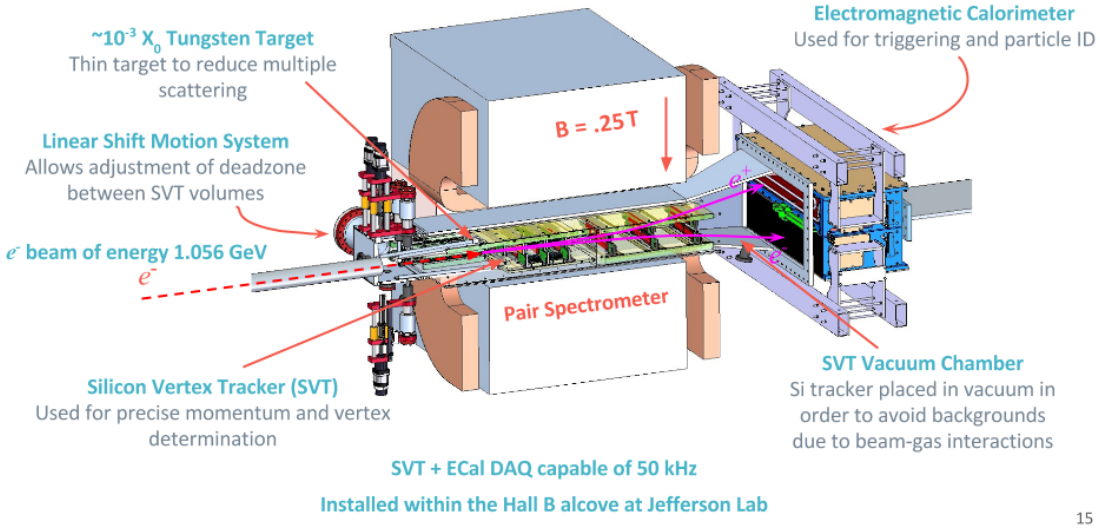

Figure 4.1: Schematic view of the Heavy Photon Search Detector used during the 2015 engineering run.

The HPS detector was installed and commissioned within the Hall B alcove at the Thomas Jefferson National Accelerator Facility (JLab) in Newport News, VA early in the spring of 2015. Shortly after, an engineering run took place utilizing the Continuous Electron Beam Accelerator Facility (CEBAF) operating at an energy of 1.056 GeV and current of 50 nA.

The chapter that follows will detail various elements of the experiment. It will begin with a discussion of CEBAF and continue with descriptions of several beamline elements, SVT, Ecal and data acquisition system (DAQ).

4.1 CEBAF

CEBAF's ability to provide a nearly continuous, clean and intense electron beam makes it ideal to search for heavy photons with weak couplings. Recently, CEBAF underwent an upgrade that increased its maximum operating energy to 12 GeV and introduced a new experimental hall, Hall D, that will house the GlueX detector [72]. The upgraded facility is now capable of delivering 11 GeV electron beams to the three existing experimental halls (Hall A, B, C) and can use the 12 GeV electron beam to generate and deliver a 9 GeV photon beam to Hall D. The maximum current that it can deliver to halls A and C is 85 μA while Halls B and D can receive no more than 5 μA.

As shown in Figure 4.2, achieving 12 GeV operation required several improvements to the accelerator [73]. Central to the upgrade was the addition of 5 cryomodules to each of the linacs. Coupled with upgrades to the accelerator magnets and power supplies, the additional cryomodules allowed each linac to accelerate electrons at a rate of 2.2 GeV per pass up to a maximum of 5 passes. Enabling

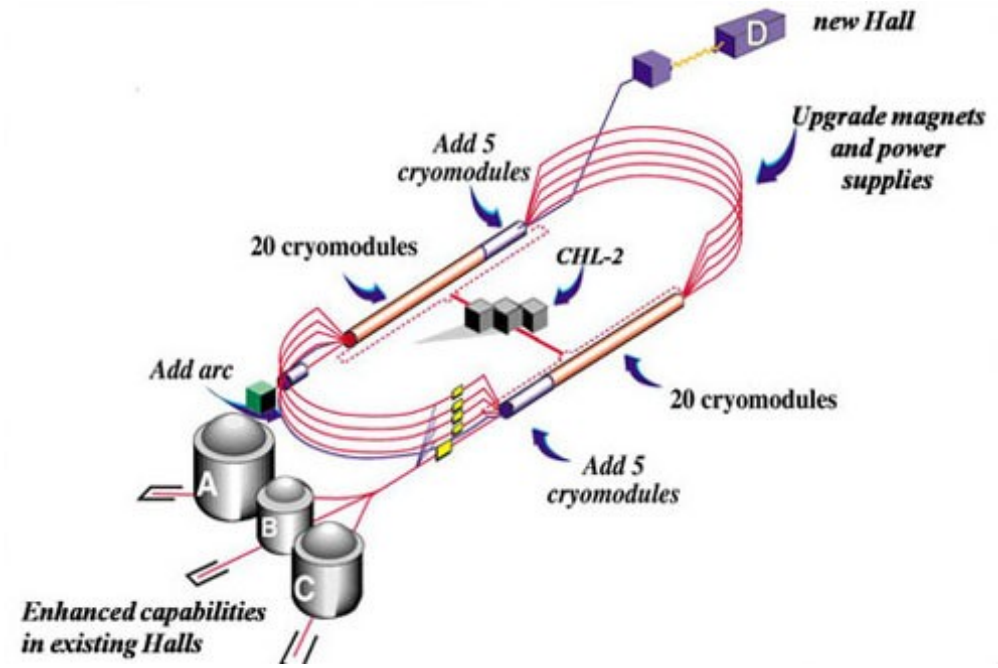

Figure 4.2: A diagram of the Thomas Jefferson National Accelerator Facility Continuous Electron Beam Accelerator Facility showing the components that were upgraded as part of the 12 GeV Upgrade program.

four-hall operation also required the addition of a new 750 MHz RF separator, a new laser to the electron source and a 10th arc which provides the additional pass of acceleration that allows delivery of the maximum beam energy to Hall D.

4.1.1 Electron Production and Injection

The electrons injected into the accelerator were produced by photoemission from a strained GaAs superlattice photocathode [74]. Each of the four experimental halls has a dedicated gain-switched fiber coupled laser of wavelength 1560 nm. The lasers are frequency doubled in order to produce light of wavelength of 780 nm, matching the band gap of the superlattice cathode. The lasers are phased shifted and are each pulsed for $\approx$ 40 ps at the frequency of 499 MHz. Since the operational frequency of the accelerator cryomodules is 1497 MHz, four hall operation requires subharmonics of 499 MHz to be chosen. This is achieved by "cutting away" pulses using an optical modulator [75].

The photoemission electrons are released into an extremely high vacuum environment at a pressure of 10^{-11} to 10^{-12} Torr. The free electrons are then delivered into the injector by a 100 keV electron gun. The injector itself then accelerates the electron bunches to an energy of 50 MeV before they are delivered into the accelerator.

4.1.2 Electron Acceleration

The CEBAF accelerator is composed of two linacs arranged in a racetrack configuration as shown in Figure4.2. Each of the linacs consist of 25 cryomodules,

5 of which were added as part of the upgrade. The original (new) cryomodules consist of 8 5-cell (7-cell) superconducting radio frequency (RF) cavities made of ultra-pure Niobium (see Figure 4.3). The original cryomodules are capable of

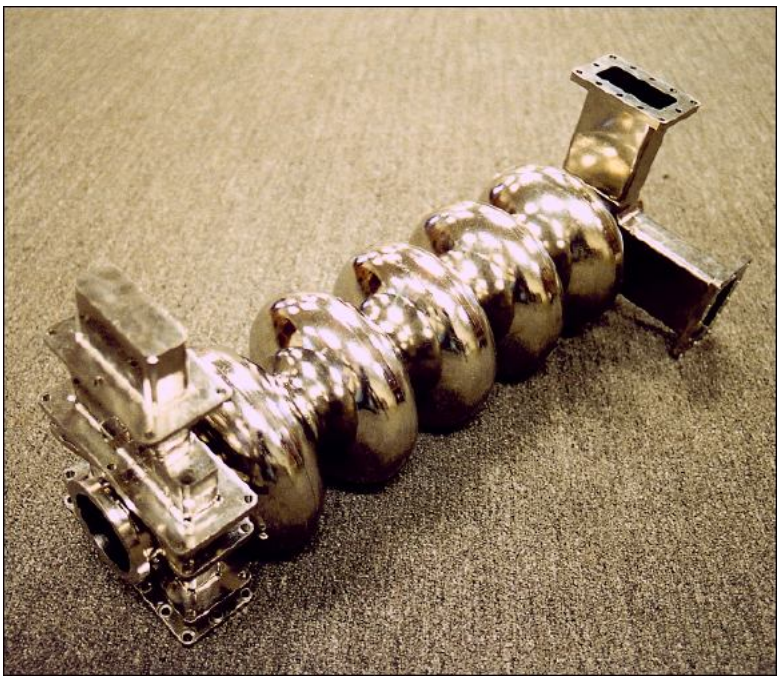

Figure 4.3: A 5-cell ultra-pure Niobium superconducting radio frequency cavity used to accelerate electrons at CEBAF.

accelerating an electron upwards of 25 MeV while the newly installed cryomodules can achieve an acceleration of 100 MeV. This leads to an acceleration of 1.1 GeV per linac and 2.2 GeV per pass. The number of passes depends on the energy requirements of the experiment taking place. However, for electrons delivered to Halls A, B and C, the maximum number of passes is 5, while for Hall D, it's 5.5.

Electron bunches circulating the accelerator can be delivered to a Halls A, B

and C by an RF separator operating at a frequency of 499 MHz. Delivery to Hall D uses an RF separator of 750 MHz.

4.1.3 Single Pass Operation For HPS

During the Spring of 2015, HPS was prepared to run at a beam energy of 2.2 GeV, in conjuction with the commissioning of the 750 MHz RF separator. Unfortunately, an incident occurred which resulted in the loss of the new CHL required to operate the accelerator as a 12 GeV machine. The loss caused the accelerator to fallback to 6 GeV operation using a single CHL. As a result, HPS was given the unique opportunity to run with a beam energy of 1.056 GeV allowing the experiment to have sensitivity to the g-2 favored region of the mass-coupling phase space.

4.2 Beamline

4.2.1 Layout

The HPS experiment is installed within the Hall B alcove upstream of the CEBAF Large Acceptance Spectrometer 12 detector. The experiment utilizes a three-magnet chicane system as shown in Figure 4.4. The distance between the center of the magnets is 218.1 cm. The second dipole of the setup, the Hall B

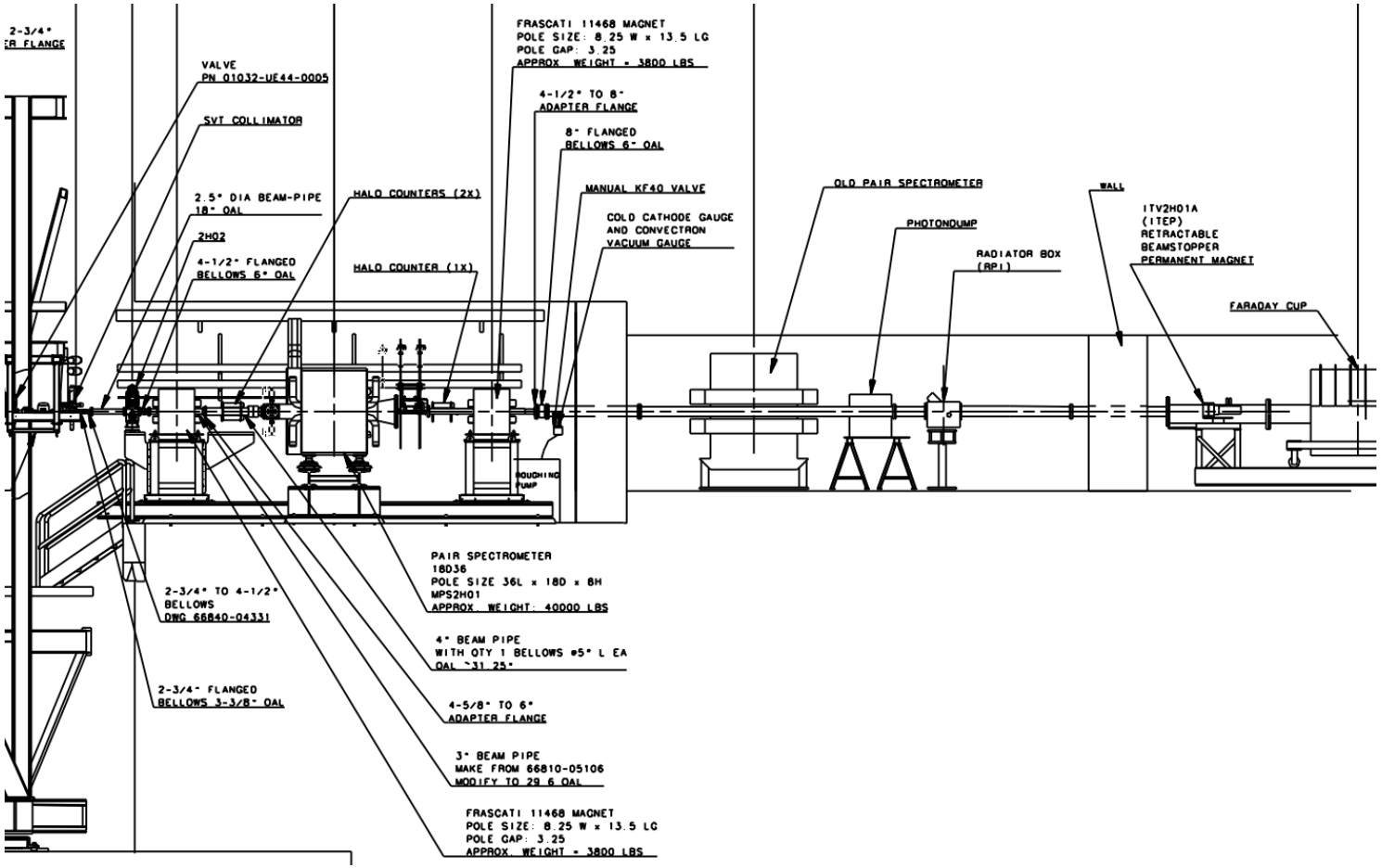

Figure 4.4: Configuration of the beam line during the HPS engineering run.

Pair Spectrometer (PS), serves as the analyzing magnet of the experiment. It is a 18D36 magnet with a pole length of 91.44 cm and gap size of 45.72×15.24 cm^2. It provides a 0.24 Tesla field perpendicular to the beam plane. A vacuum chamber, housing the SVT, resides within the gap of the analyzing magnet. The first and last dipoles of the chicane are "Frascati" H-dipole magnets. They are used to steer the deflected beam back onto the beam line and into the beam dump downstream. They have a pole length of 50 cm and were operated at 0.6 Tesla.

A 0.125%X_0 ($\sim 4\mu$m thick) tungsten target is installed at the upstream edge of the PS magnet, 10 cm from the first layer of the SVT. The target is connected a rigid support rod that is attached on the upstream side to a linear shift. This allows the precise movement of the target in an out the of the beam plane using a stepper motor. Far upstream of the target, a 10 mm thick tungsten protection collimator with a 4×10 mm^2 hole was installed. The protection collimator was used to protect the SVT silicon planes from being hit directly by mistered beam.

A vacuum box is mounted on the upstream end of the PS vacuum chamber and is used to provide vacuum penetration for linear motion system, cooling lines, power and signal cables (see Figure 4.5. On the downstream end of the PS vacuum chamber, another vacuum chamber is installed and is encroached by the upper and lower modules of the SVT.

4.3 Silicon Vertex Tracker

4.3.1 Layout

The HPS SVT is comprised of two halves of six measurement layers encroaching the beam plane as shown of Figure 4.5. Each layer consist of a pair of closely-spaced silicon strip detector planes with one of the planes oriented orthogonal to the beam plane and the other at small angle stereo (see Table 4.1). This allows

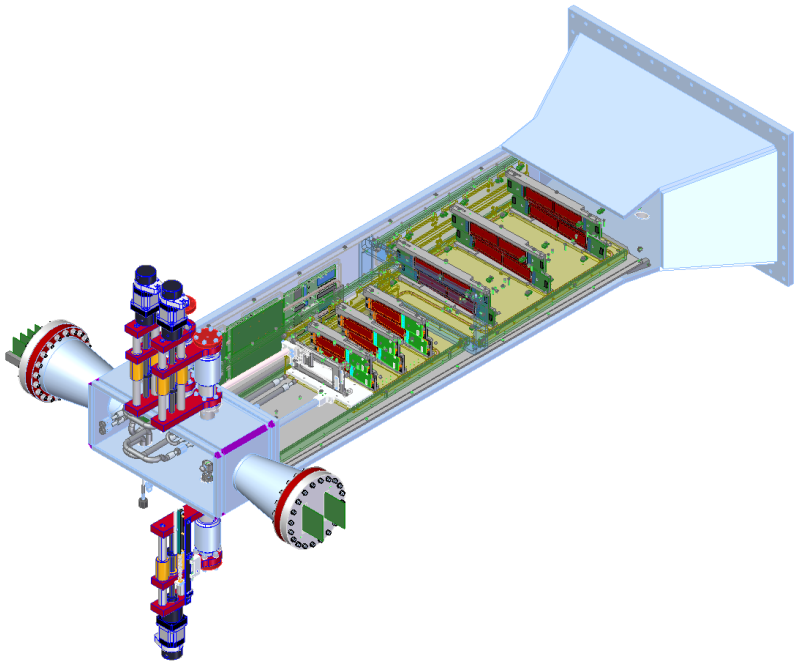

Figure 4.5: A rendered view of the Silicon Vertex Tracker inside the pair spectrometer vacuum chamber.

for the measurement of both the vertical and horizontal coordinate of a hit, in

turn, enabling full 3D hit reconstruction.

The first three layers consist of a single sensor of coverage above and below the beam plane and use a stereo angle of 100 mrad. In order to better match the acceptance of the Ecal, the coverage of the last three layers is two sensors wide and use a stereo angle of 50 mrad. The choice of a 50 mrad angle for the last three layers instead of 100 mrad was meant to break the degeneracy that results in fake tracks due to ghost hits in layers with the same stereo angle. It must be noted that only five layers are needed to match the full acceptance of the Ecal, however, an improvement in the momentum resolution was observed with the addition of another layer. In total, the SVT makes use of 36 sensors, which amounts to 23,004 channels.

Since heavy photons are produced very forward, and the opening angle of their decay products goes as $\sim m_A/E_0$, sensitivity to low mass heavy photons requires the tracker layers to be as close to the beam plane as possible. When deciding the distance of the first layer to the beam, several effects needed to be taken into consideration. These include the extent of the beam halo, the amount of radiation damage that is expected to be incurred from the Coulomb scattering of the primary beam as well as radiative secondaries, the ability to resolve hits with pileup present and being capable of doing pattern recognition in a high occupancy

environment. With all of this in mind, it was determined that the closest tolerable angular proximity was 15 mrad, putting the edge of layer 1 at 0.5 mm from the beam center. In simulation, this corresponds to 1% occupancy of strips closest to the beam plane of layer 1.

4.3.2 Sensors

At the energies at which HPS operates, the uncertainty in both the mass and vertex resolutions are dominated by multiple Coulomb scattering in the first few layers. This made it important to choose a sensor technology that would minimize the material budget of the SVT modules, especially since the material budget of the sensors dominates the total material budget of the SVT modules. Furthermore, the need to place the SVT in close proximity to the beam plane made it necessary to choose sensors which are highly tolerant to radiation. With these considerations in mind, a readily available batch of silicon microstrip sensors, initially manufactured for the D0 Run IIb upgrade, were found to satisfy all necessary requirements [76].

The sensors were manufactured by Hamamatsu Photonics Corporation on $\langle 100 \rangle$ crystal rotation silicon and are p^+ on n-bulk, single sided, AC-coupled and polysilicon-biased. The cut dimensions of the sensors are 100×40.34 mm^2 with

Layer	**1**	**2**	**3**	**4**	**5**	**6**
z position from target (cm)	10	20	30	50	70	90
Stereo angle (mrad)	100	100	100	50	50	50
Bend plane resolution (μm)	$\approx$6	$\approx$6	$\approx$6	$\approx$6	$\approx$6	$\approx$6
Non-bend plane resolution (μm)	$\approx$ 60	$\approx$ 60	$\approx$ 60	$\approx$ 120	$\approx$ 120	$\approx$ 120
Nominal dead zone in y (mm)	$\pm$ 1.5	$\pm$ 3.0	$\pm$ 4.5	$\pm$ 7.5	$\pm$ 10.5	$\pm$ 13.5
Material budget (%X_0)	.7	.7	.7	.7	.7	.7

Table 4.1: The layout of the HPS SVT.

Cut dimensions (L×W)	100 mm x 40.34 mm
Active area (L×W)	98.33 mm x 38.34 mm
Readout (Sense) pitch	60 (30) μm
# Readout (Sense) strips	639 (1277)
Breakdown voltage	> 1000 V
Depletion voltage	> 130 V
Bias Resistor Value	0.8 ± 0.3 MΩ
AC Coupling Capacitance	> 12 pF/cm
Total Interstrip Capacitance	< 1.2 pF/cm
Defective Channels	< 1 %

Table 4.2: Specifications of the sensors used for the HPS SVT.

an active area of 98.33×38.34 mm^2. They are $320 \pm 20\mu$m thick and have a sense (readout) pitch of 30 (60) μm. The sensor specifications are summarized on Table 4.2.

Over the lifetime of the HPS detector, the sensor strips closest to the beam plane are expected to see $> 10^{15}$ electrons per cm^2. The radiation damage the sensors are expected to incur due to the large electron flux will lead to an increase in both the leakage current and the voltage required to fully deplete the sensor. It was thus beneficial to choose a sensor technology that can be operated at high bias voltage in order for them to remain fully depleted even after irradiation. In fact, previous studies have shown that sensors that may be operated to 1000 V can tolerate a dose of 1.5×10^{14} 1 MeV neq/cm^2 [77]. Since the damage incurred by electrons with energies less than 10 GeV is a factor ~ 30 less than 1 MeV neutrons

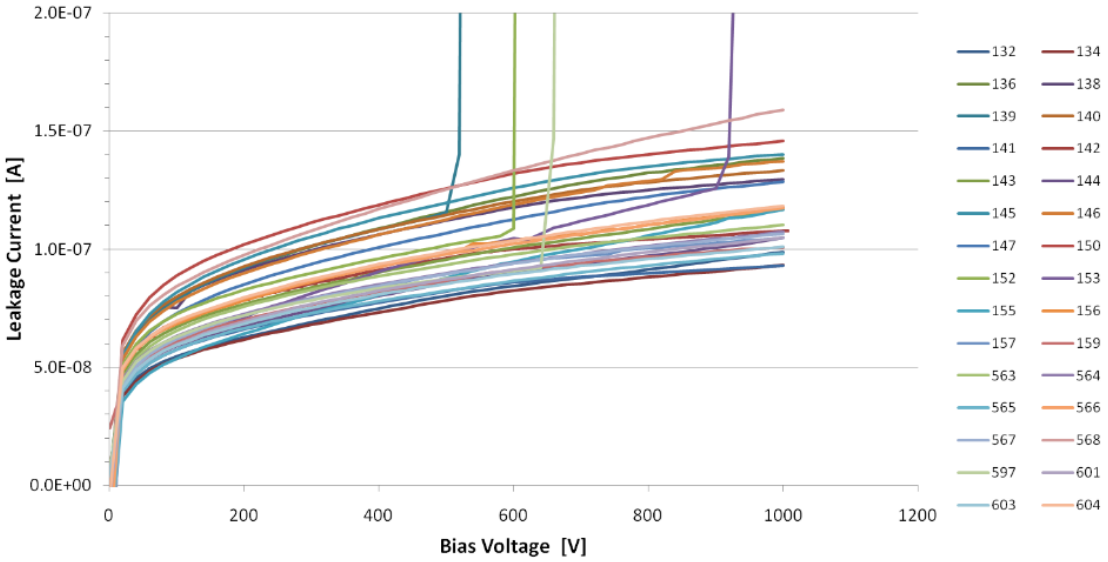

Figure 4.6: Measured IV curves before irradiation for a subset of sensors used by HPS.

[78], then ensuring all sensors can be biased to 1000 V will ensure that the sensors will be able to withstand the expected flux of electrons over the lifetime of HPS.

Before being considered for use for the SVT modules, all sensors were electrically characterized. Specifically, the leakage current was measured as a function of bias voltage up to a maximum bias of 1000 V. During these test, leakage currents of less than 500 nA were observed. The measured IV curves for a subset of sensors can be seen on Figure 4.6. Only sensors whose leakage current did not uncontrollably increase (i.e. break down) before reaching a bias of 1000 V were considered for use in HPS.

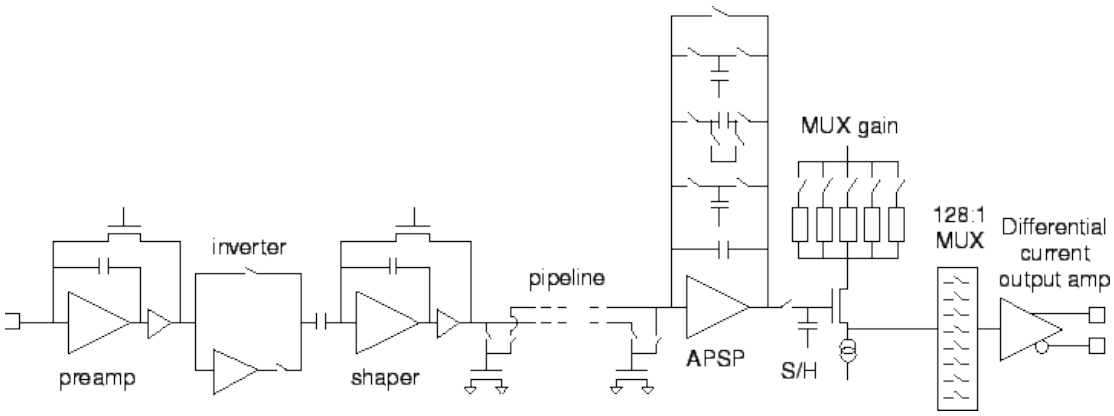

Figure 4.7: A schematic of a single channel of the APV25 readout chip.

4.3.3 Readout

The sensors are continuously read out using the APV25 readout chip developed for the Compact Muon Solenoid detector at the Large Hadron Collider [79]. The APV25 has 128 channels, with each channel consisting of a charge-sensitive preamplifier coupled to CR-RC shaping amplifier and a 192-cell-deep analog pipeline. A schematic of a single channel is shown in Figure 4.7.

When a particle traverses a sensor, it generates a charge signal which is processed by the APV25 amplifier chain. As shown in Figure 4.8, the shaper output is continuously sampled at 41.6 MHz into the analog pipeline. The position along the pipeline into which the shaper output is stored is determined by a write pointer which continuously cycles through the pipeline. Similarly, a read pointer determines the position that will be marked for read out when a trigger signal is

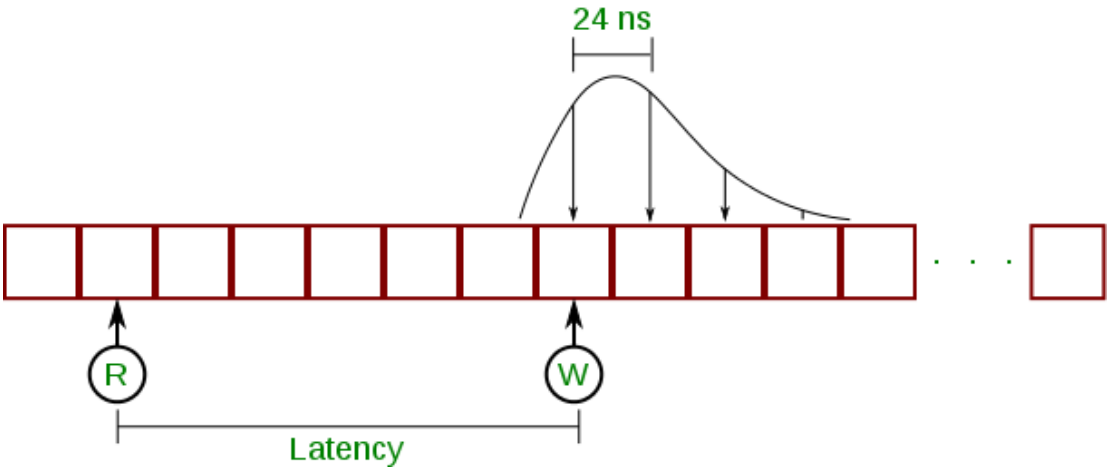

Figure 4.8: A schematic demonstrating the sampling of the shaper signal and the management of read/write pointers.

received. Since the trigger decision cannot happen instantaneously, the distance between the read and write pointers or latency is programmable. Given that only 160 pipeline cells out of the 192 are used to buffer samples, the delay between a signal and the arrival of the trigger can be as long as 3.8 μs. The remaining 32 cells along the pipeline are used to buffer the addresses of samples that are waiting to be read out.

The samples are read out by the Analog Pulse Shape Processor (APSP) which can operate in two modes: multi-peak and deconvolution mode. In deconvolution mode, three consecutive pipeline cells are read out and combined into a weighted sum before being output. In multi-peak mode, three consecutive samples are read out and output without any additional operations, allowing for the reconstruction

of the shaper output. The output of the APSP is then sent to a 128:1 multiplexer which makes the raw data frames.

During the engineering run, the APV25s were operated using the nominal settings listed in Table 4.3. The nominal shaping time is set to 50 ns. The high occupancies expected during the engineering run meant that overlapping of hits or "pile-up" were a concern. In order to mitigate this problem, the APV25s were operated in multi-peak mode allowing the reconstruction of the shaper output. Furthermore, with each Ecal trigger, the APV25s were sent two consecutive trigger signals allowing the readout of six consecutive samples instead of three. The trigger latency was then adjusted such that two samples before the signal were read out, allowing the shape of the pileup pulse to be captured by the fit. This was used to remove any effects of pileup from the signal pulse. Approximately 5% of hits in layer 1 were observed to be affected by pileup.

4.3.4 SVT Modules

Two different sensor module designs were used for the layers of the SVT. A module was built by sandwiching a pair of half-modules around an aluminum cooling block located on the hybrid side. For layers 1-3, the half-modules are fixed on the hybrid side while a spring and lever mechanism tensions them on the

Name	Description	Value
IPRE	Preamp input FET current	98 (460 μA)
IPCASC	Preamp cascode current	52 (60 μA)
IPSF	Preamp source follower current	34 (50 μA)
ISHA	Shaper input FET current bias	34 (50 μA)
ISSF	Shaper source follower current	34 (50 μA)
IPSP	APSP current	55 (80 μA)
IMUXIN	Multiplexer input current	34 (50 μA)
VFP	Preamp feedback voltage	30
VFS	Shaper feedback voltage	60
VPSP	APSP Voltage level	40
LATENCY	Trigger latency	147
MUXGAIN	Multiplexer gain	100 μA/MIP

Table 4.3: APV25 specs used during the engineering run.

opposite end. For layers 4-6, the tensioning mechanism is integrated into into one of the cooling blocks.

The first three layers of the SVT reused the half-module design from the HPS test run [80]. They consist of a single sensor and FR4 hybrid electronic board glued onto a polyimide-laminated carbon fiber composite backing. The hybrid contains filtering for the high voltage bias, temperature sensors and the APV25 readout chips used to read out the sensor. The APV25 chips are mounted onto the hybrid electronic board and the channel pads are wiredbonded directly to the sensor. Each sensor requires 5 APV25 chips in order to read out all channels. In order to further minimize the material budget of the half-modules, a window was machined into the carbon fiber, leaving the middle of the sensor exposed.

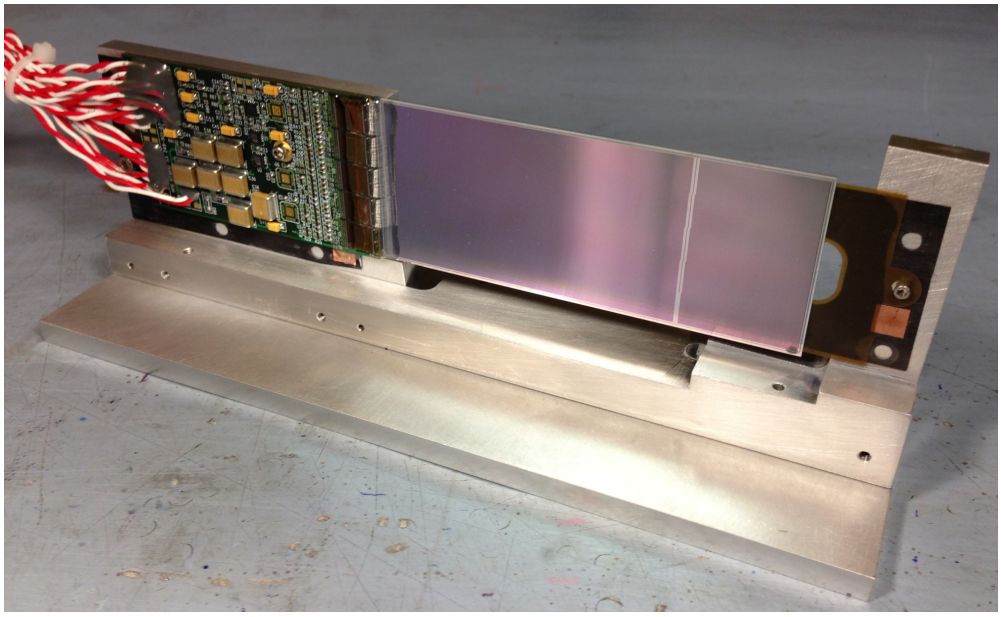

Figure 4.9: A layer 1-3 half-module used by the SVT.

In order to better match the acceptance of the Ecal, the half-modules used in layers 4-6 consist of two sensors glued end-to-end onto the polyimide-laminated carbon fiber backing with hybrids on either side of them. Due to space constraints, the hybrids used by layers 4-6 have a smaller footprint compared to the hybrids used for layers 1-3.

4.3.5 Mechanical Support, Cooling and Services

The SVT modules are mounted directly to 4, 1/4" aluminum "u-channels" with each of the u-channels supporting 3 modules as shown in Figure 4.10. The u-channels are actively cooled by HFE 7000 flowing through 1/4" copper tubing

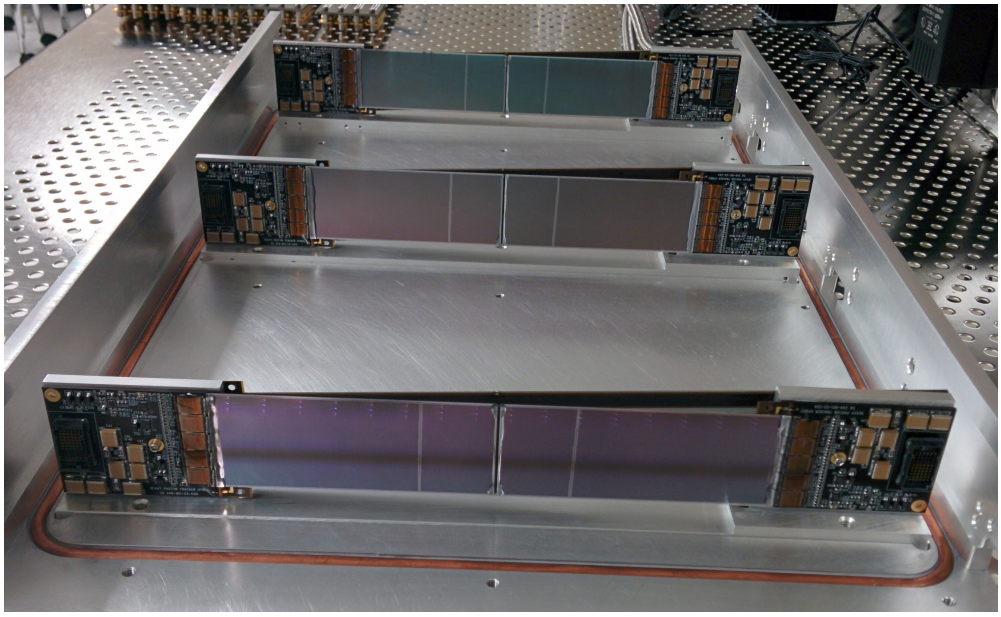

Figure 4.10: A layer 4-6 half-module used by the SVT.

press-fit into pre-machined grooves into the aluminum. Each of the 4 u-channels are installed inside an aluminum support box using a guide rail system allowing quick access to the mounted modules . The layer 4-6 u-channels are fixed inside of the box while the layer 1-3 u-channels have a rigid support rod attached on the upstream end which are connected to linear shifts. The linear shifts are used to precisely move the layer 1-3 u-channels vertically in 6 μm steps using stepper motors. This, in turn, allows the placement of the edge of the layer 1 sensor at $\sim$ 7 mm from the beam plane. Each of the two layer 1-3 u-channels are connected to their own linear shifts. The support box is installed inside the Hall B analyzing magnet vacuum enclosure.

The support box is also used to house an aluminum plate onto which data acquisition boards are mounted. The aluminum plates slides into the support box via a machined grove. An embedded loop is used to circulate water through the plate, providing cooling of the boards.

4.4 Electromagnetic Calorimeter

The HPS Ecal is used to provide the primary trigger for the experiment as well as to identify electrons. It consist of two halves of lead-tungstate ($PbWO_4$) crystals with each half mounted on an aluminum frame $\sim$ 137 cm from the upstream edge of the analyzing magnet. Each half is composed of five layers of crystals with the four outermost layers consisting of 46 crystals and the layer closest to the beam plane consisting of 37. The removal of the 9 crystals from the inner layer was necessary to allow the outgoing electron and photon beams to pass through unimpeded. Each half is enclosed in a temperature controlled environment held at 17°C which encroaches on the Ecal vacuum chamber.

Each of the crystals is 16 cm long and trapezoidal in shape with a front face dimension of 1.3×1.3 cm^2 and a back face dimension of 1.6×1.6 cm^2. In order to maximize the light yield, the crystals were wrapped in VM2000 non-metallic reflector film. A Hamamatsu S8664-1010 Avalanche Photodiode (APD) with a

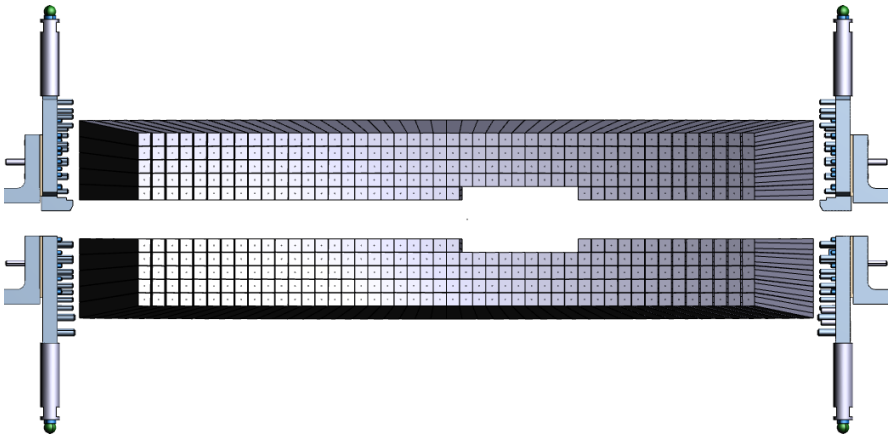

Figure 4.11: A rendering showing the arrangement of the Ecal crystals. The Ecal is split into upper and lower modules in order to accommodate the "dead zone." The crystals removed from the first layer allow a larger opening for the outgoing electron and photon beams.

photosensitive area of 10×10 mm^2 was glued to the back of each crystal and used to read out the signals collected by the crystals.

4.5 Trigger and Data Acquisition

4.5.1 Ecal Data Acquisition

The analog signals that are read out from each of the Ecal crystals by the APDs are sent to a 16-channel JLab FADC250 VXS module (FADC) (see Figure 4.13). The 221 FADC channels used by each half of the Ecal are housed in their own 20 slot VSX crates.

The APD signals are sampled and digitized by the FADCs at a rate of 250 MHz

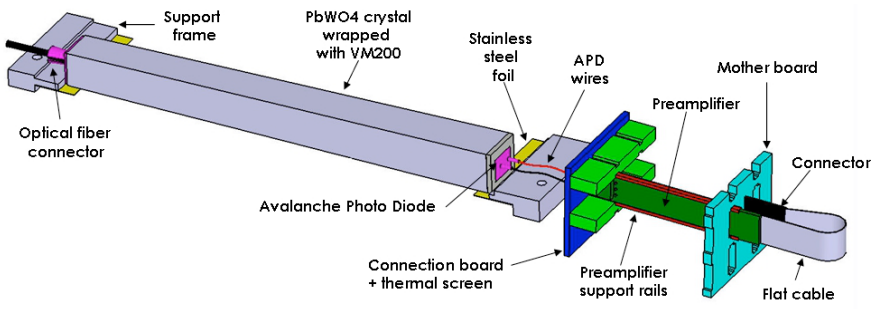

Figure 4.12: Rendered view of an HPS Ecal module consisting of a 16 cm PbW_4 crystal, Avalanche Photodiode and preamplifier board.

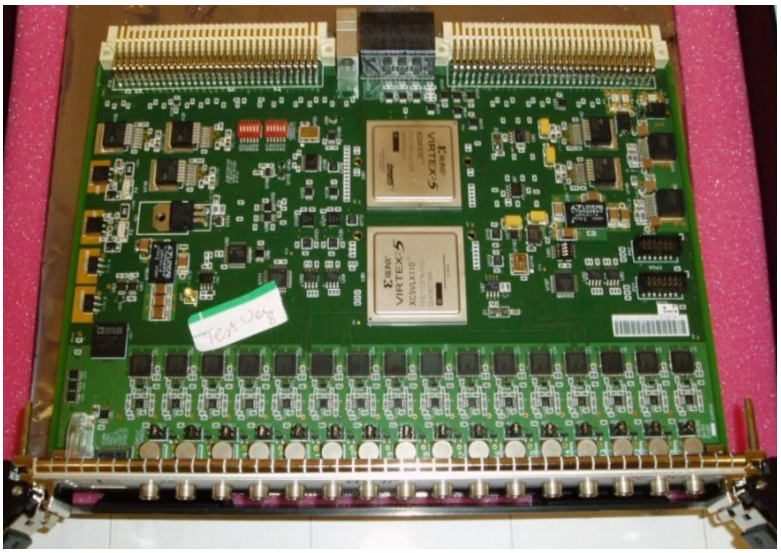

Figure 4.13: A 16-channel Jefferson Lab FADC250 VXS module.

into 8 μs deep pipelines. If an FADC signal crosses a pre-defined threshold, the integrated amplitude of a select number of samples before and after the threshold crossing, as well as the crossing time, are passed to the Crate Trigger Processor (CTP).

4.5.2 Trigger

The HPS trigger is designed to efficiently select e^+e^- pairs whose energy depositions, or clusters, in the Ecal are consistent with the decay of an A'. The trigger logic searches for signals that are coincident in time and satisfy a specific kinematic selection optimized to select A' events.

As discussed in the previous section, if a signal from an Ecal crystal is found to cross some pre-determined threshold, the crossing time and amplitude are reported to the CTP. The CTP contains the cluster finding algorithm which performs the following task:

- The amplitude of hits from every 3x3 array of crystals in the Ecal that is within a programmable number of clock cycles is summed.

- If the 3x3 sum exceeds a pre-defined cluster amplitude threshold and the sum is greater than any of the neighboring 3x3 windows, then the amplitude (energy), position, time and hit pattern are reported to the Sub-System

Processor (SSP).

The SSP takes the cluster information reported by both halves of the Ecal and creates all possible pairs of clusters that fall within an 8 ns coincident window. Then, in order to further reduce background rates, the following selection is applied to the pairs of clusters:

- $E_{min} \leq E_{top} + E_{bottom} \leq E_{max}$
- $|t_{top} - t_{bottom}| \leq \Delta t_{max}$
- $|E_{top} - E_{bottom} \leq \Delta E_{max}$
- $E_{low} + R \times F \leq \text{Threshold}_{slope}$
- $|\tan^{-1} \frac{X_{top}}{Y_{top}} - \tan^{-1} \frac{X_{bottom}}{Y_{bottom}}| \leq \theta_{Coplanarity}$

Here, E_{top} (E_{bottom}), t_{top} (t_{bottom}), x_{top} (x_{bottom}) and y_{top} (y_{bottom}) are the energy, timestamp and position of the cluster in the top (bottom) half of the Ecal and E_{min} (E_{max}) is the minimum (maximum) cluster energy sum. E_{low} is the energy of the lowest energy cluster, R is the distance between its center and the calorimeter center while F is a constant. The values used during the engineering run are listed in Table 4.4. If a pair of clusters satisfies these criteria, a trigger signal is generated by the Trigger Supervisor and sent to all subsystems.

Parameter	**Single-0**	**Single-1**	**Pair-0**	**Pair-1**
E_{min} (GeV)	0.060	0.400	0.054	0.054
E_{high} (GeV)	2.500	1.100	1.100	0.630
$N_{threshold}$	3	3	1	1
E_{sumlow} (GeV)			0.120	0.180
$E_{sumhigh}$ (GeV)			2.000	0.860
$E_{\text{differenec}}$ (GeV)			1.000	0.540
F(GeV)				0.0055
$\theta_{\text{coplanirity}}$				30°
$t_{\text{coplanirity}}$(ns)			16	12
Prescale	2^{13}	2^{11}	2^{10}	2^{0}
Rate (50 nA)	0.4 Hz	1.3 kHz	0.7 kHz	16.6 kHz

Table 4.4: The trigger setting for all trigger types used during the engineering run. The pair-1 trigger was the main trigger used by the experiment.

During the engineering run, several triggers were run simultaneously. The main trigger used to select A' type events is the Pair-1 trigger. The Pair-0 trigger is a much looser version of the Pair-1 trigger and was tuned to select electron-electron elastic scattering (Møller scattering) events. The Single-1 trigger was tuned to select electrons that Coulomb scatter in the target i.e. full energy electrons (FEE) into the acceptance of the Ecal. These events are used to study both the momentum resolution of the tracker and the energy resolution of the Ecal. Finally, there was a cosmic trigger and a pulser trigger used to trigger on cosmic ray muons and randoms respectively. A summary of all of the settings is given in Table 4.4

4.5.3 SVT Data Acquisition

After a trigger is received, the differential current signals from each of the APV25s are transferred to a total of 10 Front End Boards (FEB) to undergo digitization and further processing. The FEBs contain all of the necessary electronics to digitize the signal and to distribute power to the hybrids. The signals from layers 1-3 are transferred to the FEBs via Teflon-coated twisted pair wires while those emerging from layers 4-6 use twisted pair magnet wire. The use of twisted pairs reduces crosstalk between the lines as well as electromagnetic interference.

At the FEB's, the differential current signals are first converted to a voltage by a pre-amplifier circuit to match the dynamic range of the AD9252 14-bit analog to digital converter (ADC). The ADC samples the signal at 41.667 MHz and digitizes it to a value between 0 and 16384. The digitized signals are then transferred to Xilinx Artix-7 field programmable gate arrays (FPGA) which sends the signals upstream to multi-gigabit transceivers. In addition to transmitting data upstream, the FPGAs are also responsible for controlling and monitoring the hybrid power and distributing triggers and clock to the hybrids.

Data from the FEBs are transferred through mini SAS cables to electronic boards potted through slots on a 8 inch vacuum flange located upstream on the vacuum box. The flange boards contain the necessary electronics to convert the

digitized signal to optical. The optical signal is then transferred over 30 m fibers to an ATCA crate. The data from all 10 FEBs is distributed between two ATCA blades, called Cluster on board (COB), housed inside the ATCA crate. Each COB contains 8 processing nodes known as Reconfigurable Cluster Elements (RCE). The processing nodes use Xilinx Zynq-7000 series FPGAs to apply data reduction algorithms to the incoming signals and build event frames.

Chapter 5

Detector Performance

The HPS engineering run took place within Hall B at the Thomas Jefferson National Accelerator Facility (JLab) in Newport News, VA in the Spring of 2015. Although the commissioning of the Ecal had already taken place during a run in December of 2014, the engineering run would mark the first time that the SVT would take on an electron beam and that both subsystems (SVT, Ecal) would be operating in conjunction. Therefore, the performance results from the engineering run were critical in verifying that all performance metrics were as simulated and to the planning of future HPS runs. In the chapter that follows, a review of a few selected results that demonstrate the performance of both subsystems during the engineering run will be given.

5.1 Performance of the Silicon Vertex Tracker

Since it was the first time that the SVT would take on physics quality beam, care was taken to understand several performance metrics before continuing to move the first three layers of the SVT towards their final position. In fact, data was taken with layers 1-3 of the SVT at several positions above the beam plane and the occupancies were verified to match what was expected from simulation. This was of utmost importance since the 1% occupancy requirement at 0.5 mm was crucial to operation of the SVT.

All of the data taken with the SVT saw all APV25s configured to their nominal operating points as listed in Table 4.3, while all sensors were reverse-biased to 180 V. All hybrids were being cooled to $\sim$ -14°C while all FEBs were being operated at $\sim$ 20°C. Finally, only 4 out of the 23,004 SVT channels were found to be dead or noisy.

5.1.1 Calibrations

Preparing the SVT for real physics data-taking required the calibration of the readout system. This involved the extraction of the baseline (pedestal), noise and gain for each of the 23,004 SVT channels. All measurements were made with the APV25s configured to their nominal operating points and all sensors

reverse-biased to 180 V.

The baseline and noise of each of the channels were evaluated by using special "calibration" runs during which the APV25s were continuously triggered and read out without any signal present at the input. The amplitude of each of the six samples that are read out will be Gaussian distributed around the true baseline value with a width equal to the noise. For each of the samples, the baseline distributions were fit and the baseline and noise extracted (see Figure 5.1). A

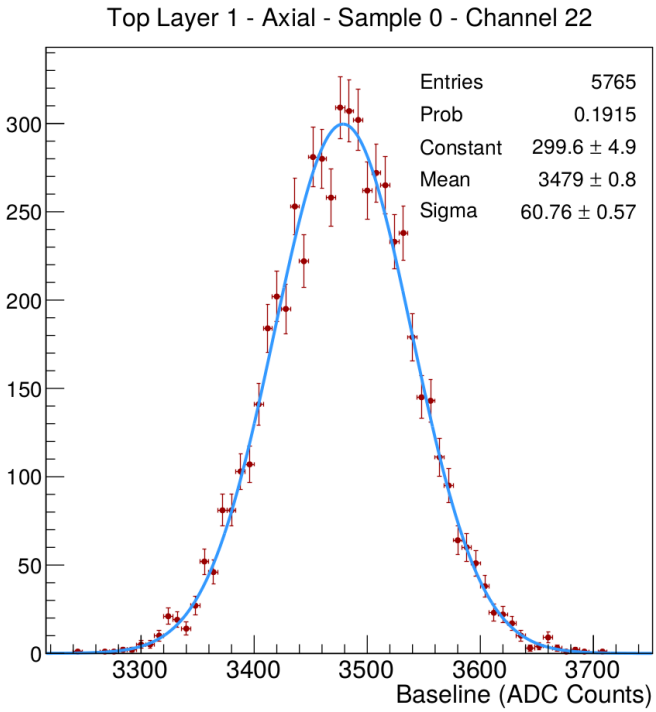

Figure 5.1: Example illustrating the Gaussian nature of the distribution of baseline values. The distribution is fit with a Gaussian in order to extract the baseline and noise for the channel and sample.

typical distribution of baseline values across a half-module is shown in Figure 5.2.

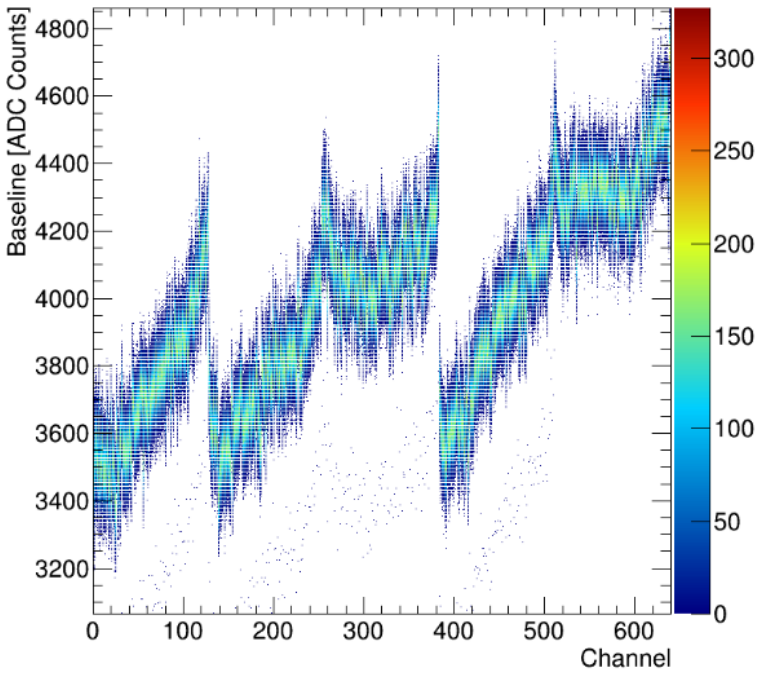

Figure 5.2: Distribution of baseline values across a sensor.

Figure 5.3 shows the noise across a half-module for each of the six samples that are read out. The noise level of layers 1-3 (4-6) was established to be between 55-60 (50-55) ADC counts which amounts to $\sim$ 800 - 875 (725 - 800) electrons. One thing to note is the large noise values at the edges of each chip. This has also been observed by the Compact Muon Solenoid collaboration and the cause is still under investigation[1].

[1]There was an extensive email discussion with APV25 experts on CMS regarding this issue, but a clear cause was never pinpointed.

The APV25 has a built in calibration circuit that allows for a pre-determined signal of known charge to be injected into a subset of channels. This allows for the accurate determination of the response to a given charge via a CR-RC shape fit to the six pedestal subtracted samples. The distribution across a hybrid of responses to 18,500 electrons is shown in Fig. 5.4. Typically, the response varies by $\sim 7\%$ across a half-module. The response scale obtained with the internal calibration circuitry was cross-checked with ionization source measurements.

The calibration circuitry was also used to create a response curve for every channel. An example of a response curve for one of the APV25 channels is shown in Figure 5.5. A linear fit to the response curve yields the gain and offset of the

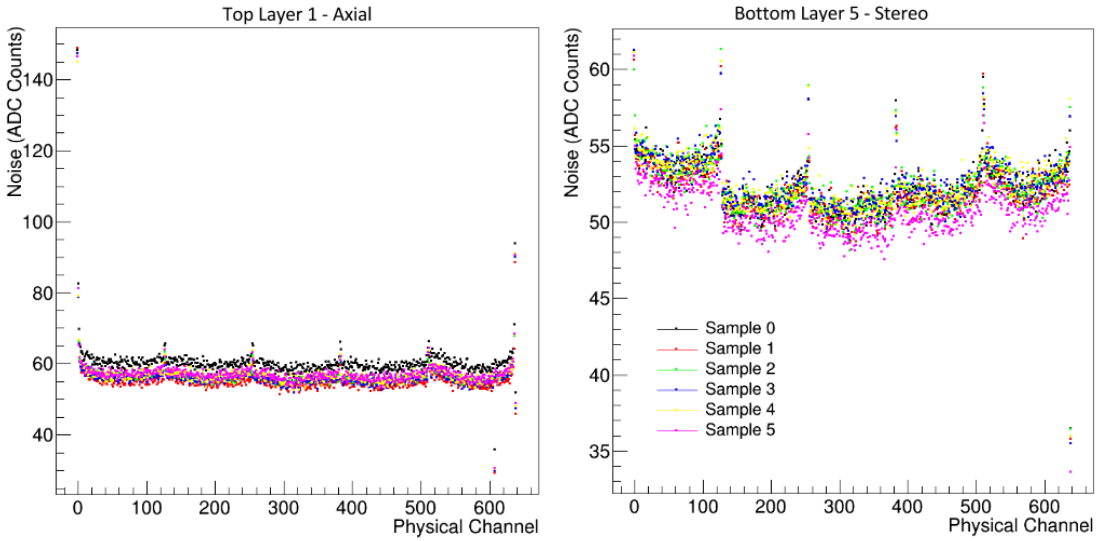

Figure 5.3: Noise of all channels across a hybrid.

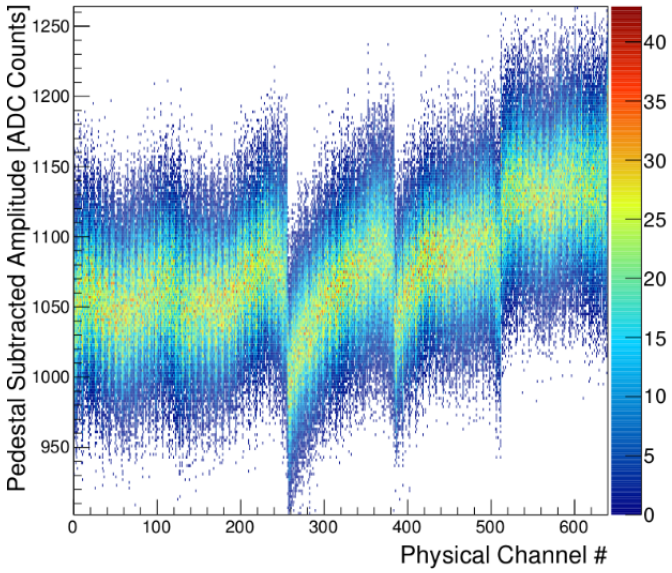

Figure 5.4: Distribution of responses to 18,500 electrons across one of the half-modules of the Silicon Vertex Tracker.

channel. From the figure, it can be seen that the response is approximately linear up to $\sim$ 2 MIPs ($\sim$ 25,000 e^-) which is the region of relevance for HPS. This is in agreement with previous measurements which found the gain to be linear up to approximately 3 MIPS [81].

5.1.2 Occupancy

When deciding the extent of the "dead zone" between upper and lower portions of the SVT, aside from avoiding the radiation field, two of the main considerations were the ability to perform robust pattern recognition and minimization of pileup within the window of time needed for the shaper output to evolve ($\sim$ 250 ns for

a 50 ns shaping time). Using simulation, it was determined that limiting the occupancy of the strips closest to the beam within an 8 ns window to less than 1% fulfilled all of the requirements.

Since the engineering run marked the first time that the SVT had taken an electron beam, care was taken when lowering the first three layers to their final position a mere 15 mrad from the beam. In fact, the occupancies with layers 1-3 at 4, 3, 2, and 1.5 mm away from the beam plane were verified to match what was predicted from simulation before the SVT was lowered to its final position. As can be seen in Figure 5.6, once the first three layers were lowered into their

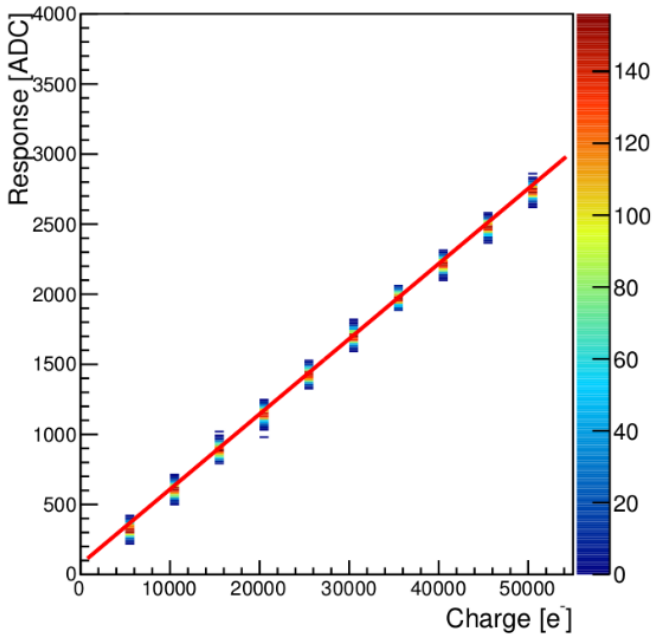

Figure 5.5: Response curve for a single APV25 channel.

final position (edge at 0.5 mm away from the beam plane), the occupancies on the innermost strips were observed to be less than 1% as expected.

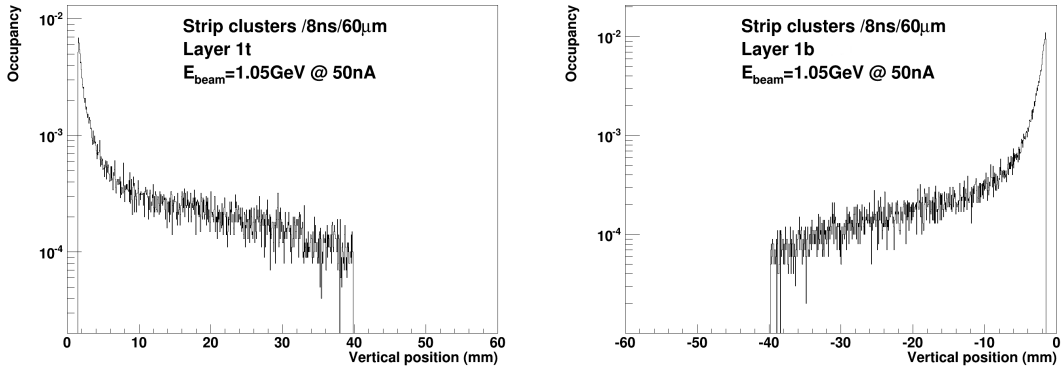

Figure 5.6: Occupancies of both top and bottom layer 1. The occupancies of the innermost strips were observed to be less than 1%, as predicted by simulation.

5.1.3 Hit Quality

When an electron traverses a sensor, the deposited charge may be spread over several strips. The signal from each of the strips is processed by the APV25, and the six samples emerging from each channel are fit using the following 3-pole function

$$f(t) = A\frac{\tau_1^2}{(\tau_1-\tau_2)^3}\left(e^{-\frac{t-t_0}{\tau_1}} - \sum_{k=0}^{2}\left(\frac{\tau_1-\tau_2}{\tau_1\tau_2}(t-t_0)\right)^k \frac{e^{-\frac{t-t_0}{\tau_2}}}{k!}\right) \qquad (5.1)$$

where τ_1 and τ_2 represent the fall and rise time of the shaper signal respectively. The amplitude, A, and the time of the hit, t_0, are then determined from the fit.

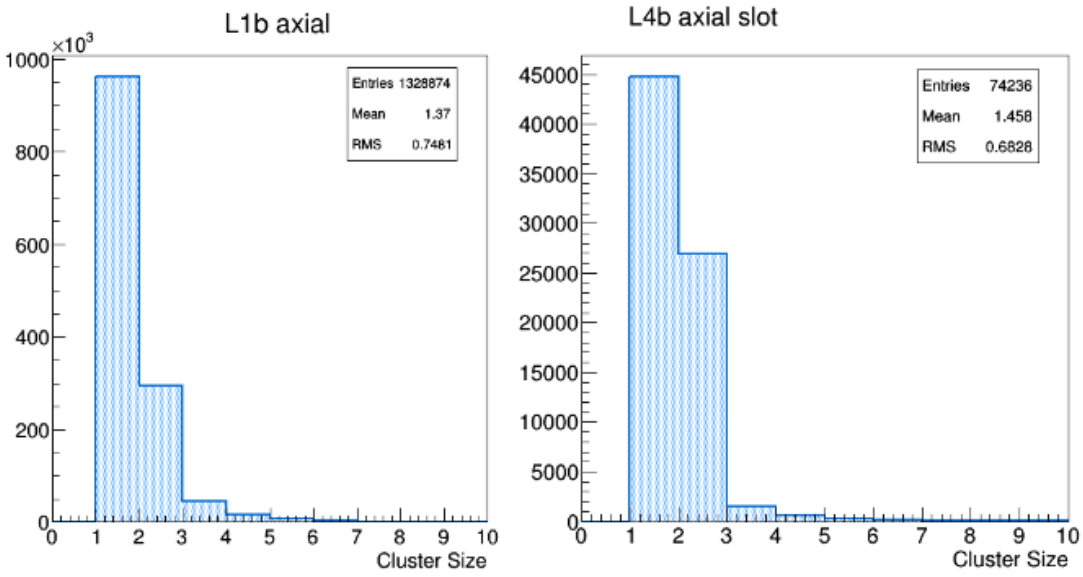

Figure 5.7: The strip multiplicity typically seen during the engineering run.

Hits on neighboring strips are clustered using a nearest neighbor algorithm as follows:

- A list of seeds is created from all raw hits that have an amplitude, S, $> 4 \times \sigma_{\text{Noise}}$
- Recursively add neighboring strips that have $S > 3 \times \sigma_{\text{Noise}}$ until a strip with $S < 3 \times \sigma_{\text{Noise}}$ is found.
- Require that neighboring hits have a t_0 that is within 8 ns of the seed hit.
- Repeat the first two steps until seed strips are no longer found.
- Require that a cluster has an amplitude $> 4 \times \sigma_{\text{Noise}}$.

The typical strip multiplicity observed during the run is shown in Figure 5.7. Figure 5.8 shows the characteristic Landau shape of the cluster charge distribution

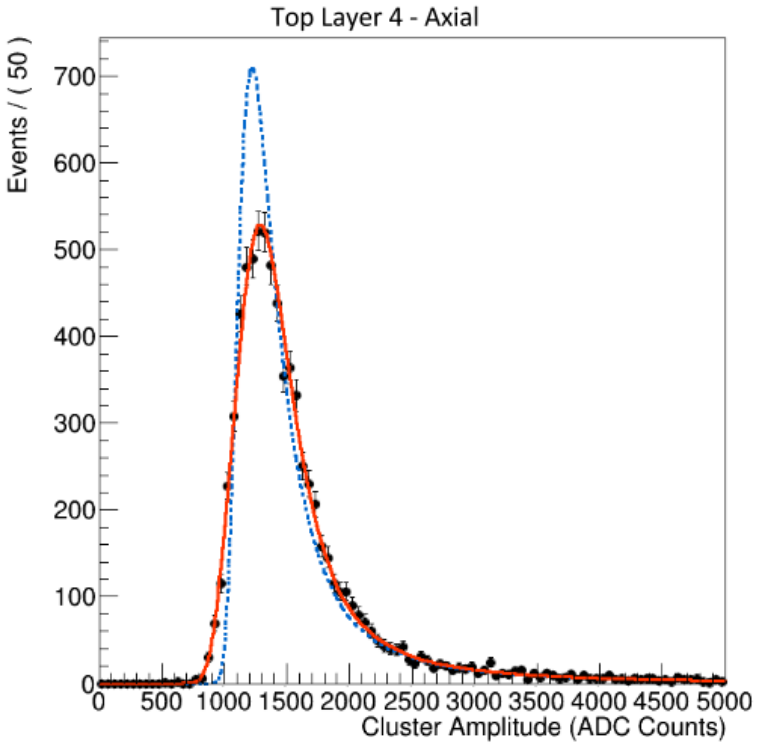

Figure 5.8: Distribution of cluster charge exhibiting the characteristic Landau shape. The cluster charge was fit with a Landau (dashed blue line) convoluted with a Gaussian (convolution shown in red) in order to extract the most probable value.

for one of the sensors. The cluster charge distributions of every layer were fit using a Landau convoluted with a Gaussian in order to extract the most probable value. The cluster charge for all layers were measured to be between ∼1400-1500 ADC counts which corresponds to ∼21,000-22,500 e^-.

Measuring the signal-to-noise of a sensor was done by simply taking the cluster charge amplitude for all single strip clusters and dividing it by the noise of the channels. Using this procedure, the signal-to-noise of all layers was measured to be within ∼24-26, as expected (See Figure 5.9).

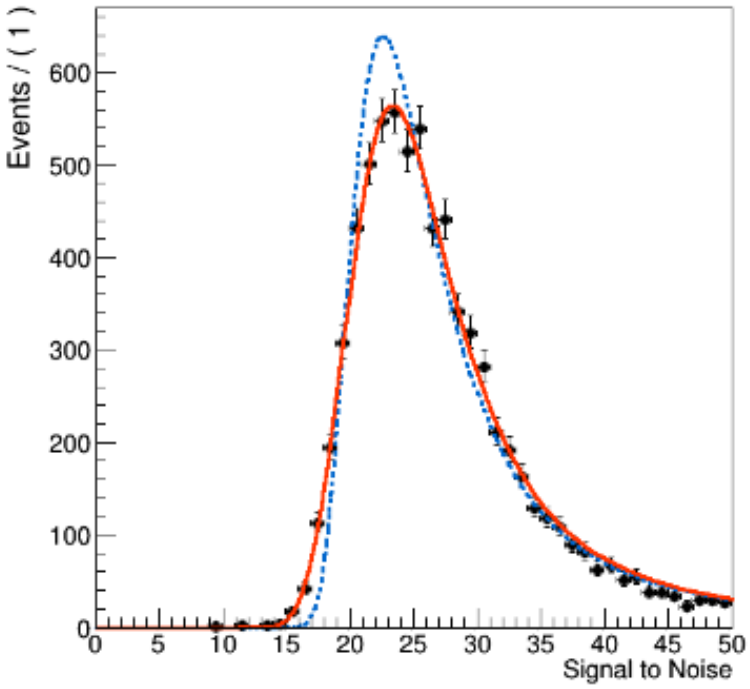

Figure 5.9: Example of signal to noise measured during the engineering run. The signal-to-noise was fit with a Landau (dashed blue line) convoluted with a Gaussian (convolution shown in red) in order to extract the most probable value.

After hits on a sensor have been clustered, the cluster time is computed as the amplitude-weighted average of the t_0 times from the hits that compose it. In order to study the hit time resolution, first a "track time" is computed by averaging

the cluster times of all clusters composing a track. Then, the residual of each of the cluster times is calculated and the resulting distribution per layer is fit with a Gaussian to extract the t_0 resolution. The resulting distribution and fit for one of the layers in the SVT is shown in Figure 5.10. After correcting for offsets and

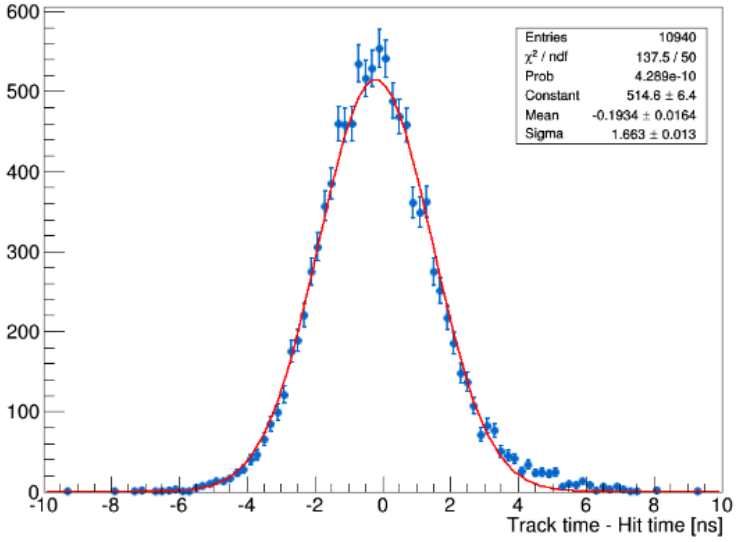

Figure 5.10: Distribution of cluster time residuals for a single layer of the SVT.

the correlation between hit times, the t_0 resolution is observed to be $\sim$ 1.8 ns.

5.1.4 Momentum Resolution

Beam electrons that multiple Coulomb scatter in the target can be used not only to verify that the momentum scale is correct but also determine the momentum resolution. These full energy electrons (FEEs) were selected by requiring a cluster in the Ecal to have a matching track and to satisfy the following criteria:

- The energy of the cluster of interest in the Ecal is between 0.8 GeV and 1.1 GeV.
- The time of the cluster seed relative to the trigger time is between 39.5 ns and 49.5 ns.
- The number of hits composing the cluster has to be greater than 3.
- The energy of the cluster seed has to be greater than 400 MeV.
- Only consider clusters whose position is above the first row of the Ecal.

The momentum distributions of the tracks matched to the clusters that pass the criteria are shown in Figures 5.11 and 5.12, split up by volume. The peaks of both distributions show that the momentum scale is accurate to within 1% which is an indication that the detector is well aligned. The multiple scattering limited momentum resolution of the top (bottom) was measured to be $\sigma_p/p = 6.8\%$ ($\sigma_p/p = 7.1\%$) which is within 5% of of the expected value.

5.1.5 Tracking Efficiency

The electron efficiency was calculated using a tag-and-probe technique. First two clusters that are coincident in time are selected in the calorimeter. One cluster must be on the positron side, i.e. $x > 0$, and the other on the electron side. Then,

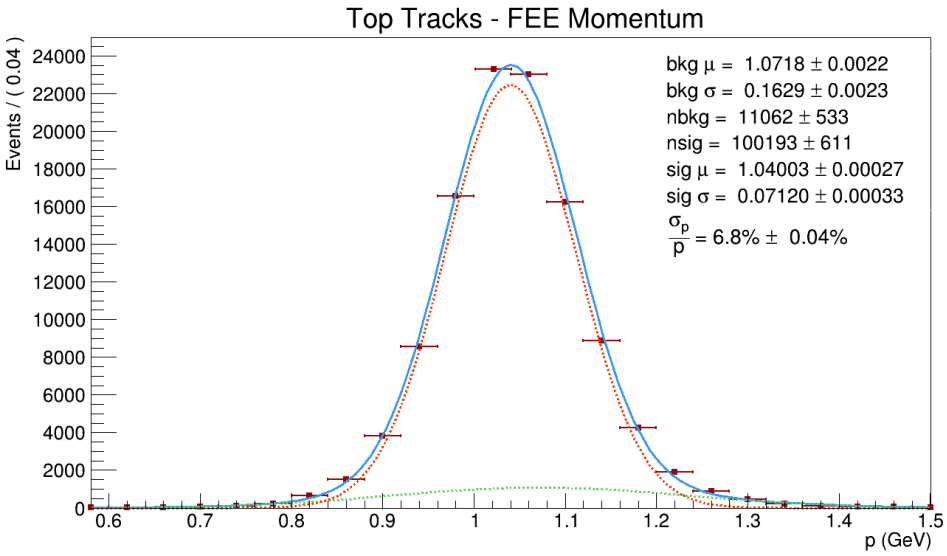

Figure 5.11: Momentum distribution of multiple Coulomb scattered electrons (FEE) in the top portion of the SVT and Ecal. The mean of the distribution is within ∼1% of the beam energy (1.056 GeV), indicating that the detector is well aligned.

the positron side cluster is required to match to a positron track. This becomes the tag. The cluster on the electron side is then checked to have a match to an electron track. The electron efficiency is then calculated as

$$\varepsilon = \frac{N_{probes}}{N_{tags}}. \tag{5.2}$$

Using this method, the electron efficiency was found to be $\sim$ 95%. A similar procedure was used to find the positron efficiency to be $\sim$ 95%.

5.1.6 Mass resolution

The heavy photon signal is expected to appear as a Gaussian peak above the QED trident invariant mass spectrum with the width corresponding to the mass resolution of the experiment. Thus, determining the mass resolution is a crucial component of the resonance search, the details of which will be given in Chapter 6.

Parameterizing the mass resolution from data was accomplished by using electron-electron elastic scattering (Møller scattering) which will have a well de-

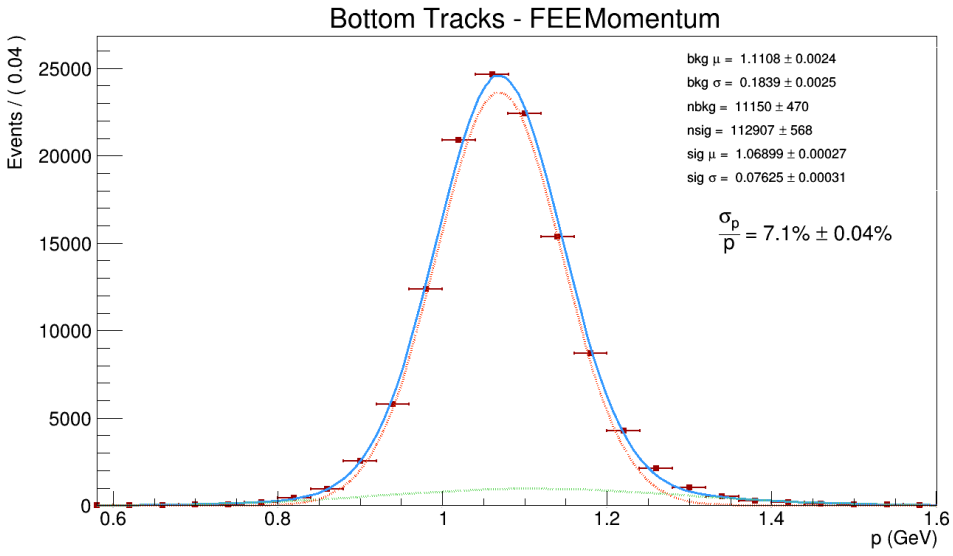

Figure 5.12: Momentum distribution of multiple Coulomb scattered electrons (FEE) in the bottom portion of the SVT and Ecal. The mean of the distribution is within ∼1% of the beam energy (1.056 GeV), indicating that the detector is well aligned.

fined mass. For this particular study, only events which satisfy the "Single-1" trigger requirements were used. Furthermore, only events where the bias of the SVT was on, the SVT was positioned at 0.5 mm from the beam plane and were free of data acquisition errors were considered.

Selection of Møller events begins with the requirement that an event have a pair of clusters in the Ecal coincident in time satisfying the following criteria:

- The two clusters must be coincident within a 1.6 ns window.
- The two clusters must be in opposite detector volumes.
- The x position of both clusters must be < 0, i.e. both clusters are on the electron side.

Once a pair of candidate clusters is found, they are required to match to e^- tracks. Both the tracks are then subjected to the following criteria:

- Both tracks are subjected to a χ^2 probability cut of 95%.
- The momentum of the tracks are required to be less than 0.7 GeV.
- The two electron tracks must come from the same vertex. In order to ensure this, the vertex $\chi^2 < 10$. The positions along x and y are then required to

lie within an ellipse defined as

$$v_x^2/0.04 + v_y^2/0.0025 = 1.$$

Finally, the momentum sum of the tracks associated with the clusters must be greater than 0.8*1.056 GeV and less 1.2 GeV. The resulting Møller distribution is shown in Figure 5.13.

In order to extract the mass resolution, the invariant mass distribution was fit with a Crystal Ball function [82] plus a Gaussian to account for accidental e^-e^- on the low side (See Figure 5.13). From the fit, the mass peak is found to be at 33.2 MeV which is within 3% of the design value. The mass resolution at 33.2 MeV is 1.4 MeV, which is within 10% of what was predicted by simulation.

Determining the mass resolution as a function of mass was done by using A' signal and Møller Monte Carlo. The resulting mass resolutions at each mass hypothesis are shown in Figure 5.14. The mass resolution as a function of mass was found to be best modeled using a third order polynomial of the form

$$\sigma_m(m_{ee}) = -6.166m_{ee}^3 + 0.9069m_{ee}^2 - 0.00297m_{ee} + 0.000579 \text{ GeV} \qquad (5.3)$$

This equation was used in the resonance search described in Chapter 5.

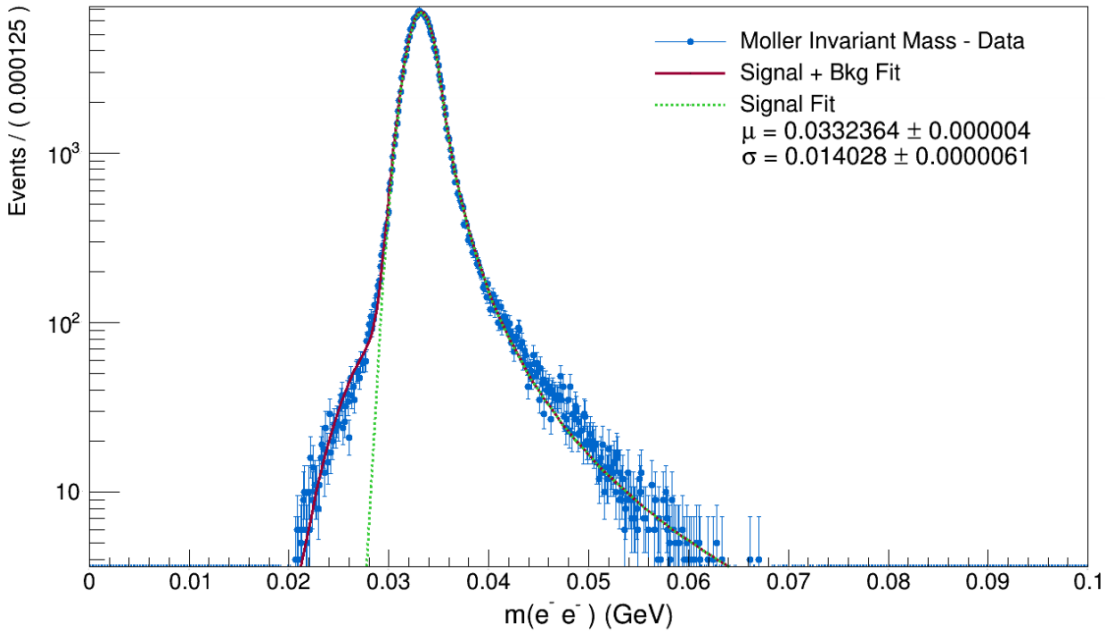

Figure 5.13: Møller invariant mass distribution.

5.2 Performance of the Electromagnetic Calorimeter

Beam electrons that multiple Coulomb scatter in the target can also be used to determine the energy resolution of the calorimeter. The resulting resolution measured in this manner was determined to be $\sim 4\%$ and is shown in Figure 5.15. The full waveforms that are read out by the FADCs were used to determine the time resolution to be $\sim 300ps$

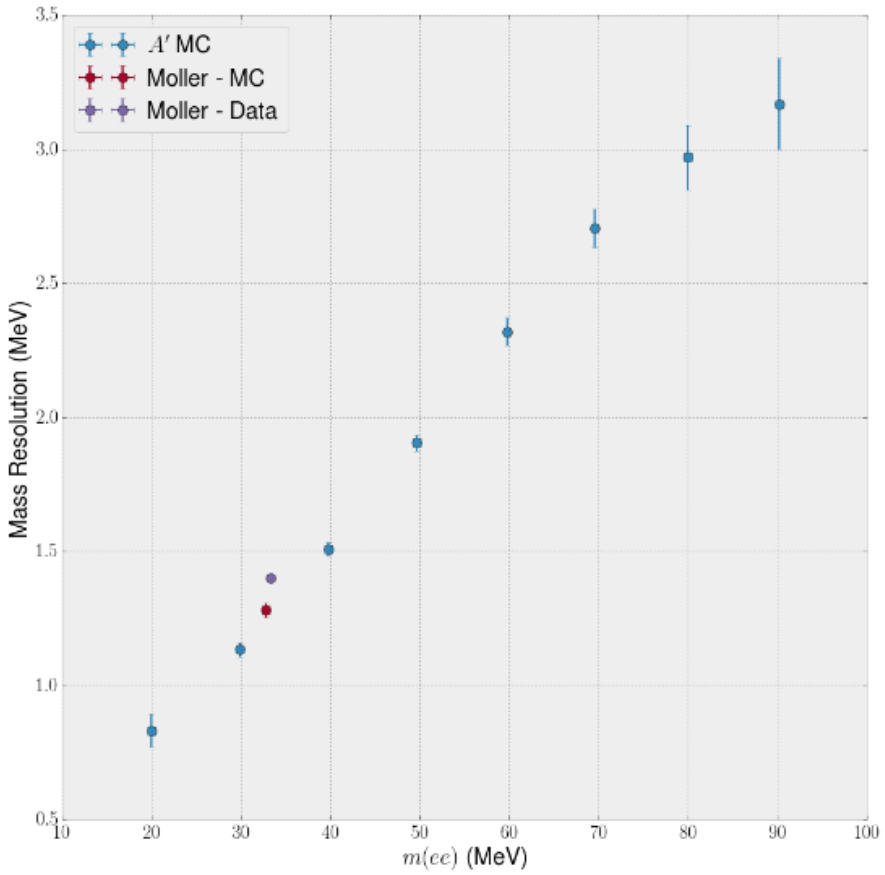

Figure 5.14: The mass resolution as a function of mass calculated using the invariant mass distributions of A' (blue) and Møller Monte Carlo (red) as well as Møller data (purple). The mass resolution calculated using data is within 10% of the expected value calculated with Monte Carlo.

5.3 Trigger Performance

The performance of the trigger was studied by using a simulation of the trigger and comparing it to the hardware trigger. First, the raw FADC hits are converted to simulated clusters using a simulation of the hardware clustering algorithm.

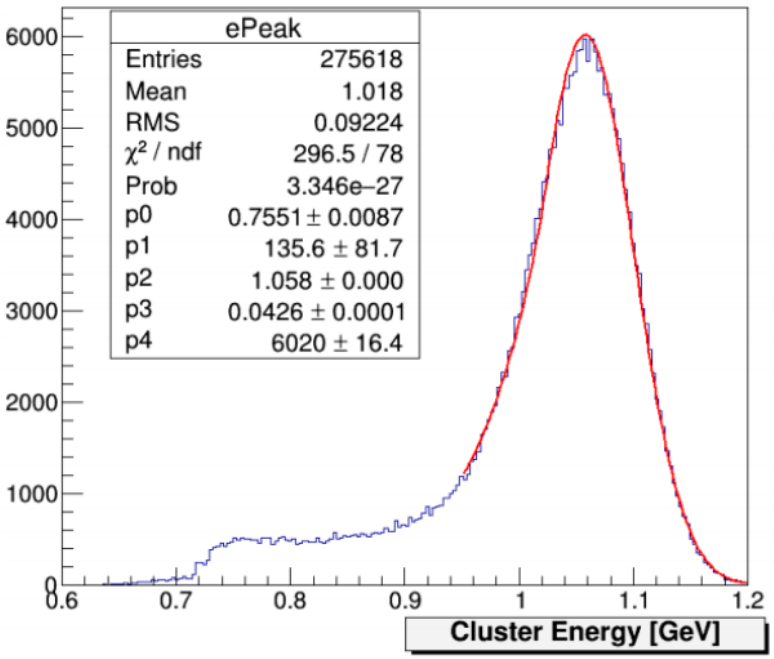

Figure 5.15: Energy distribution of multiple Coulomb scattered electrons in the in the Ecal.

Then a simulation of the trigger decision was compared to the actual decision reported by the hardware trigger. The efficiency is calculated as

$$\epsilon = \frac{N_{\text{trigger, hardware}}}{N_{\text{trigger, simulated}}} \tag{5.4}$$

The results of the study are listed in Table 5.1.

Trigger Type	**Efficiency**
Singles	99.6%
Pair	99.7%

Table 5.1: Trigger efficiency of both Singles and Pair triggers.

Chapter 6

Event Selection

Searching for a heavy photon resonance requires both the accurate reconstruction of the QED trident invariant mass spectrum and the efficient rejection of Bethe-Heitler events. With this in mind, a scheme was developed to select events with e^+e^- pairs whose kinematic signatures resemble that of QED tridents which, in turn, mirror the kinematics of heavy photon production and decay. Once a sample of QED tridents has been selected, additional kinematic requirements were applied to reject Bethe-Heitler events. The e^+e^- events which satisfied all criteria were used to produce the final invariant mass spectrum employed to search for a heavy photon resonance. The following chapter will discuss the selection used to arrive at the final event sample.

6.1 Data

Run Number	10%×Total Events	10%×Luminosity (nb^{-1})
5723	10,687,650	3.927
5724	11,397,637	4.229
5725	8,612,363	3.193
5739	8,093,200	2.956
5741	10,977,410	3.987
5742	11,174,619	4.224
5743	6,040,229	2.244
5766	9,927,829	3.337
5769	11,179,994	4.059
5771	11,642,768	4.254
5772	11,865,312	4.403
5773	13,429,284	5.014
5775	5,580,172	1.988
5776	8,121,968	2.997
5782	12,396,243	4.552
5783	12,226,626	4.548
5791	10,584,270	3.716
5795	8,789,774	3.174
5796	12,055,927	4.323
5797	10,047,503	3.584

Table 6.1: List of "golden" runs from the 2015 Heavy Photon Search Engineering Run used in this analysis along with the total number of events and luminosity of the unblinded portion of the data.

The data used for this analysis consist of the unblinded portion of the 2015 HPS engineering run. This amounts to 74.72 nb^{-1} (.4671 mC of charge) or 1/10 of a PAC day. For comparison, the projected limits shown in Figure 1.1 were set assuming a full PAC week (37.5 mC) of data. The list of runs used in this analysis

along with the unblinded number of events and luminosity for each run are shown in Table 6.1.

6.2 Event Selection

The HPS "pairs1" trigger was designed to trigger on events with two clusters whose positions in the Ecal were consistent with an e^+e^- from either a trident reaction or the decay of an A'. As such, only "pairs1" trigger events were considered for the final data sample. Furthermore, only events where the bias of the SVT was on, the SVT was positioned at 0.5 mm from the beam and where the events were free of data acquisition errors were included in the data sample.

6.2.1 Cluster Pair Selection

The acceptance of the HPS detector is optimized such that the e^+e^- pairs produced in either a QED trident reaction or from the decay of an A' are observed through their energy depositions in the Ecal. The energy depositions or clusters are expected to be in opposite Ecal volumes, i.e. top/bottom and coincident in time within a coincidence window of a few ns. This can be seen from Figure 6.1, which plots cluster time of one cluster composing a pair versus that of the other cluster. From the figure, it can be seen that most cluster pairs of interest are

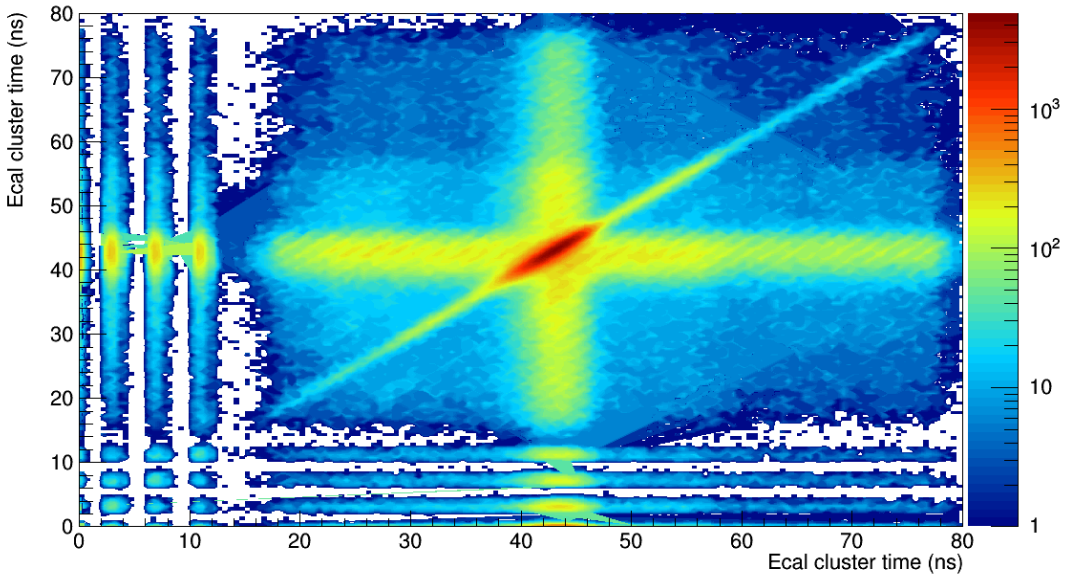

Figure 6.1: The spectrum of Ecal cluster times of one cluster composing a pair versus that of the other cluster. The figure clearly shows that most coincident pairs fall within tight coincidence and cluster time windows.

coincident to within a few ns. Furthermore, the majority of coincident clusters have a cluster time between 40 - 48 ns which corresponds approximately to the size of the trigger window (see Figure 6.2).

In order to select true coincidences, the clusters forming a pair were required to have a cluster time between 42 ns and 47.5 ns. Clusters outside of this window tend to be associated with pile-up in the calorimeter and fall outside of the 8 ns trigger window. As a result, the efficiency of finding a track associated with a cluster dramatically drops for clusters outside of this window. The selection is

shown graphically in red in Figure 6.2. Clusters satisfying the cluster time criteria are then formed into pairs. The difference between the cluster time of the pair is then required to fall within a 3.2 ns window around the coincidence peak located at 0.003 ns (Figure 6.3). If an event contains multiple "good" cluster pairs, the pair with the smallest difference in time is chosen.

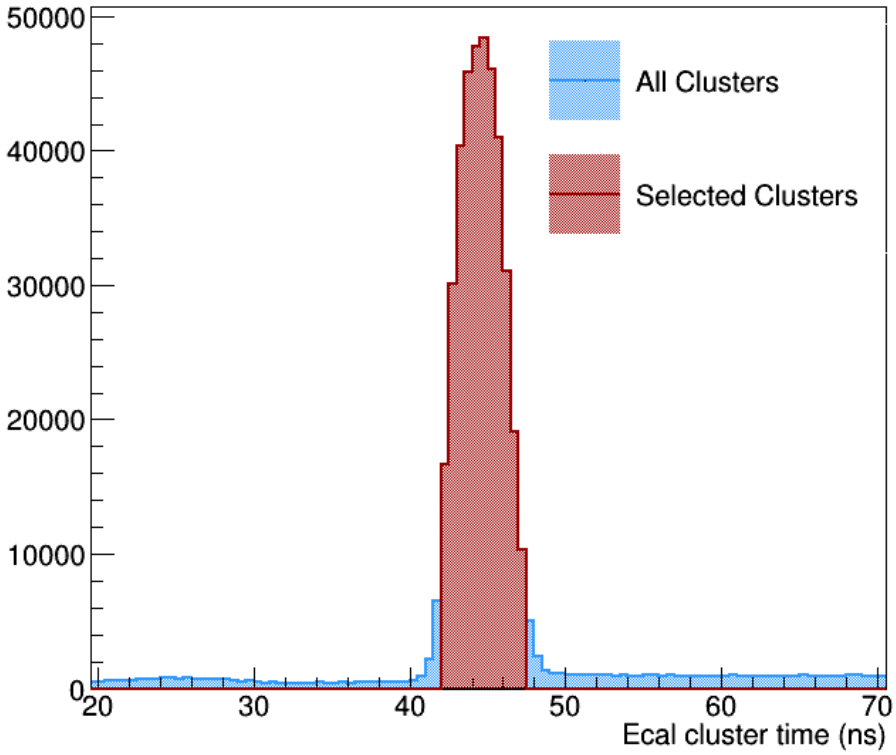

Figure 6.2: Cluster time of all Ecal clusters in an event (blue). The time of cluster is required to be between 42 ns and 47.5 ns (red) in order to ensure that it falls within the trigger window.

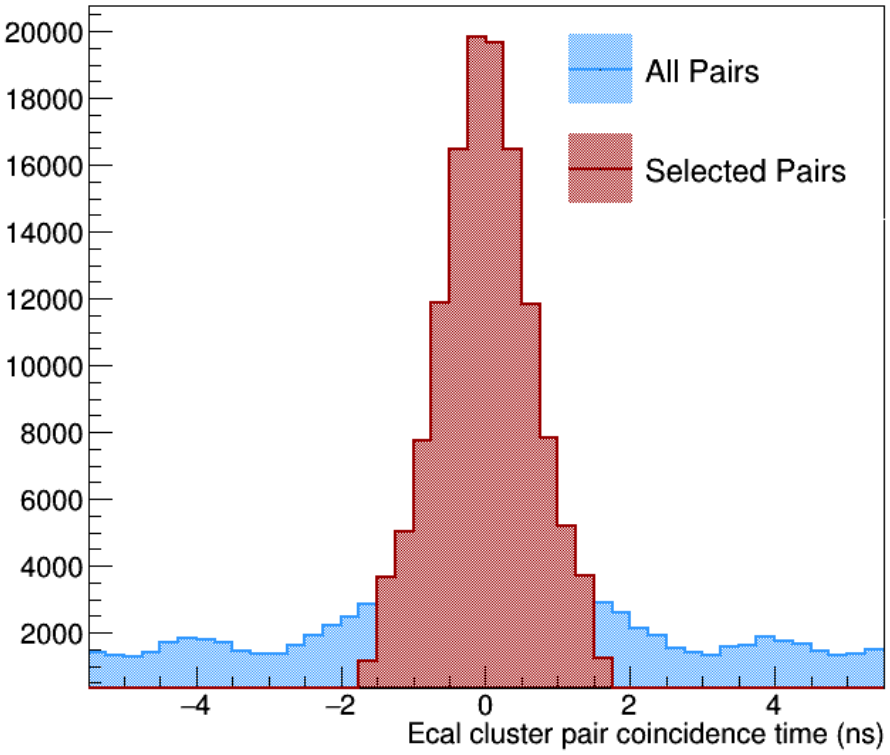

Figure 6.3: The difference in time of a cluster pair in an event. Pairs selected for the final event sample are required to have a difference in time that falls within a 3.2 ns window centered at 0.003 ns.

6.2.2 Track-Cluster Matching

In order to further suppress accidental coincident pairs where one or both clusters can be attributed to a photon, the selected "good" cluster pairs are required to have tracks associated with them. The trajectories of all tracks in an event are propagated downstream to the face of the Ecal using the full 3D magnetic field

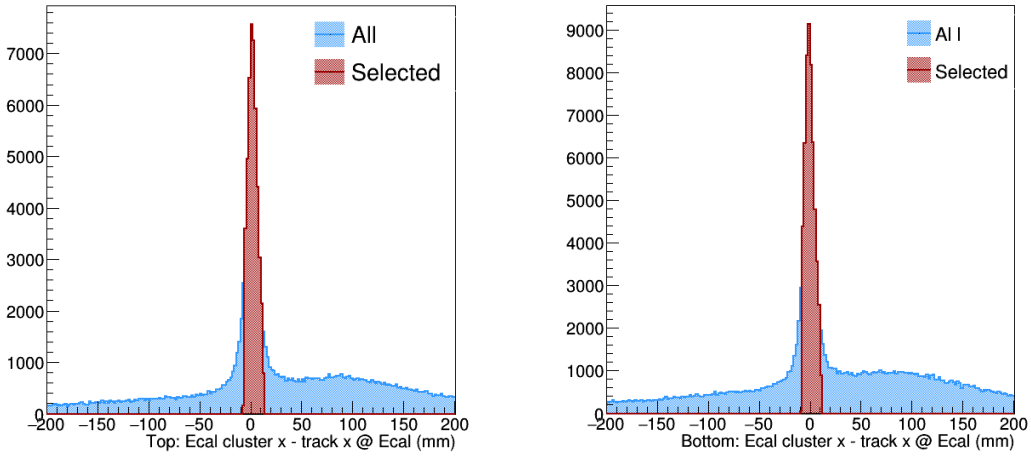

Figure 6.4: Difference between the x position of an Ecal cluster and the extrapolated track x at the Ecal for all tracks and clusters in an event (blue) separate by top (left) and bottom (right) detector volumes. True track-cluster matches appear as a peak above mismatches. In order for a track and cluster to be considered a match, the difference in x was required to fall within a 3σ window around the peak.

map. A track and a cluster are considered a match if the difference between their positions in both x and y satisfy the criteria listed in Table 6.2. The cuts were chosen such that they create a 3σ window around the peak of the cluster-track position difference distributions. The resulting selection is highlighted in red on Figure. 6.4 and 6.5. If multiple tracks were found to match to a single cluster,

	Cluster x - track x at Ecal (mm)	**Cluster y - track y at Ecal (mm)**
Top	$-6.10 \leq x \leq 12.93$	$-6.08 \leq y \leq 11.49$
Bottom	$-8.02 \leq x \leq 10.84$	$-8.31 \leq y \leq 7.40$

Table 6.2: Boundaries used to denote the 3σ window used to establish if an Ecal cluster and SVT track are matched to each other. Due to global misalignments, different windows are needed for top and bottom tracks and clusters.

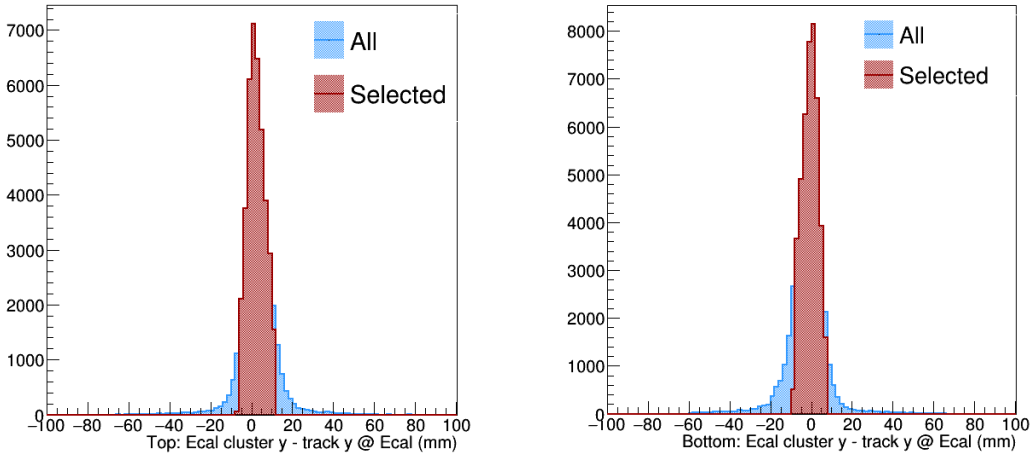

Figure 6.5: Difference between the y position of an Ecal cluster and the extrapolated track y at the Ecal for all tracks and clusters in an event (blue) separate by top (left) and bottom (right) detector volumes. True track-cluster matches appear as a peak above mismatches. In order for a track and cluster to be considered a match, the difference in y was required to fall within a 3σ window around the peak.

the track with the minimum radial distance to the cluster was chosen.

6.2.3 Final Trident Sample

The event selection criteria that have been applied thus far only select events that have QED trident or A'-like signatures, i.e. two coincident clusters that passed the trigger cuts and have e^+e^- tracks associated with them. However, there remain e^+e^- accidental coincidences that need to be removed from the final event sample. This is best accomplished by subjecting the tracks associated with the clusters to the following additional criteria:

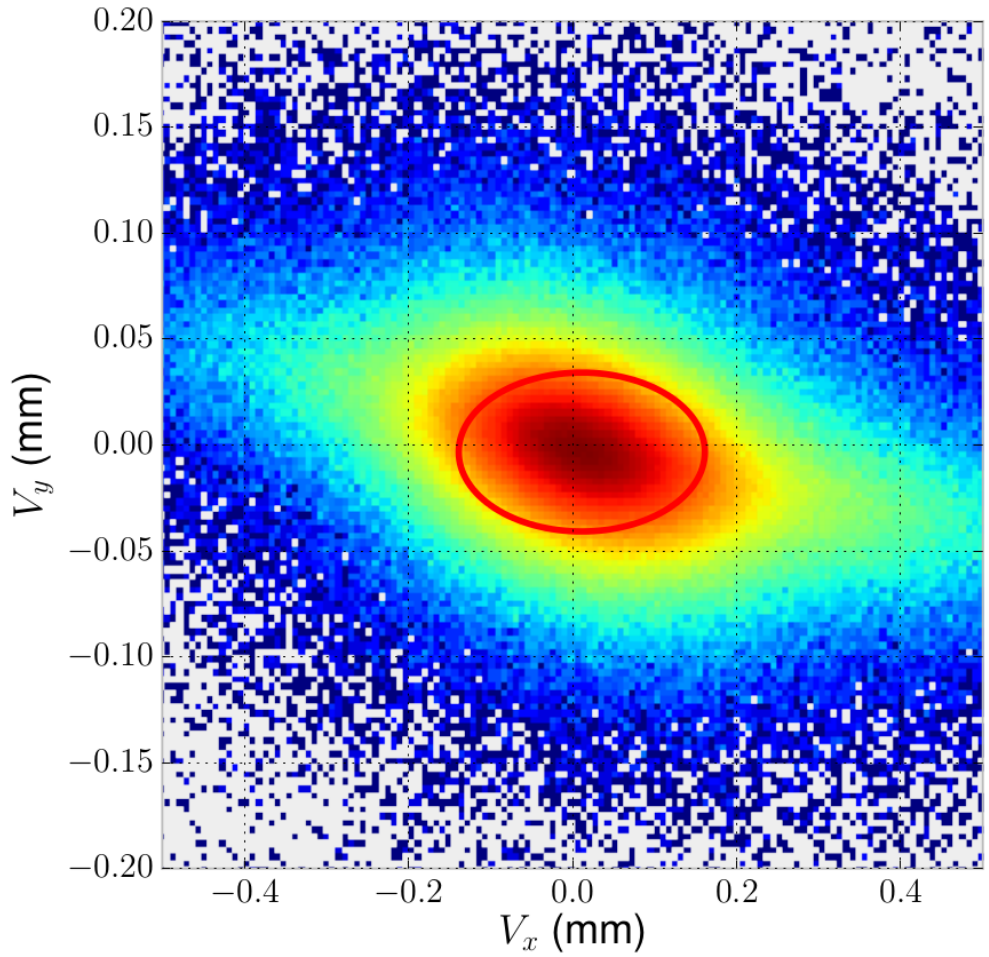

Figure 6.6: Vertex position at the target of all e^+e^- track pairs. The elliptical selection (in red) is used to select pairs for the final event sample.

- For simplicity, events that have multiple positron tracks are not considered.

- In order to cut down on the number of misconstructed tracks that may have been mismatched to a cluster, both tracks are subjected to χ^2 probability cut of 95%.

- Some electrons in the cluster pair may actually be a multiple Coulomb scattered beam electron of energy 1.056 GeV instead of one associated with a true e^+e^- pair. To remove these events from the final event sample, the momentum of each electron track is required to be less than 0.85 GeV.

- The e^+e^- tracks associated with the clusters are vertexed with their position along the beamline, v_z, constrained to the target. For true e^+e^- pairs, the vertex position in x and y (v_x and v_y) should be well constrained to an ellipse with dimensionality close to the beam spot. With this in mind, the fitted vertex χ^2 is first required to be less than 10. The positions along x and y are then required to lie within an ellipse defined as

$$\left(\frac{v_x - 0.0113}{0.15}\right)^2 + \left(\frac{v_y + 0.0033}{0.05}\right)^2 \leq 1.$$

  The elliptical selection is shown graphically in Figure 6.6.

6.2.4 Radiative Selection

As discussed in Section 3.2, the kinematic similarities between heavy photons and radiative processes can be used to analyze both the rate of A' signal production and the sensitivity of the experiment to A' signals. It is then crucial to

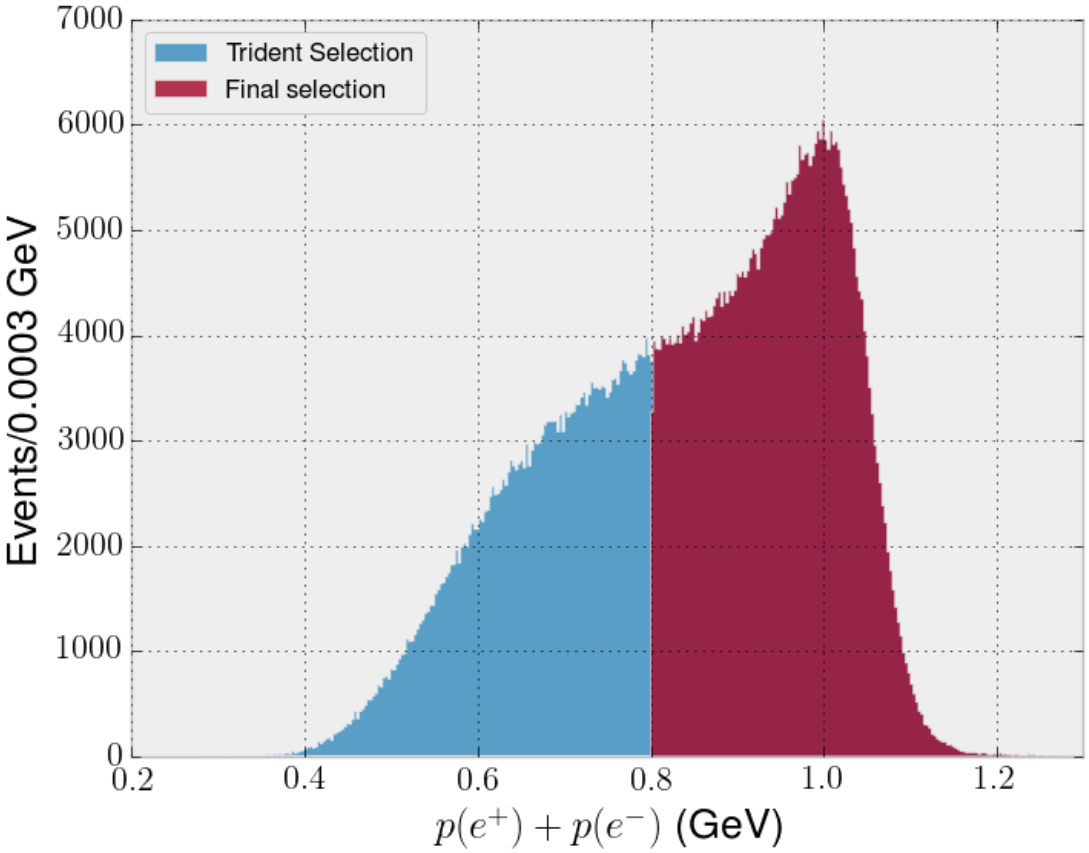

Figure 6.7: Distribution of the sum of e^+e^- momenta. The distribution in red graphically indicates the selection used to reduce the number of Bethe-Heitler from the final event sample.

maximize the fraction of radiative events in the final event sample. The final event sample is expected to be dominated by the Bethe-Heitler process. However, as discussed in Section 3.2, the kinematic difference between the radiative and Bethe-Heitler processes can be exploited to reduce the number of Bethe-Heitler events. Specifically, the e^+e^- pair produced in a radiative process will be highly boosted,

while only one of the electrons in the Bethe-Heitler process will be boosted while the other will be much softer. With this in mind, the sum of the momentum of the electron and positron, "p-sum," allows for the discrimination between the two processes. Specifically, radiative events are expected to have a "p-sum" peaked close to the beam energy (1.056 GeV), while the distribution of Bethe-Heitlers will be peaked at low p-sum.

Figure 6.7 shows the distribution of the sum of the momenta (p-sum) of the e^+e^- tracks composing a pair. Reducing the dominant Bethe-Heitler background was accomplished by requiring the p-sum of the e^+e^- tracks be greater than 0.8 GeV. The cut is shown graphically in Figure 6.7.

The invariant mass distribution before (blue) and after (red) the p-sum cut was applied is shown in Figure 6.8. The invariant mass distribution in red will serve as the starting point for the resonance search. The details of the resonance search will be given in Chapter 7.

6.2.5 Event Selection Efficiency

The cuts used to select the final invariant mass distribution along with their selection efficiency for data, trident Monte Carlo (MC), pure radiative Monte Carlo and 50 MeV A' events are summarized in Table 6.3. The trident MC sample used

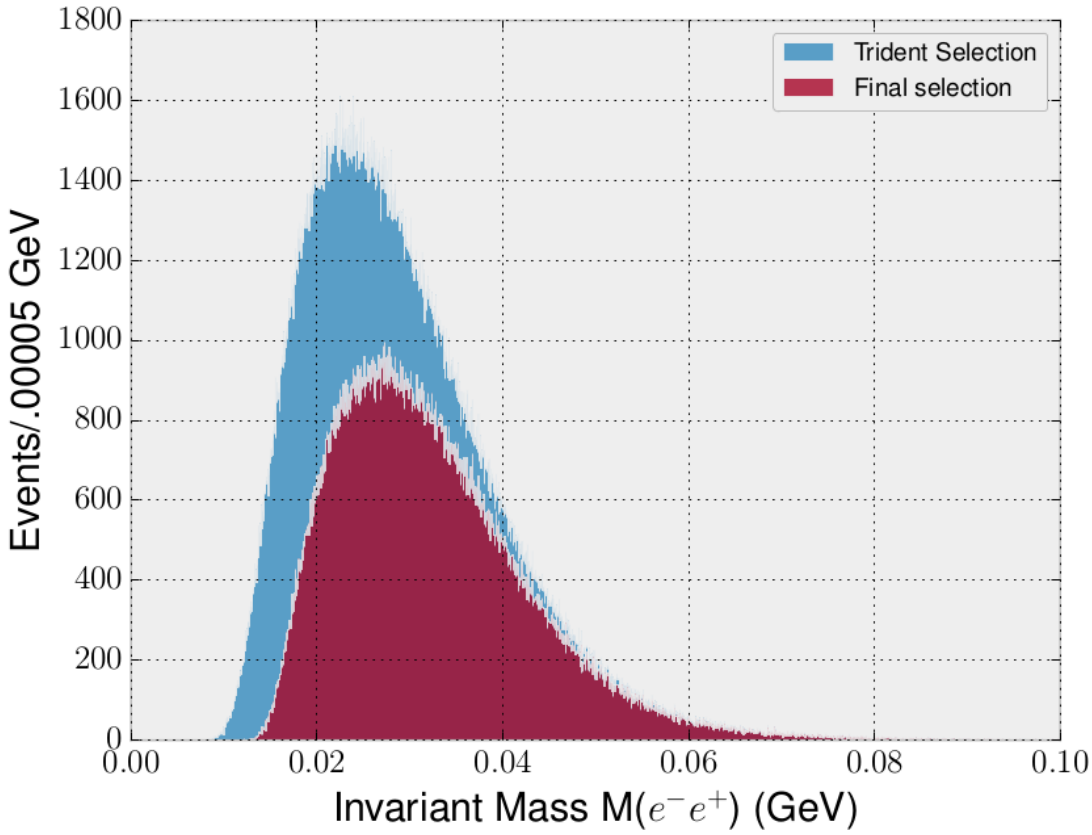

Figure 6.8: The Heavy Photon Search e^+e^- invariant mass distribution before (blue) and after (red) a cut on the sum of the e^+e^- momenta. The mass distribution in red will serve as the starting point for the resonance search.

contains both Bethe-Heitler and radiative events.

Description of Cuts	**Data**		**Trident MC**	**Radiative MC**	**50 MeV A' MC**
	N_{events}	ε (%)	ε (%)	ε (%)	ε (%)
Pair 1 Trigger Count	162825923	-	-	-	-
Single positron	12705660	7.80	75.05	70.73	85.90
Good cluster pair	4529997	2.78	51.10	54.60	73.74
Track-cluster match	1735394	1.07	21.11	27.19	55.49
Track $\chi^2 < 15$	1236300	0.76	17.33	21.66	32.52
e^- momentum < 0.85 GeV	1194117	0.73	17.31	21.63	32.48
Vertex $\chi^2 < 10$ and elliptical	710558	0.44	13.36	15.86	23.67
e^+e^- momentum sum > 0.8 GeV	437766	0.27	5.21	11.91	22.41

Table 6.3: Table showing the efficiency of each cut for data, a sample of trident MC, pure radiatives and 50 MeV A' events. The trident sample contains both Bethe-Heitler and radiative events.

Chapter 7

Resonance Search and Results

The following chapter will discuss the details and results of a resonance search for an A' in the mass range between 20 MeV/c^2 to 60 MeV/c^2. This includes a discussion of the procedure used to determine if a significant resonance was observed at a given A' mass hypothesis and the statistical formalism used to set an upper limit on both the signal and A' coupling strength.

This analysis makes use of the unblinded portion of the 2015 HPS engineering run data which amounts to a luminosity of 74 nb^{-1} (.4671 mC of charge) or 1/10 of a PAC day. A blind search for a resonance using the procedure outlined in this chapter and making use of the full 2015 engineering run dataset (1165.71 nb^{-1}, 7.2875 mC) is expected to be completed in the Summer of 2016.

7.1 Searching for a Resonance

If a heavy photon does indeed exist and has a mass that is within the acceptance of the HPS detector, it will appear as a resonance above the copious QED trident invariant mass distribution. Such a signal is expected to be Gaussian in nature, with a mean equal to the mass $m_{A'}$ of the A' and with a mass dependent width, $\sigma_{m_{A'}}$, given by the mass resolution parameterization define in Section 5.1.6. With this in mind, the invariant mass distribution measured by HPS (see Chapter 6 and Figure 6.8) will serve as the starting point for this analysis.

7.1.1 Maximum Likelihood Fit

Since the mass of the A' is unknown a priori, the e^+e^- invariant mass spectrum needs to be scanned for any significant peaks. Customarily, a search for a resonance is performed within a window constructed around the mass hypothesis of interest. Within the window, the distribution of A' signal events is modeled using the probability distribution function

$$P(m_{e^+e^-}) = \mu \cdot \phi(m_{e^+e^-}|m_{A'}, \sigma_{m_{A'}}) + B \cdot p(m_{e^+e^-}|\mathbf{t}) \tag{7.1}$$

where $m_{e^+e^-}$ is the e^+e^- invariant mass, μ is the signal yield, B is the number of background events within the window, $\phi(m_{e^+e^-}|m_{A'}, \sigma_{m_{A'}})$ is a Gaussian probability distribution describing the signal and $p(m_{e^+e^-}|\mathbf{t})$ is a Chebyshev polynomial of the first kind with coefficients $\mathbf{t} = (t_1, ...t_j)$ that is used to describe the background shape. In this instance, a 7th order Chebyshev polynomial is used to describe the background (see Section 7.2.3). Furthermore, $m_{A'}$ and $\sigma_{m_{A'}}$ are constant and set to the A' mass hypothesis and expected experimental mass resolution, respectively. Estimating the signal yield as well the background normalization and shape within a window can be done by the method of maximum likelihood. The theoretical formalism used to do this will be outlined here but a detailed discussion can be found in [83].

Assume the events within the window are binned as $\mathbf{n} = (n_1, ...n_i)$. Furthermore, assume the center of the ith bin is given by b_i and has a width equal to ϵ. The expected number of events of the ith bin is given by

$$E[n_i] = S_i + B_i \tag{7.2}$$

where

$$S_i = \mu \int_{b_i-\epsilon/2}^{b_i+\epsilon/2} \phi(m_{e^+e^-}|m_{A'}, \sigma_{m_{A'}}) d(m_{e^+e^-}) \tag{7.3}$$

$$B_i = B \int_{b_i-\epsilon/2}^{b_i+\epsilon/2} p(m_{e^+e^-}|t_j) d(m_{e^+e^-}). \tag{7.4}$$

Denoting the parameters that are not of immediate interest, i.e. the nuisance parameters, by $\theta = (B, \mathbf{t})$, an estimate of μ and θ can be obtained by finding the parameters $\hat{\mu}$ and $\hat{\theta}$ that maximize the Poisson likelihood function, $\mathcal{L}$

$$\mathcal{L}(\mu, \theta) = \prod_{k=1}^{n_{\text{bins}}} \frac{(S_k + B_k)^{n_k}}{n_k!} e^{-(S_k+B_k)} \tag{7.5}$$

where the sum is over all bins within the window, n_{bins}. In the case where the invariant mass is scanned for a resonance, the Poisson likelihood function is maximized within the window constructed around each A' mass hypothesis. This yields estimators for the signal yield and nuisance parameters at each A' mass hypothesis which are used to determine if a significant resonance was found.

7.1.2 Likelihood Ratio

When searching for a resonance above a background distribution, it is necessary to discriminate between two scenarios:

- The background only or null hypothesis, $H_0 : \mu = 0$.
- The signal+background hypothesis or alternative, $H_1 : \mu > 0$.

Establishing whether the signal+background model is significantly different from the background only model is typically done using the profile likelihood ratio

$$\lambda(\mu) = \frac{\mathcal{L}(\mu, \hat{\hat{\theta}})}{\mathcal{L}(\hat{\mu}, \hat{\theta})} \tag{7.6}$$

where $\hat{\hat{\theta}}$ is the conditional estimator for the nuisance parameters obtained by maximizing the Poisson likelihood assuming that the null or background only hypothesis is true i.e. $\mu = 0$. The unconditional estimators $\hat{\mu}$ and $\hat{\theta}$ are obtained by maximizing the Poisson likelihood without any constraints on μ. As can be seen from 7.6, if the estimator of the signal yield, $\hat{\mu}$, is compatible (incompatible) with the hypothesized μ, the likelihood ratio will tend to 1 (0).

A more convenient test statistic is the log likelihood ratio defined as

$$q_0 = \begin{cases} -2 \ln \frac{\mathcal{L}(0,\hat{\hat{\theta}})}{\mathcal{L}(\hat{\mu},\hat{\theta})} & \hat{\mu} > 0 \\ 0 & \hat{\mu} < 0. \end{cases} \tag{7.7}$$

In the large sample limit, the test statistic q_0 can be shown to follow a $1/2\chi^2$ distribution defined in [83] as

$$f(q_0|0) = \frac{1}{2}\left(\delta(q_0) + \frac{1}{\sqrt{2\pi}}\frac{1}{\sqrt{q_0}}e^{-q_0/2}\right) \tag{7.8}$$

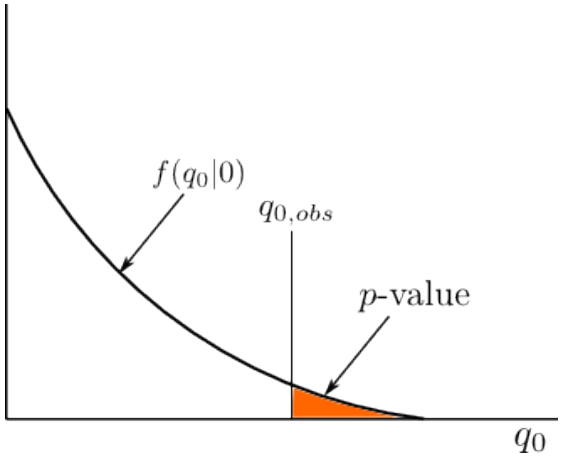

Figure 7.1: Graphical representation of a p-value.

where the first term on the right side of the equation is a delta function at 0 and the second term is a χ^2 distribution with one degree of freedom.

Quantifying how extreme the observation is can be done by calculating a p-value as

$$p = \int_{q_{0,obs}}^{\infty} f(q_0|0)dq_0. \tag{7.9}$$

This is shown graphically in Figure 7.1. Typically, the observed p-value is compared against a significance level α. The significance level denotes the probability of incorrectly rejecting the null hypothesis in favor of the alternative (type-I error). In other words, it denotes the probability of there being a statistical fluctuation in the background large enough to mimic a signal. If a p-value is found to be less than α, the measurement is claimed to be significant. Typically, in particle

physics, an α on the order of 3×10^{-7} (5σ) is required to claim discovery of new phenomena. This means that there is a 1 in about 3.5 million chance that the observation is due to a fluctuation in the background.

7.1.3 The Look-Elsewhere Effect

As discussed previously in Section 7.1.2, a result is determined significant if the p-value is smaller than some pre-determined threshold, α. However, when performing multiple tests, as is the case when scanning a mass distribution for a resonance, an observation with a p-value that is as extreme as α is bound to occur at a rate of $n \times \alpha$ where n is the number of measurements. This phenomenon is known as the "Look-Elsewhere Effect" (LEE) and needs to be taken into account through a correction to the "local" p-value observed at each mass hypothesis.

Assuming that only a single heavy photon can be observed within the HPS invariant mass distribution, the correction can be estimated using a large number of pseudo-data sets and generating the distribution $f(q_{0,max}|0)$ composed of the largest q_0 (i.e. smallest p-value) from each of the invariant mass scans. However, generating a distribution of $f(q_{0,max}|0)$ that would allow an estimation of a "global" p-value (i.e. local p-value after correction) down to the level of 5σ with any accuracy would require running $> 10^6$ pseudo experiments. Generating so

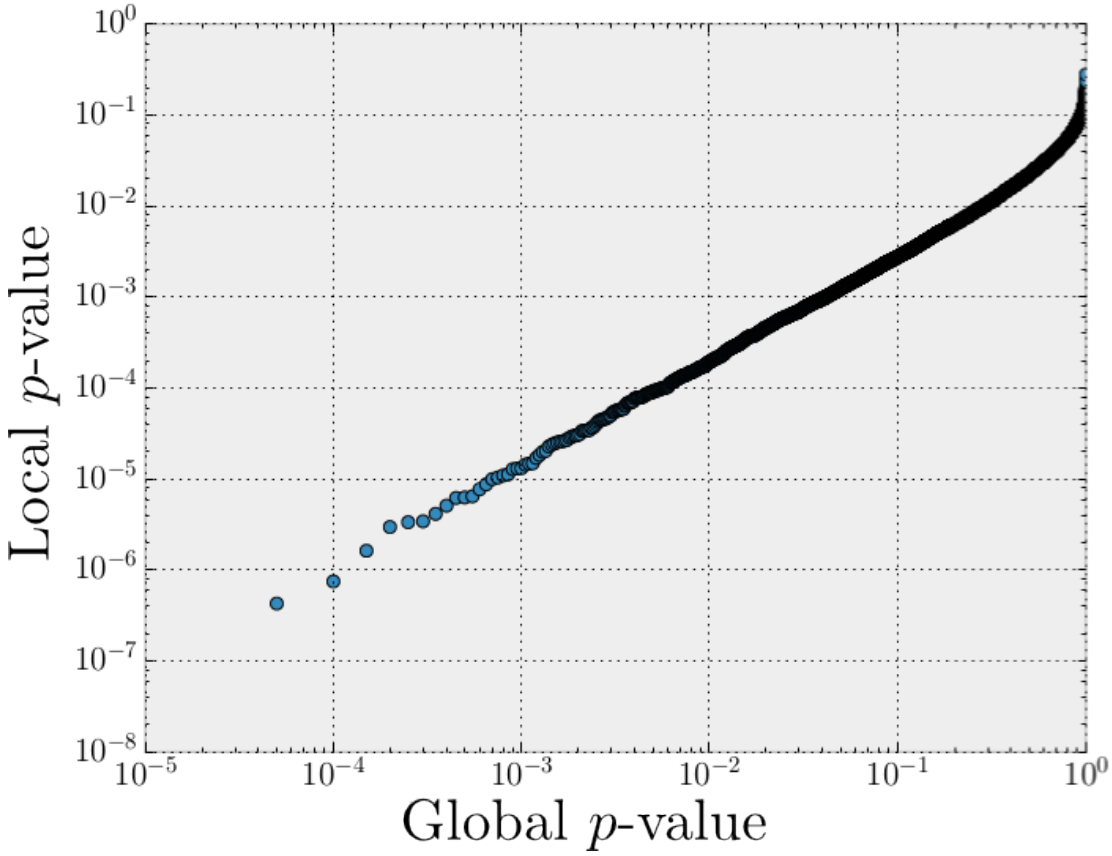

Figure 7.2: Mapping between local and global p-values.

many pseudo-data sets is often not feasible within a reasonable amount of time.

Instead, the smallest p-values obtained from a series of resonance searches on 10,000 pseudo data sets were ranked and the corresponding quantile was calculated [84]. A mapping from a local p-value to a global p-value is then created. The mapping created for this analysis is shown in Figure 7.2. As can be seen from the figure, a local p-value equal to 0.05 corresponds to a global p-value of ~ 0.5.

7.2 Fit Parameters

Prior to performing the resonance search on real data, several fit parameters were optimized using pseudo data sets based on Monte Carlo. These included the size of the fit window, the binning of the invariant mass distribution and the order of the polynomial used to describe the background. All parameters were chosen such that signal yield pull

$$\text{pull} = \frac{\mu_{\text{fit}} - \mu_{\text{inserted}}}{\mu_{\text{fit error}}} \tag{7.10}$$

was minimized for all fits performed across an invariant mass spectrum.

7.2.1 Pseudo Data Sets

Pseudo data sets are needed to understand fitting systematics and to optimize the fit function, window size and mass binning. In order to obtain an invariant mass probability density function (PDF) that describes the data, smoothing algorithm 353 QH [85] was applied to the unit normalized final invariant mass MC distribution. The resulting PDF after smoothing (blue line) overlaid on top of the MC distribution it was generated from is shown in Figure 7.3.

Pseudo data sets were then generated by sampling the PDF between 0 and

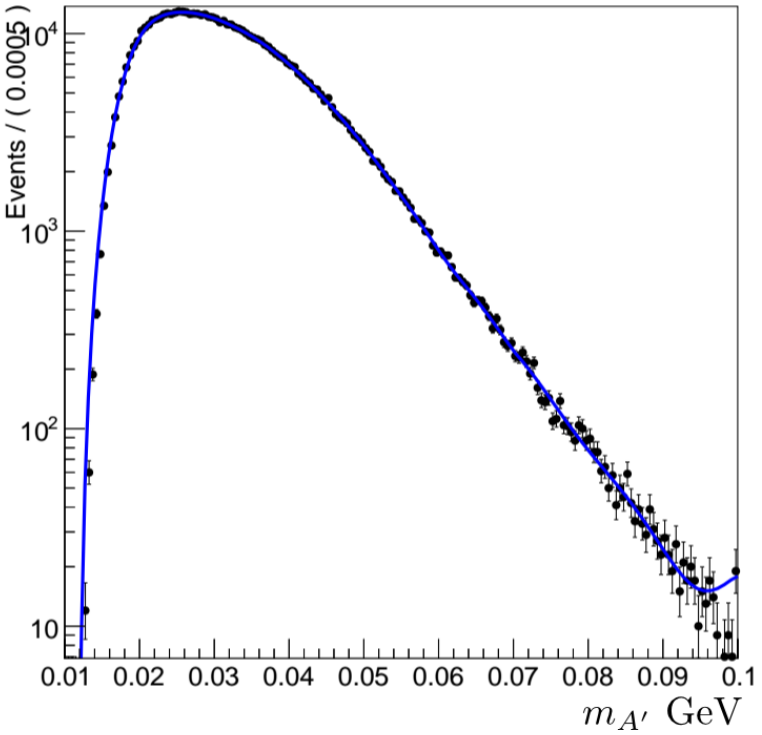

Figure 7.3: Probability density function obtained by applying a smoothing algorithm to the Heavy Photon Search Monte Carlo invariant mass distribution.

100 MeV with the total number of events, 437,766, chosen to match the number observed in data. The resulting pseudo data is binned to match the data distributions with the expectation value of each bin Poisson distributed.

7.2.2 Mass Binning

Ideally, an unbinned maximum likelihood fit would be used to estimate the fit parameters describe previously. However, due to the large number of statistics, this wouldn't be possible to do in a reasonable amount of time. Instead, a binned

likelihood fit is performed with the bin size set such that the pulls are minimized.

In order to understand the effect of the bin size on the fitting systematics, pseudo data sets were binned using bin sizes of 0.2 MeV, 0.1 MeV and 0.05 MeV. A resonance search was performed on each of the pseudo data sets and pull distributions were generated at each mass hypothesis. Using this procedure, it was found that using a bin size of 0.05 MeV minimizes the pulls, hence, it was used in the final analysis.

7.2.3 Fit Window and Polynomial Order

The pseudo data sets were also used to understand what size fit window and what order polynomial minimizes the signal yield pulls. Performing a resonance search on each of the pseudo data sets using windows of size $n \times \sigma_{m_{A'}(m_{e^+e^-})}$ where n is a scale factor, it was found that $n = 15$ minimizes the pulls across the whole range. Furthermore, it was found that the maximum window size that could be used is 20 MeV after which the pulls would become worse. A similar procedure was used to determine the polynomial used to model the background. It was found that a 7th order polynomial minimizes the pulls.

7.3 Results

The resulting local p-values from a resonance search conducted in the range between 20 MeV and 60 MeV are shown in Figure 7.4. The most significant signal was found at a mass of 27.525 MeV and has a local p-value of 4×10^{-3}. The resulting signal plus background fit (blue) along with the signal component (red) and background component (green) is shown in Figure 7.5. After correcting for the LEE, the corresponding global p-value is $\sim 10\%$.

7.4 Setting Upper Limits on the Signal Yield

Since no significant resonances were found, a 90% confidence upper limit on the number of signal events at each mass hypothesis was set. For the purpose of setting an upper limit, the likelihood ratio is inverted. The statistic used to set an upper limit is then

$$q_\mu = \begin{cases} -2\ln\frac{\mathcal{L}(\mu,\hat{\hat{\theta}})}{\mathcal{L}(0,\hat{\hat{\theta}})} & \hat{\mu} < 0 \\ -2\ln\frac{\mathcal{L}(\mu,\hat{\hat{\theta}})}{\mathcal{L}(\hat{\mu},\hat{\theta})} & 0 \leq \hat{\mu} \leq \mu \\ 0 & \hat{\mu} > \mu \end{cases} \tag{7.11}$$

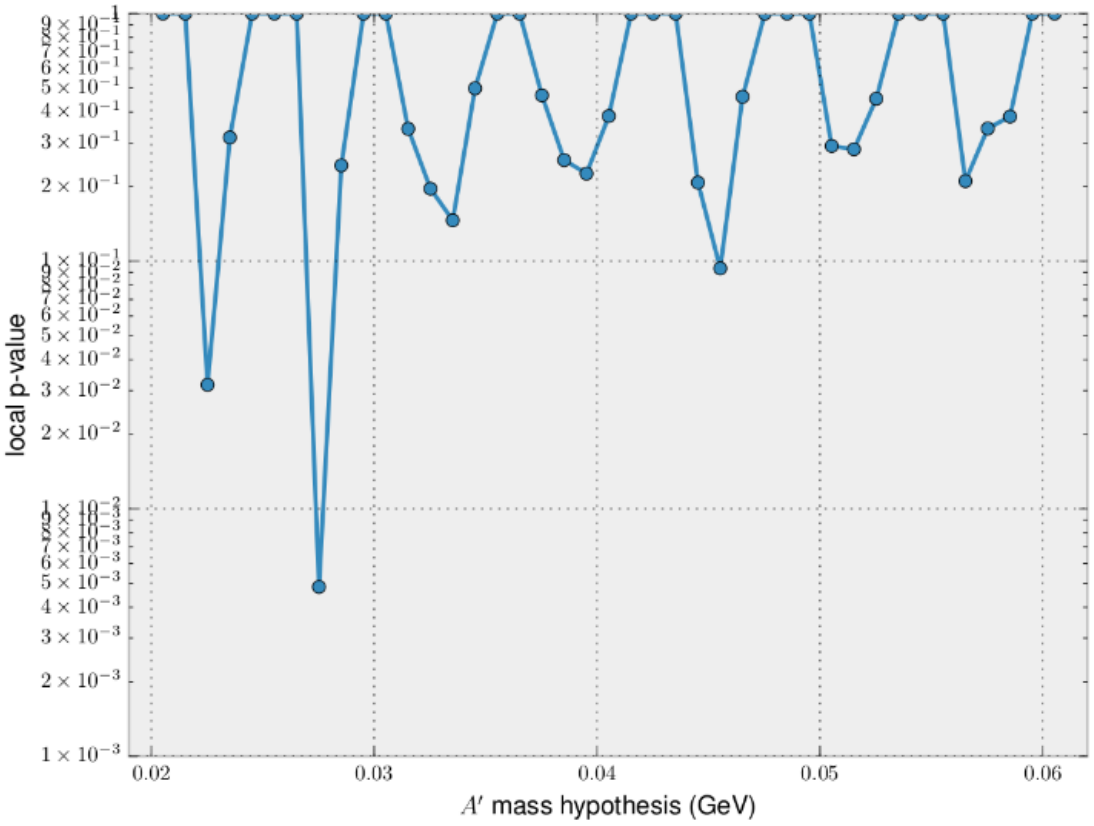

Figure 7.4: Resulting p-values from a resonance search for an A' across the invariant mass spectrum.

with the corresponding p-value being given by

$$p = \int_{q_{\mu,obs}}^{\infty} f(q_\mu|\mu) dq_\mu \tag{7.12}$$

where $f(q_\mu|\mu)$ is the probability distribution of q_μ given the hypothesized value of μ. In order to find the upper limit, μ_{up}, the test above is carried out over a range of signal yields until a p-value of 0.1 (90% confidence) is found. The signal yield

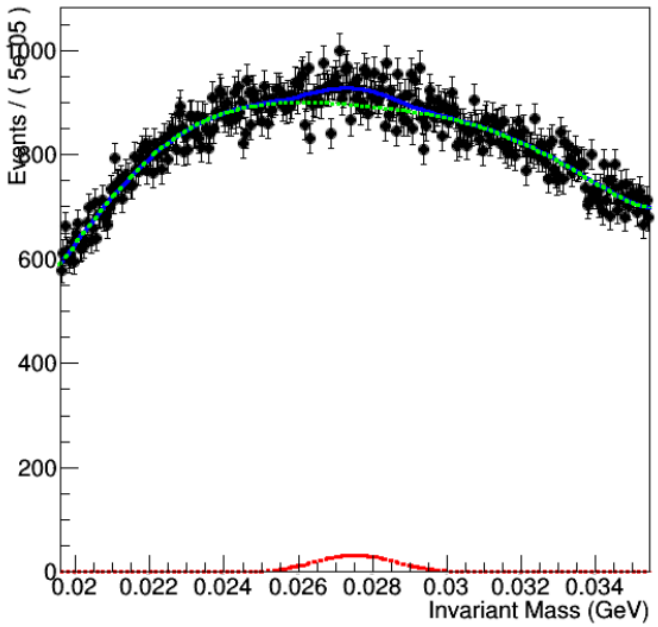

Figure 7.5: Resulting signal plus background fit (blue) assuming an A' mass hypothesis of 27.525 MeV. The signal component is shown in red while the background component is shown in green.

value that corresponds to a p-value of 0.1 is μ_{up} and is often referred to as the unconstrained limit. The resulting unconstrained upper limits are shown in blue in Figure 7.6.

As shown in green in Figure 7.6, it is often the case that the estimator for the signal yield, at a given mass hypothesis, is zero or even negative. In such cases, the probability distribution function of the test statistic q_μ assuming μ_{up} will nearly coincide with the distribution of q_μ assuming $\mu = 0$, i.e. the background only hypothesis. As a result, there is a lack of sensitivity to a signal measurement at those mass hypotheses.

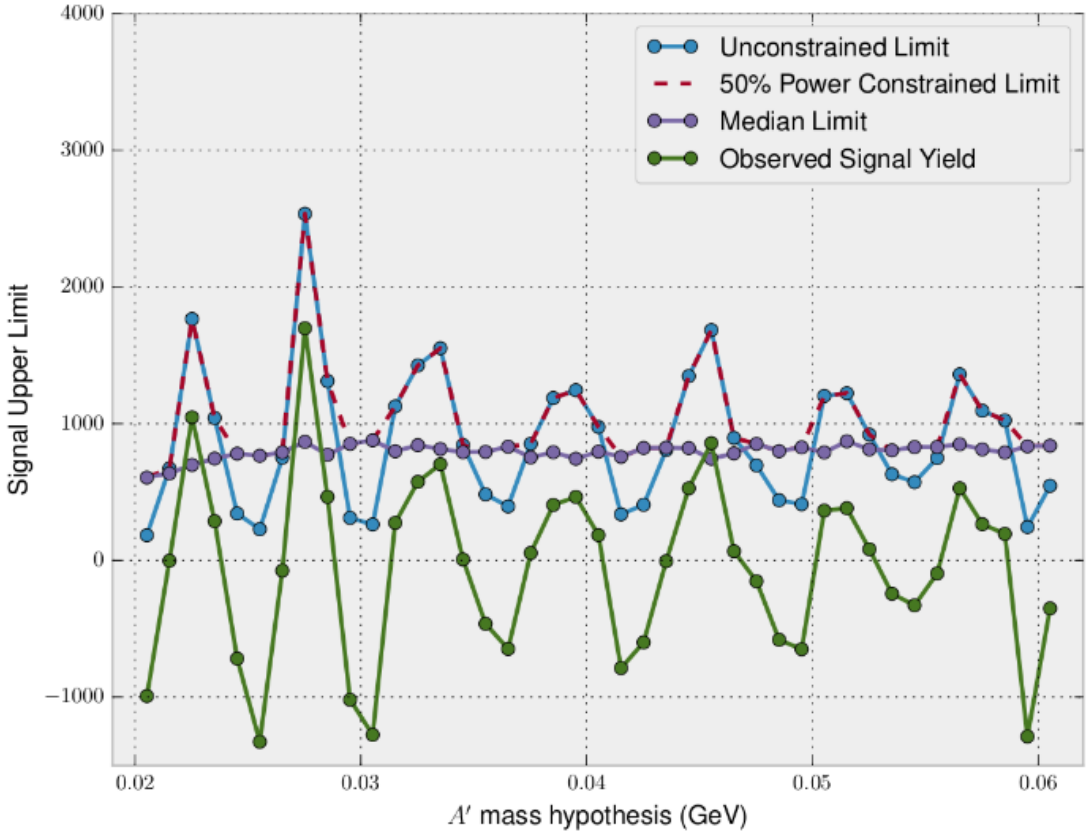

Figure 7.6: Upper limits on the signal yield at each mass hypothesis.

In such cases, a 50% power-constrained upper limit on the signal is set [86]. At each mass hypothesis, a distribution of signal upper limits is generated from background only pseudo-data sets and the median (50% quantile) upper limit is calculated, μ_{median}. The upper limit in that region is then set to the larger of either the unconstrained limit or the median limit

$$\mu_{pc} = \max(\mu_{\text{up}}, \mu_{\text{median}}). \tag{7.13}$$

The power constrained limits are shown in red in Figure 7.6.

7.5 Setting a limit on ϵ

As discussed in Chapter 3, the kinematic similarities between heavy photons and radiatives allows their cross sections to be related within a mass window, δm, near $m_{A'}$ as

$$\frac{d\sigma(e^- Z \to e^- A' Z(A' \to e^+ e^-))}{d\sigma(e^- Z \to e^- \gamma^* Z(\gamma^* \to e^+ e^-))} = \left(\frac{3\pi\epsilon^2}{2N_{eff}\alpha}\right)\left(\frac{m_{A'}}{\delta m_{A'}}\right) \tag{7.14}$$

where N_{eff} is the number of available decay channels available. For the A' masses considered in this analysis, $N_{eff} = 1$. Using Equation 7.14, the upper limit on the signal, S_{up}, can be related to an upper limit on the A' coupling strength as

$$\epsilon^2 = \left(\frac{S_{\text{up}}/m_{A'}}{f\Delta B/\Delta m}\right)\left(\frac{2N_{eff}\alpha}{3\pi}\right) \tag{7.15}$$

where $\Delta B/\Delta m$ is the number of background events per MeV and f is the ratio of the pure radiative cross-section to the full trident cross section. The ratio is calculated using MC and is shown in Figure 7.7 as a function of mass. In order to calculate the number of background events per MeV, a 1 MeV window is constructed around the A' mass hypothesis and the number of background events

in that window are counted. The resulting number of background events per MeV at each mass hypothesis are shown in Figure 7.8.

The limits on the coupling derived using Equation 7.15 are shown in Figure 7.9. Using the full data set the reach is expected to increase by a factor of 4 down to $\epsilon^2 \sim 10^{-6}$.

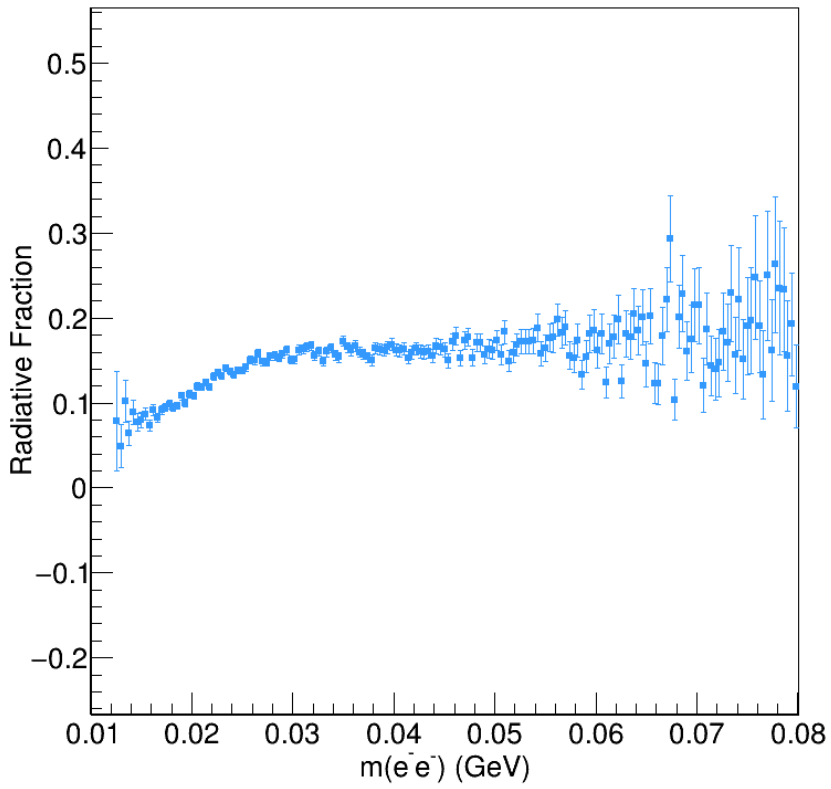

Figure 7.7: The ratio of the pure radiative cross-section to the full trident cross section as a function of mass.

7.6 Systematics

The upper limits on the coupling shown in Figure 7.9 have not been corrected for any theoretical or experimental uncertainties. These include uncertainties in the mass resolution ($\sim$10%), luminosity ($\sim$1%), theory cross-sections ($\sim$0.5%), electron and positron efficiency (>95%) and the background. All of these uncertainties will be included in the final result using the full 2015 engineering run dataset.

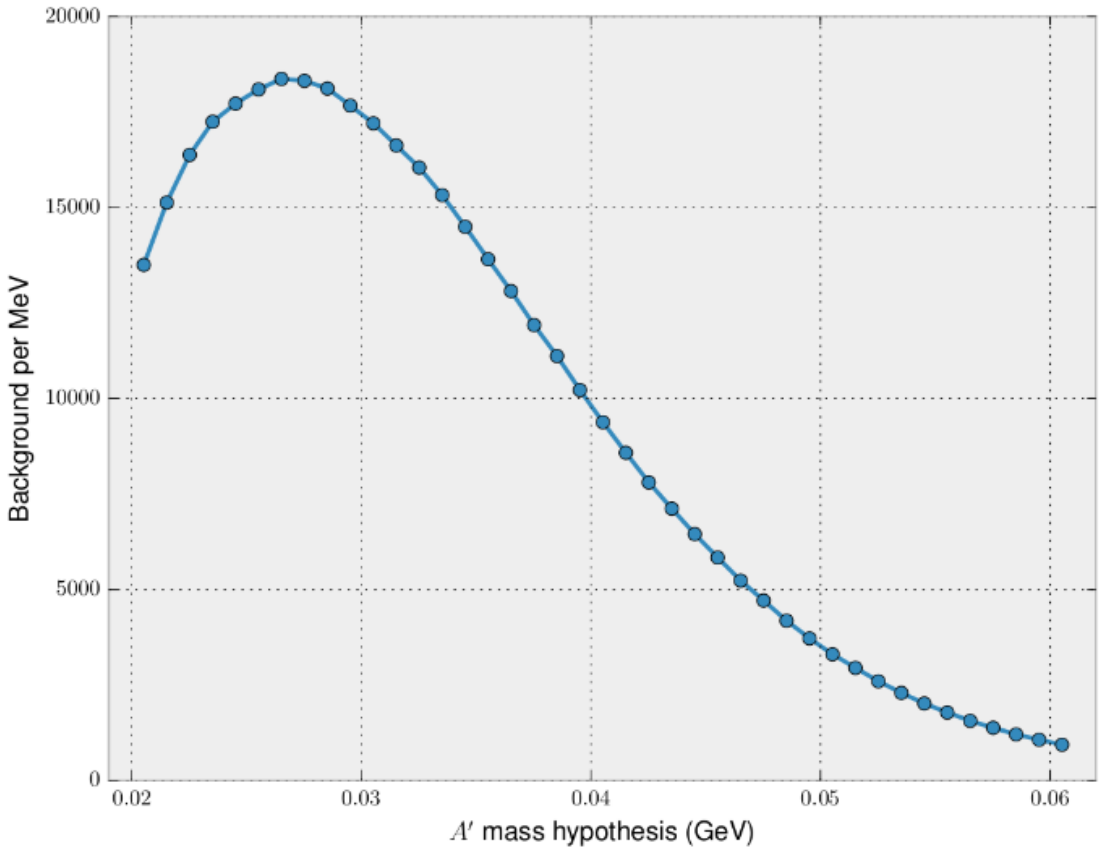

Figure 7.8: The number of background events in a 1 MeV window around each A' mass hypothesis.

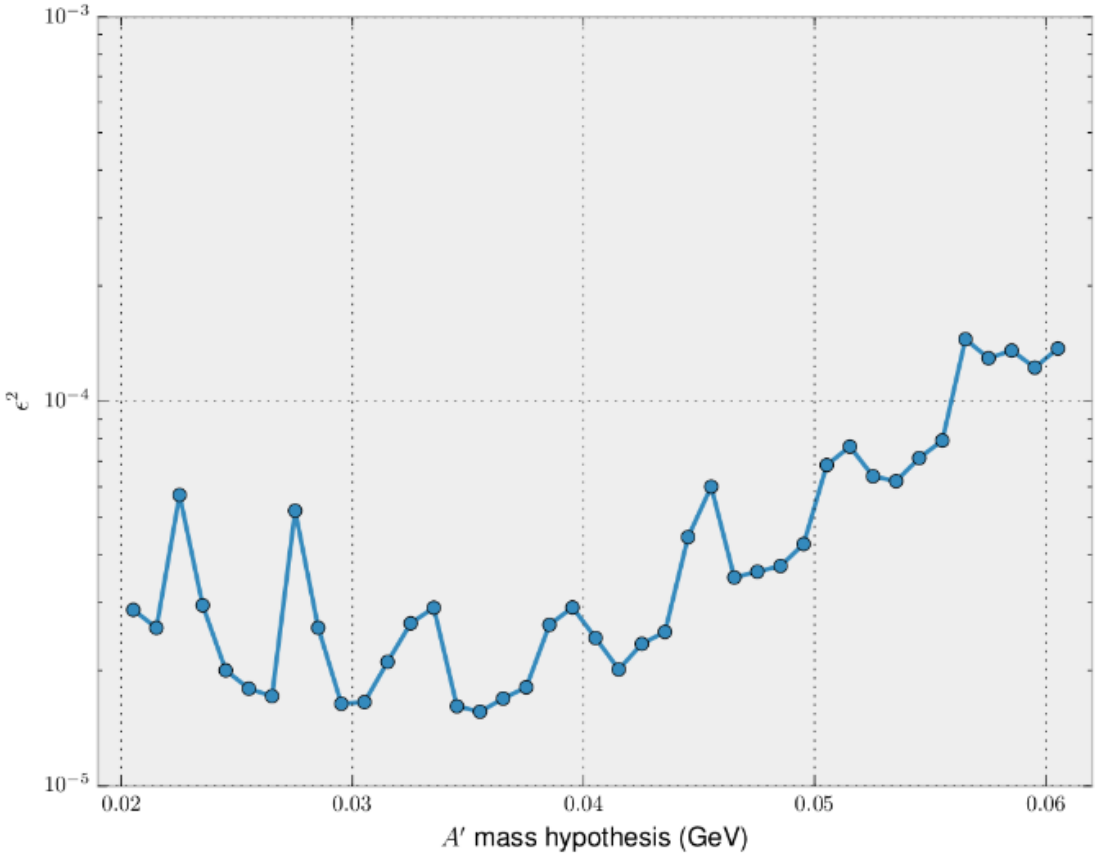

Figure 7.9: Upper limits on the coupling strength.

Chapter 8

Conclusion

A resonance search for an A' with a mass ranging between 20 MeV and 60 MeV and decaying to an e^+e^- pair was performed using the unblinded portion of the 2015 HPS engineering run dataset. A search for a peak above the trident QED invariant mass spectrum that would arise from the decay of the heavy photon was conducted and no significant excess was observed. Preliminary, 90% confidence level, upper limits on the square of the coupling were set at the level of $10^{-5} - 10^{-4}$. These upper limits do not take into account systematics which will be incorporated into the final analysis using the full engineering run dataset. A resonance search using the full engineering run dataset is expected to be completed over the summer. Using the full dataset, the reach is expected to increase by a factor of 4 down to $\epsilon^2 \sim 10^{-6}$.

Bibliography

[1] Georges Aad et al. Observation of a new particle in the search for the Standard Model Higgs boson with the ATLAS detector at the LHC. *Phys. Lett.*, B716:1–29, 2012, 1207.7214.

[2] Serguei Chatrchyan et al. Observation of a new boson at a mass of 125 GeV with the CMS experiment at the LHC. *Phys. Lett.*, B716:30–61, 2012, 1207.7235.

[3] F. Zwicky. Die Rotverschiebung von extragalaktischen Nebeln. *Helv. Phys. Acta*, 6:110–127, 1933.

[4] V. C. Rubin, N. Thonnard, and W. K. Ford, Jr. Rotational properties of 21 SC galaxies with a large range of luminosities and radii, from NGC 4605 /R = 4kpc/ to UGC 2885 /R = 122 kpc/. *Astrophys. J.*, 238:471, 1980.

[5] Douglas Clowe, Marusa Bradac, Anthony H. Gonzalez, Maxim Markevitch, Scott W. Randall, Christine Jones, and Dennis Zaritsky. A direct empirical proof of the existence of dark matter. *Astrophys. J.*, 648:L109–L113, 2006, astro-ph/0608407.

[6] R. Adam et al. Planck 2015 results. I. Overview of products and scientific results. 2015, 1502.01582.

[7] Oscar Adriani et al. An anomalous positron abundance in cosmic rays with energies 1.5-100 GeV. *Nature*, 458:607–609, 2009, 0810.4995.

[8] Nima Arkani-Hamed, Douglas P. Finkbeiner, Tracy R. Slatyer, and Neal Weiner. A Theory of Dark Matter. *Phys. Rev.*, D79:015014, 2009, 0810.0713.

[9] Maxim Pospelov and Adam Ritz. Astrophysical Signatures of Secluded Dark Matter. *Phys. Lett.*, B671:391–397, 2009, 0810.1502.

[10] Dan Hooper, Neal Weiner, and Wei Xue. Dark Forces and Light Dark Matter. *Phys. Rev.*, D86:056009, 2012, 1206.2929.

[11] Bob Holdom. Two U(1)'s and Epsilon Charge Shifts. *Phys. Lett.*, B166:196–198, 1986.

[12] J. D. Bjorken, S. Ecklund, W. R. Nelson, A. Abashian, C. Church, B. Lu, L. W. Mo, T. A. Nunamaker, and P. Rassmann. Search for Neutral Metastable Penetrating Particles Produced in the SLAC Beam Dump. *Phys. Rev.*, D38:3375, 1988.

[13] E. M. Riordan, M. W. Krasny, K. Lang, P. de Barbaro, A. Bodek, S. Dasu, N. Varelas, X. Wang, R. Arnold, D. Benton, P. Bosted, L. Clogher, A. Lung, S. Rock, Z. Szalata, B. W. Filippone, R. C. Walker, J. D. Bjorken, M. Crisler, A. Para, J. Lambert, B. Button-Shafer, J.and Debebe, M. Frodyma, R. S. Hicks, G. A. Peterson, and R. Gearhart. Search for short-lived axions in an electron-beam-dump experiment. *Phys. Rev. Lett.*, 59:755–758, 1987.

[14] A. Bross, M. Crisler, S. Pordes, J. Volk, S. Errede, and J. Wrbanek. Search for short-lived particles produced in an electron beam dump. *Phys. Rev. Lett.*, 67:2942–2945, 1991.

[15] A. Konaka, K. Imai, H. Kobayashi, A. Masaike, K. Miyake, T. Nakamura, N. Nagamine, N. Sasao, A. Enomoto, Y. Fukushima, E. Kikutani, H. Koiso, H. Matsumoto, K. Nakahara, S. Ohsawa, T. Taniguchi, I. Sato, and J. Urakawa. Search for neutral particles in electron-beam-dump experiment. *Phys. Rev. Lett.*, 57:659–662, 1986.

[16] M. Davier and H. Nguyen Ngoc. An Unambiguous Search for a Light Higgs Boson. *Phys. Lett.*, B229:150, 1989.

[17] James D. Bjorken, Rouven Essig, Philip Schuster, and Natalia Toro. New Fixed-Target Experiments to Search for Dark Gauge Forces. *Phys. Rev.*, D80:075018, 2009, 0906.0580.

[18] Sarah Andreas, Carsten Niebuhr, and Andreas Ringwald. New limits on hidden photons from past electron beam dumps. *Phys. Rev. D*, 86:095019, 2012.

[19] J. Blumlein et al. Limits on neutral light scalar and pseudoscalar particles in a proton beam dump experiment. *Z. Phys.*, C51:341–350, 1991.

[20] J. Blumlein et al. Limits on the mass of light (pseudo)scalar particles from Bethe-Heitler e+ e- and mu+ mu- pair production in a proton - iron beam dump experiment. *Int. J. Mod. Phys.*, A7:3835–3850, 1992.

[21] Matthew Reece and Lian-Tao Wang. Searching for the light dark gauge boson in GeV-scale experiments. *JHEP*, 07:051, 2009, 0904.1743.

[22] Bernard Aubert et al. Search for Dimuon Decays of a Light Scalar Boson in Radiative Transitions $\Upsilon \to \gamma A_0$. *Phys. Rev. Lett.*, 103:081803, 2009, 0905.4539.

[23] D. Babusci et al. Limit on the production of a light vector gauge boson in phi meson decays with the KLOE detector. *Phys. Lett.*, B720:111–115, 2013, 1210.3927.

[24] F. Archilli et al. Search for a vector gauge boson in ϕ meson decays with the KLOE detector. *Phys. Lett.*, B706:251–255, 2012, 1110.0411.

[25] S. Abrahamyan et al. Search for a New Gauge Boson in Electron-Nucleus Fixed-Target Scattering by the APEX Experiment. *Phys. Rev. Lett.*, 107:191804, 2011, 1108.2750.

[26] H. Merkel et al. Search at the Mainz Microtron for Light Massive Gauge Bosons Relevant for the Muon g-2 Anomaly. *Phys. Rev. Lett.*, 112(22):221802, 2014, 1404.5502.

[27] G. Agakishiev et al. Searching a Dark Photon with HADES. *Phys. Lett.*, B731:265–271, 2014, 1311.0216.

[28] J. R. Batley et al. Search for the dark photon in π^0 decays. *Phys. Lett.*, B746:178–185, 2015, 1504.00607.

[29] Maxim Pospelov. Secluded U(1) below the weak scale. *Phys. Rev.*, D80:095002, 2009, 0811.1030.

[30] G. W. Bennett et al. Final Report of the Muon E821 Anomalous Magnetic Moment Measurement at BNL. *Phys. Rev.*, D73:072003, 2006, hep-ex/0602035.

[31] Mark Goodsell and Andreas Ringwald. Light Hidden-Sector U(1)s in String Compactifications. *Fortsch. Phys.*, 58:716–720, 2010, 1002.1840.

[32] S. A. Abel, M. D. Goodsell, J. Jaeckel, V. V. Khoze, and A. Ringwald. Kinetic Mixing of the Photon with Hidden U(1)s in String Phenomenology. *JHEP*, 07:124, 2008, 0803.1449.

[33] P. Candelas, Gary T. Horowitz, Andrew Strominger, and Edward Witten. Vacuum Configurations for Superstrings. *Nucl. Phys.*, B258:46–74, 1985.

[34] S. Andreas, M. D. Goodsell, and A. Ringwald. Dark matter and dark forces from a supersymmetric hidden sector. *Phys. Rev.*, D87(2):025007, 2013, 1109.2869.

[35] Joerg Jaeckel and Andreas Ringwald. The Low-Energy Frontier of Particle Physics. *Ann. Rev. Nucl. Part. Sci.*, 60:405–437, 2010, 1002.0329.

[36] Clifford Cheung, Joshua T. Ruderman, Lian-Tao Wang, and Itay Yavin. Kinetic mixing as the origin of a light dark-gauge-group scale. *Phys. Rev. D*, 80:035008, 2009, hep-ph/09023246.

[37] Nima Arkani-Hamed and Neal Weiner. LHC Signals for a SuperUnified Theory of Dark Matter. *JHEP*, 12:104, 2008, 0810.0714.

[38] Mark Goodsell, Joerg Jaeckel, Javier Redondo, and Andreas Ringwald. Naturally Light Hidden Photons in LARGE Volume String Compactifications. *JHEP*, 11:027, 2009, 0909.0515.

[39] Michele Cicoli, Mark Goodsell, Joerg Jaeckel, and Andreas Ringwald. Testing String Vacua in the Lab: From a Hidden CMB to Dark Forces in Flux Compactifications. *JHEP*, 07:114, 2011, 1103.3705.

[40] M. Ackermann et al. Measurement of separate cosmic-ray electron and positron spectra with the fermi large area telescope. *Phys. Rev. Lett.*, 108:011103, 2012, astro-ph/11090521.

[41] M. Aguilar et al. First result from the Alpha Magnetic Spectrometer on the International Space Station: Precision measurement of the positron fraction in primary cosmic rays of 0.5-350 gev. *Phys. Rev. Lett.*, 110:141102, 2013.

[42] Dan Hooper and Tim Linden. Origin of the gamma rays from the Galactic Center. *Phys. Rev. D*, 84:123005, 2011.

[43] Tim Linden, Dan Hooper, and Farhad Yusef-Zadeh. Dark Matter and Synchrotron Emission from Galactic Center Radio Filaments. *The Astrophysical Journal*, 741:95, 2011.

[44] Kevork N. Abazajian and Manoj Kaplinghat. Detection of a gamma-ray source in the galactic center consistent with extended emission from dark matter annihilation and concentrated astrophysical emission. *Phys. Rev. D*, 86:083511, 2012.

[45] Two emission mechanisms in the Fermi Bubbles: A possible signal of annihilating dark matter. *Physics of the Dark Universe*, 2(3):118 – 138, 2013.

[46] Esra Bulbul, Maxim Markevitch, Adam Foster, Randall K. Smith, Michael Loewenstein, and Scott W. Randall. Detection of An Unidentified Emission Line in the Stacked X-ray spectrum of Galaxy Clusters. *Astrophys. J.*, 789:13, 2014, 1402.2301.

[47] Peng-Fei Yin, Zhao-Huan Yu, Qiang Yuan, and Xiao-Jun Bi. Pulsar interpretation for the AMS-02 result. *Phys. Rev. D*, 88:023001, 2013.

[48] Tim Linden and Stefano Profumo. Probing the Pulsar Origin of the Anomalous Positron Fraction with AMS-02 and Atmospheric Cherenkov Telescopes. *The Astrophysical Journal*, 772:18, 2013.

[49] Ilias Cholis, Lisa Goodenough, Dan Hooper, Melanie Simet, and Neal Weiner. High Energy Positrons From Annihilating Dark Matter. *Phys. Rev.*, D80:123511, 2009, 0809.1683.

[50] Ilias Cholis and Dan Hooper. Dark Matter and Pulsar Origins of the Rising Cosmic Ray Positron Fraction in Light of New Data From AMS. *Phys. Rev.*, D88:023013, 2013, 1304.1840.

[51] P. A. R. Ade et al. Planck 2015 results. XIII. Cosmological parameters. 2015, 1502.01589.

[52] Dan Hooper and Lisa Goodenough. Dark Matter Annihilation in The Galactic Center As Seen by the Fermi Gamma Ray Space Telescope. *Phys. Lett.*, B697:412–428, 2011, 1010.2752.

[53] Kevork N. Abazajian. The Consistency of Fermi-LAT Observations of the Galactic Center with a Millisecond Pulsar Population in the Central Stellar Cluster. *JCAP*, 1103:010, 2011, 1011.4275.

[54] Lisa Goodenough and Dan Hooper. Possible Evidence For Dark Matter Annihilation In The Inner Milky Way From The Fermi Gamma Ray Space Telescope. 2009, 0910.2998.

[55] Douglas P. Finkbeiner and Neal Weiner. An X-Ray Line from eXciting Dark Matter. 2014, 1402.6671.

[56] Rouven Essig, Philip Schuster, Natalia Toro, and Bogdan Wojtsekhowski. An Electron Fixed Target Experiment to Search for a New Vector Boson A' Decaying to e+e-. *JHEP*, 02:009, 2011, 1001.2557.

[57] Marat Freytsis, Grigory Ovanesyan, and Jesse Thaler. Dark Force Detection in Low Energy e-p Collisions. *JHEP*, 01:111, 2010, 0909.2862.

[58] B. Wojtsekhowski, D. Nikolenko, and I. Rachek. Searching for a new force at VEPP-3. 2012, 1207.5089.

[59] T. Beranek, H. Merkel, and M. Vanderhaeghen. Theoretical framework to analyze searches for hidden light gauge bosons in electron scattering fixed target experiments. *Phys. Rev.*, D88:015032, 2013, 1303.2540.

[60] Bertrand Echenard, Rouven Essig, and Yi-Ming Zhong. Projections for Dark Photon Searches at Mu3e. *JHEP*, 01:113, 2015, 1411.1770.

[61] S. Gardner, R. J. Holt, and A. S. Tadepalli. New Prospects in Fixed Target Searches for Dark Forces with the SeaQuest Experiment at Fermilab. 2015, 1509.00050.

[62] Sergey Alekhin et al. A facility to Search for Hidden Particles at the CERN SPS: the SHiP physics case. 2015, 1504.04855.

[63] Philip Ilten, Yotam Soreq, Jesse Thaler, Mike Williams, and Wei Xue. Inclusive Dark Photon Search at LHCb. 2016, 1603.08926.

[64] Philip Ilten, Jesse Thaler, Mike Williams, and Wei Xue. Dark photons from charm mesons at LHCb. *Phys. Rev.*, D92(11):115017, 2015, 1509.06765.

[65] R. D. Peccei and Helen R. Quinn. CP Conservation in the Presence of Pseudoparticles. *Phys. Rev. Lett.*, 38:1440–1443, 1977.

[66] Johannes Blumlein and Jurgen Brunner. New Exclusion Limits for Dark Gauge Forces from Beam-Dump Data. *Phys. Lett.*, B701:155–159, 2011, 1104.2747.

[67] Johannes Blümlein and Jürgen Brunner. New Exclusion Limits on Dark Gauge Forces from Proton Bremsstrahlung in Beam-Dump Data. *Phys. Lett.*, B731:320–326, 2014, 1311.3870.

[68] A. Adare et al. Search for dark photons from neutral meson decays in $p+p$ and $d+$Au collisions at $\sqrt{s_{NN}} = 200$ GeV. *Phys. Rev.*, C91(3):031901, 2015, 1409.0851.

[69] Yung-Su Tsai. Axion bremsstrahlung by an electron beam. *Phys. Rev.*, D34:1326, 1986.

[70] Yung-Su Tsai. Pair Production and Bremsstrahlung of Charged Leptons. *Rev. Mod. Phys.*, 46:815, 1974. [Erratum: Rev. Mod. Phys.49,521(1977)].

[71] Kwang Je Kim and Yung-Su Tsai. Improved Weizsacker-Williams method and its application to lepton and W boson pair production. *Phys. Rev.*, D8:3109, 1973.

[72] Jozef Dudek et al. Physics Opportunities with the 12 GeV Upgrade at Jefferson Lab. *Eur. Phys. J.*, A48:187, 2012, 1208.1244.

[73] Volker D. Burkert. The JLab 12 GeV upgrade and the initial science program - Selected topics. *Proc. Int. Sch. Phys. Fermi*, 180:303–332, 2012, 1203.2373.

[74] T. Maruyama et al. A systematic study of polarized electron emission from strained gaas/gaasp superlattice photocathodes. *Appl. Phys. Lett.*, 85:2640, 2004, physics/0412099.

[75] Reza Kazimi, John Hansknecht, Michael Spata, and Haipeng Wang. Source and Extraction for Simultaneous Four-hall Beam Delivery System at CEBAF. In *Proceedings, 4th International Particle Accelerator Conference (IPAC 2013)*, page WEPFI085, 2013.

[76] D0 Collaboration. Layer 2-5 silicon sensor specifications for D0 SMTII. *Internal Note*, 2003.

[77] E. Fretwurst, G. Lindstrom, I. Pintilie, J. Stahl, and I. Pintilie. Radiation damage in silicon detectors caused by hadronic and electromagnetic irradiation. In *Radiation effects on semiconductor materials, detectors and devices. Proceedings, 4th International Conference, RESMDD'02, Florence, Italy, July 10-12, 2002*, 2002, physics/0211118.

[78] I. Rashevskaya, S. Bettarini, G. Rizzo, L. Bosisio, S. Dittongo, and E. Quai. Radiation damage of silicon structures with electrons of 900-MeV. *Nucl. Instrum. Meth.*, A485:126–132, 2002.

[79] M. Raymond et al. The CMS tracker APV25 0.25-mu-m CMOS readout chip. *Conf. Proc.*, C00091111:130–134, 2000. [,130(2000)].

[80] M. Battaglieri et al. The Heavy Photon Search Test Detector. *Nucl. Instrum. Meth.*, A777:91–101, 2015, 1406.6115.

[81] M. J. French et al. Design and results from the APV25, a deep sub-micron CMOS front-end chip for the CMS tracker. *Nucl. Instrum. Meth.*, A466:359–365, 2001.

[82] J. Gaiser. *Charmonium Spectroscopy From Radiative Decays of the J/ψ and ψ'*. PhD thesis, SLAC, 1982.

[83] Glen Cowan, Kyle Cranmer, Eilam Gross, and Ofer Vitells. Asymptotic formulae for likelihood-based tests of new physics. *Eur. Phys. J.*, C71:1554, 2011, 1007.1727. [Erratum: Eur. Phys. J.C73,2501(2013)].

[84] Eilam Gross and Ofer Vitells. Trial factors or the look elsewhere effect in high energy physics. *Eur. Phys. J.*, C70:525–530, 2010, 1005.1891.

[85] Jerome H. Friedman. Data Analysis Techniques for High-Energy Particle Physics. In *1974 CERN School of Computing, Godoysund, Norway, 11-24 Aug 1974: Proceedings*, page 271, 1974.

[86] Glen Cowan, Kyle Cranmer, Eilam Gross, and Ofer Vitells. Power-Constrained Limits. 2011, 1105.3166.